ALTERNATIVE GEOMETRICAL DESIGNS FOR QUARTZ-BASED CHERENKOV DETECTORS FOR THE PANDA BARREL DIRC DETECTOR

Dissertation

zur Erlangung des Doktorgrades

der Naturwissenschaften

vorgelegt beim Fachbereich Physik

der Johann Wolfgang Goethe-Universität

in Frankfurt am Main

von

Marko Zühlsdorf

aus Lich

Frankfurt (2016)

(D 30)

vom Fachbereich Physik der

Johann Wolfgang Goethe-Universität als Dissertation angenommen.

Dekan: Prof. Dr. René Reifarth

Gutachter: Prof. Dr. Klaus Peters
Prof. Dr. Concettina Sfienti

Datum der Disputation: 22. Juli 2016

Abstract

The PANDA experiment will be one of the flagship experiments at the future Facility for Antiproton and Ion Research (FAIR) in Darmstadt, Germany. It is a versatile detector dedicated to topics in hadron physics such as charmonium spectroscopy and nucleon structure. A DIRC counter will deliver hadronic particle identification in the barrel part of the PANDA target spectrometer and will cleanly separate kaons with momenta up to $3.5\,\mathrm{GeV}/c$ from a large pion background. An alternative DIRC design option, using wide Cherenkov radiator plates instead of narrow bars, would significantly reduce the cost of the system. Compact fused silica photon prisms have many advantages over the traditional stand-off boxes filled with liquid. This work describes the study of these design options, which are important advancements of the DIRC technology in terms of cost and performance. Several new reconstruction methods were developed and will be presented. Prototypes of the DIRC components have been built and tested in particle beam, and the new concepts and approaches were applied. An evaluation of the performance of the designs, feasibility studies with simulations, and a comparison of simulation and prototype tests will be presented.

Contents

1. Introduction and Overview 1

2. The Barrel DIRC for the PANDA Experiment at the FAIR facility 3
- 2.1. Hadron Physics with the PANDA Experiment . . . 3
- 2.2. Facility for Antiproton and Ion Research . . . 5
- 2.3. The PANDA Detector . . . 8
- 2.4. Particle Identification at PANDA . . . 10
- 2.5. Ring Imaging Cherenkov Detectors . . . 12
  - 2.5.1. RICH Detectors . . . 14
  - 2.5.2. DIRC Detectors . . . 14
  - 2.5.3. The BaBar DIRC . . . 16
  - 2.5.4. Other DIRC Counters . . . 17
- 2.6. The PANDA Barrel DIRC . . . 19
  - 2.6.1. Baseline Design . . . 19
  - 2.6.2. Challenges . . . 20
  - 2.6.3. Resolution Contributions and Requirements . . . 23

3. Reconstruction for Radiator Plates 27
- 3.1. Simulation Overview . . . 27
- 3.2. Reconstruction for the BaBar DIRC . . . 30
- 3.3. Reconstruction for the Belle-II TOP . . . 31
- 3.4. Geometrical Reconstruction . . . 33
- 3.5. Time-based Likelihood Function . . . 47
- 3.6. Analytical PDFs . . . 62

4. Test of Prototypes with Particle Beams 74
- 4.1. Prototype Components . . . 74
- 4.2. Supplemental Devices . . . 76
- 4.3. 2012 Test Beam Campaign . . . 77
- 4.4. 2014 Test Beam Campaign . . . 85

5. Conclusion 95
- 5.1. Summary . . . 95
- 5.2. Outlook . . . 96

A. Information on the Prototype Plates 98

B. Derivation of the Uncertainties in Chapter 3.6 100

Ausführliche Zusammenfassung 103

1. Introduction and Overview

The Standard Model is the theoretical description of modern particle physics. It is able to explain the interactions of its constituents, quarks and leptons, very precisely and combines the theories of electroweak and strong interaction. For the PANDA experiment at the future FAIR facility in Darmstadt, Germany, antiproton-proton reactions are studied to shed light on some of the unresolved aspects of Quantum Chromo Dynamics, the theory that describes interactions between quarks and gluons. The performance of the detector strongly depends on the ability to identify kaon signals on a pion background over a wide track momentum and polar angle range.

A novel type of ring imaging Cherenkov detector, a DIRC detector, was selected as main component for hadronic particle identification in the central part of the PANDA spectrometer. The baseline design for this detector uses long rectangular synthetic fused silica bars as Cherenkov radiators and a large oil-filled tank for the expansion region where the Cherenkov rings pattern can unfold. The performance strongly depends on the surface quality of the radiators, which is a main cost driver for the full system. In times where many top class projects in fundamental research have to compete for governmental fundings, research efforts aiming to identify more cost efficient alternatives are a crucial part of the overall research and development phase of such an experiment.

For the scope of this work, alternative designs were explored and evaluated. By using wide plates instead of narrow bars for the Cherenkov radiators, the number of fused silica pieces to be polished can be reduced by a factor of five. A compact fused silica prism as expansion volume has practical advantages over the oil-filled tank of the baseline design and in addition would reduce the required number of photon sensors. Apart from a cost-performance optimization of the detector, the evolution of the DIRC counter technology is advanced.

After a short overview of the physics program of the PANDA experiment, the following chapter introduces the FAIR facility and highlights the path of the proton and antiproton from the production point to the PANDA interaction point. The particle identification systems used in the PANDA detector are described, the DIRC technology is introduced, and finally the description of the PANDA Barrel DIRC baseline design, the design options, and the resolution requirements are presented.

Chapter 3 addresses the reconstruction methods developed for this work. A short overview of the software tools and framework is given and the geometrical reconstruction used for the BaBar DIRC as well as the time-based likelihood approach of the Belle-II TOP group are shown. On this basis, two reconstruction algorithms are developed and evaluated with Monte-Carlo simulations.

Several prototypes that have been built and tested in particle beams are described in Ch. 4 and the application and performance of the developed reconstruction algorithms is shown.

The last chapter summarizes and concludes this work and gives an outlook to the future of DIRC technology.

2. The Barrel DIRC for the PANDA Experiment at the FAIR facility

2.1. Hadron Physics with the PANDA Experiment

Modern particle physics is described by the Standard Model which consistently includes three of the four fundamental interactions. The theory of strong interaction, Quantum Chromodynamics (QCD), describes the interaction of quarks and gluons, the constituents of matter and the field boson of QCD, respectively. As an important feature of QCD, the gluons themselves carry color charge, thus take part in strong interactions. As a consequence, the coupling constant increases with increasing distance of the interaction partners, explaining the experimental fact that free quarks are not observed in nature. Instead, bound states in QCD require neutralization of the color charges of the constituents. So far, this has been observed at states containing three or two constituent quarks. The former are called baryons (with color charges "red", "green", and "blue"), and the latter mesons (with color and anti-color).

QCD is well understood and precisely tested at high energies where the coupling constant becomes small and perturbation theory can be applied. In the low energy regime, however, QCD becomes a strongly-coupled theory where many aspects are not yet understood. To shed light on some of the unexplored aspects of non-perturbative QCD, the versatile PANDA (antiProton ANnihilation in DArmstadt) experiment is planned and currently developed as a major part of the Facility for Antiproton and Ion Research (FAIR) [1].

For the PANDA experiment, antiproton-proton reactions are studied with fixed proton and nuclear targets [1]. There are two principal types of possible reactions. In formation reactions, the $p\overline{p}$ directly transforms into resonances with any ordinary $q\overline{q}$ quantum numbers. Hereby, the precision is limited only by the energy resolution of the beam. States with all types of quantum numbers can be created with production reactions, where additional states are produced as recoil particles. The initial energy is distributed arbitrarily over theses states, which means the beam energy and the detector mass resolution contribute to the overall energy resolution. In contrast, electron-positron annihilations create virtual photons so that the quantum numbers of resonances directly produced in formation are restricted to $J^{PC} = 1^{--}$.

The PANDA physics program covers multiple aspects of QCD:

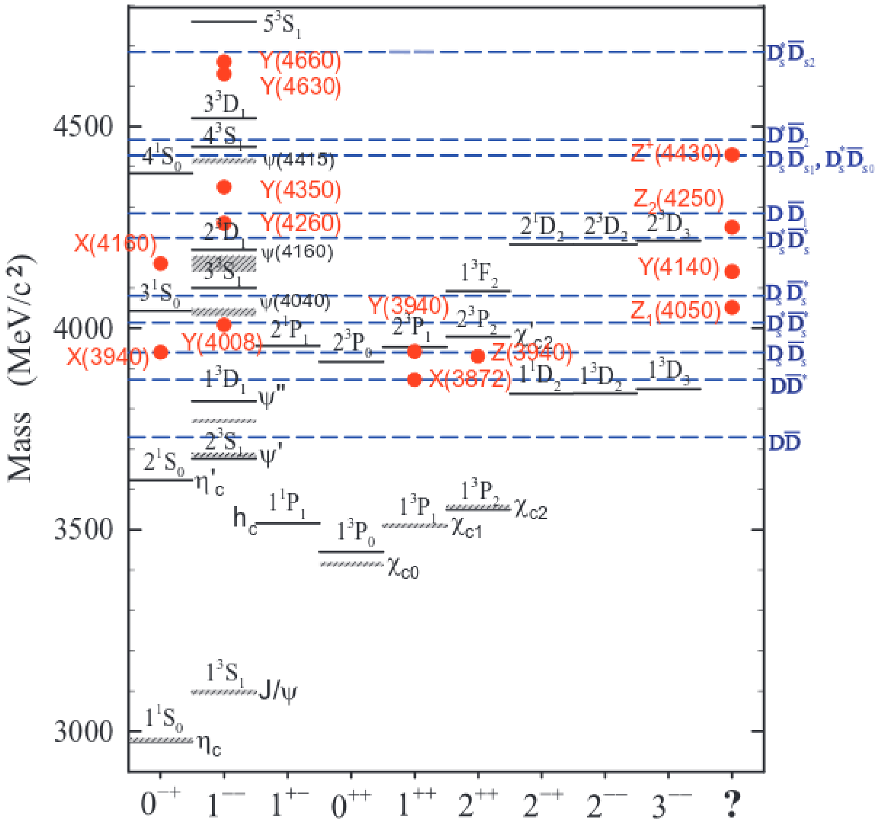

Figure 2.1: The charmonium spectrum. Black lines are predicted (shaded) and measured states (solid), the blue dashed lines represent various thresholds for strong decays. The red dots are newly discovered charmonium-like states [2].

- In experiments such as BaBar [3] and Belle [4], many new and unpredicted states in the charmonium mass regime[1](see Fig. 2.1) were discovered in the past decade. The investigation of these so-called XYZ states, the search for exotic states, such as glueballs, hybrids, and multiquark states in the hidden and open charm region, is within the scope of the scientific program [1] (see Fig. 2.2).

- The study of *D*-mesons and baryon spectroscopy allows verifications of various theories, such as lattice gauge theory or effective field theories.

- Measurements of harmonic properties of hadrons in nuclear matter have shown mass and width modifications for pions and kaons and will be investigated in the charm sector, especially for *D*-mesons.

---

[1] Mesons consisting of a charm and an anti-charm quark are called charmonium.

- PANDA has a hypernuclear program in which pairs of Λ-Baryons with low energies will be implanted in nuclei to understand nuclear structure and the $\Lambda\Lambda$ interaction.
- The structure of nucleons will be studied with hard exclusive proton-antiproton reactions and models like the Hand Bag approach can be tested. Transversal parton distributions can be studied with Drell-Yan production.

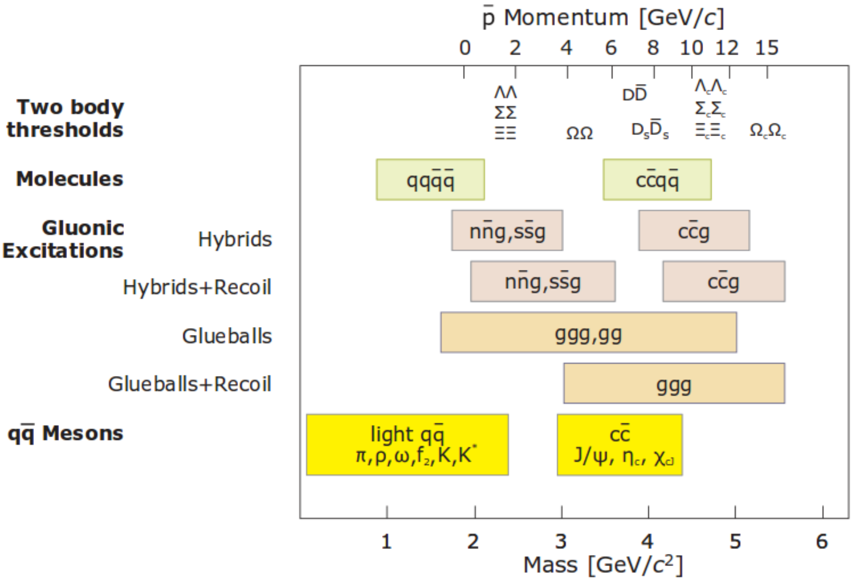

Figure 2.2: Overview of the spectroscopic aspects of the scientific program and the mass range of the PANDA experiment [5].

In order to achieve the experimental goals of the PANDA experiment, it is important to detect and identify final state particles, especially charged kaons and muons. The main challenge is to separate these signal states from the background, which is composed mainly of pions. Thus, it is mandatory to have an excellent particle identification while keeping the whole spectrometer as compact and hermetic as possible (see Ch. 2.3 and 2.5).

2.2. Facility for Antiproton and Ion Research

The FAIR Project

The GSI Helmholtzzentrum für Schwerionenforschung GmbH is a national research center in Darmstadt, Germany, specialized since 1969 on heavy ion research with heavy ion accelerators and storage rings [6]. In the course of the revision and modernization of the scientific program, it was decided to expand the laboratory by extending the accelerator infrastructure and setting up new large scale experiments addressing a broad range of physical topics. The FAIR facility will be the first international laboratory of the Helmholtz Association of German Research Centers. It is expected to be ready for commissioning in 2018 and is subdivided into the four following pillars: NUSTAR [7], APPA [8], CBM [9], and PANDA. These programs are dedicated to nuclear astrophysics, plasma physics, heavy ion research, physics with antiproton beams, and more [10]. The FAIR project aims to set new standards in terms of luminosity and particle rates, to gain insight into the physics of the strong interaction and processes concerning QCD [11]. A characterizing feature of the facility is the possibility to operate beams for parallel usage. This means that up to five research programs with different goals and technical requirements can work at the same time without interference. The beam intensity can be two to three orders of magnitude higher than at the existing facility. Figure 2.3 shows the existing GSI and the FAIR facility, currently under construction.

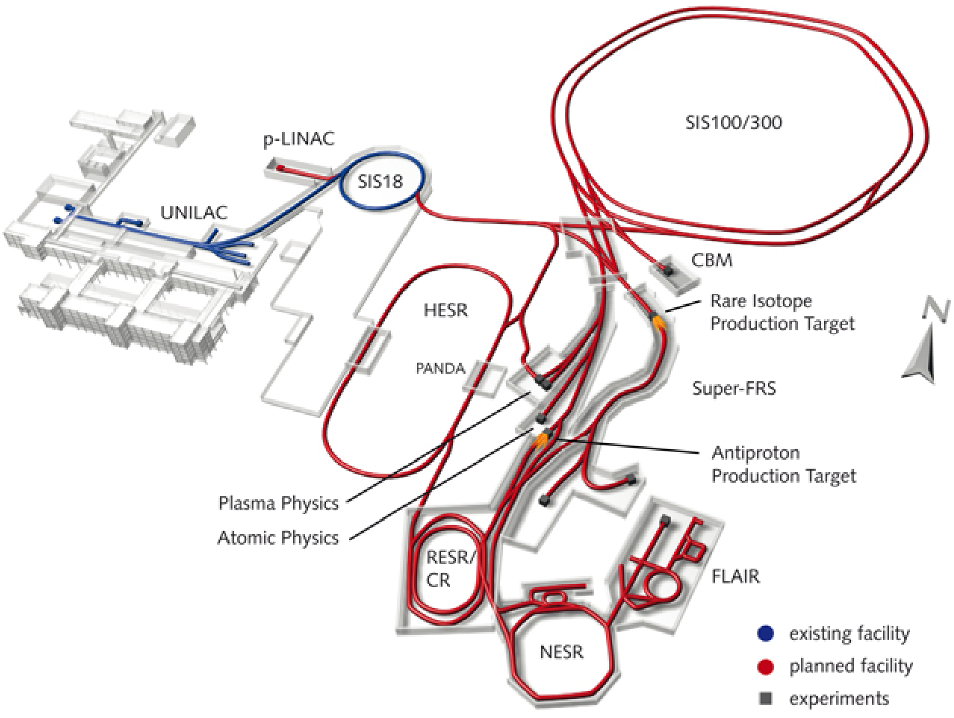

Figure 2.3: Schematic view of the FAIR facility. The blue part and the infrastructure on the left side represent the current GSI status. All red parts mark the new FAIR extensions [12].

The existing GSI accelerators will serve as particle injectors for FAIR. The first stage in the acceleration chain is managed by the UNILAC (UNIversal Linear ACcelerator), which accelerates heavy ions up to 12.4 MeV per nucleon [13]. The

UNILAC is a linear accelerator of 120 m length with two ion sources and a radio frequency quadrupole acceleration structure. The heavy ions are injected into the SIS18 (SchwerIonen Synchrotron = heavy ion synchrotron, the number describes the rigidity).

To provide high intensity proton beams, an additional linear accelerator is planned. The p-Linac (Proton LINear ACcelerator) pre-accelerates protons before they enter the SIS18. The SIS18, with a circumference of 216 m, is the main accelerator at GSI that will provide the FAIR facility with heavy ions and protons, injecting them into the SIS100. The SIS100 will be a synchrotron ring with a circumference of 1100 m that accelerates protons to a beam momentum of 30 GeV/c.

An antiproton production target consisting of nickel or copper is located behind the SIS100. About 10^7 antiprotons/s are created via $p + A \rightarrow p + \bar{p} + p + A$ processes [14]. In the subsequent Collector Ring (CR) and Recycled Experimental Storage Ring (RESR) the antiprotons undergo stochastic cooling and accumulation [15] until they enter the High Energy Storage Ring (HESR), at which the PANDA detector is located. In the first stage of the project only CR will be built and the accumulation takes place in the HESR.

The HESR

After injection into the HESR with an initial momentum of 3.7 GeV/c, antiprotons are, depending on the purpose, accelerated or decelerated to momenta down to 1.5 GeV/c and up to 15 GeV/c.

The HESR can be operated either in high luminosity mode or in high resolution mode [16]:

- The high luminosity mode provides a beam momentum resolution of $\Delta p/p = 10^{-4}$ and a maximum luminosity of $L = 2 \cdot 10^{32}\,\mathrm{cm}^{-2}\mathrm{s}^{-1}$, allowing PANDA to collect data with high statistics at an average interaction rate of 5 – 10 MHz.

- The high resolution mode aims for a momentum resolution of $\Delta p/p = 4 \cdot 10^{-5}$ at a maximum luminosity of $L = 2 \cdot 10^{31}\,\mathrm{cm}^{-2}\mathrm{s}^{-1}$ to be able to perform precise energy scans on narrow resonances with an energy resolution of about 50 keV.

In order to obtain these values, the HESR contains electron cooling (limited to 8.9 GeV/c in high resolution mode) and stochastic cooling to control the emittance of the antiproton beam. Figure 2.4 shows the HESR with beam pipes, the location of cooling devices, and the PANDA experiment.

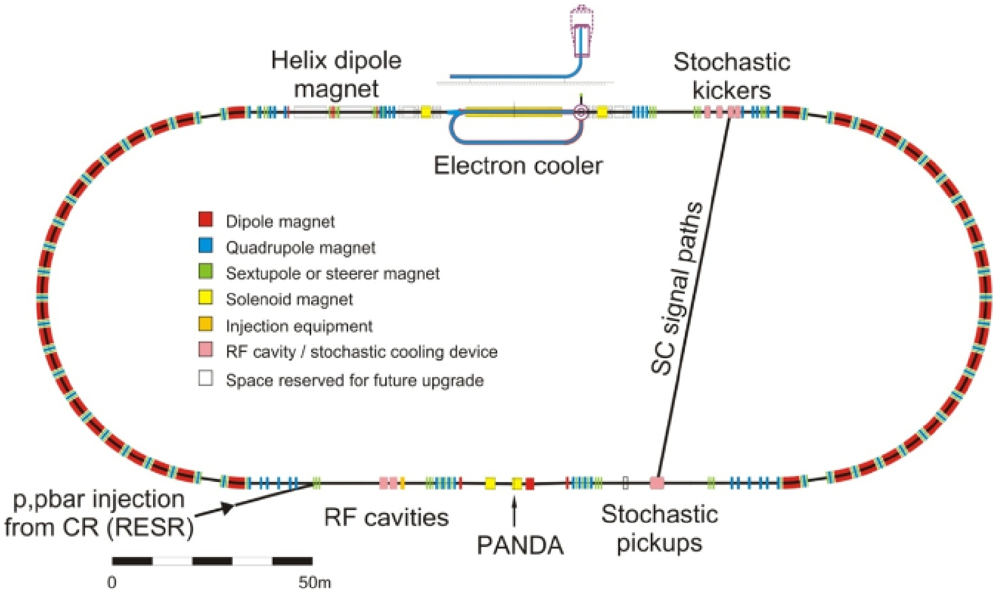

Figure 2.4: Schematic view of the High Energy Storage Ring (HESR). Electron cooling and stochastic kickers are located at the upper straight. On the opposite site, the $\overline{p}$-injection, RF cavities, the stochastic pickup, and the PANDA detector are located [16].

2.3. The PANDA Detector

The broad physical program of the PANDA experiment requires certain features of the spectrometer (Fig. 2.5), such as good coverage of the solid angle, calorimetry of secondary particles, particle identification, precise tracking, and muon detection. The PANDA detector consists of two subunits and each subunit contains detector systems dedicated to these tasks. The Target Spectrometer (TS) surrounds the primary interaction point. It has the shape of a barrel with forward and backward endcaps and covers a polar angle region between 5°(vertical)/10°(horizontal) and 170°. The Forward Spectrometer (FS) covers the region below 5°/10°.

Target Spectrometer

The TS operates within a superconducting solenoid with magnetic fields up to 2 T. The interaction region is defined by the crossing of the beam and the target pipe. The target itself is realized either as a hydrogen cluster-jet or a frozen hydrogen pellet target, and is injected from above, perpendicular to the antiproton beam [5]. Thin wires or foils of various materials can be inserted for $\bar{p} + A$ reactions.

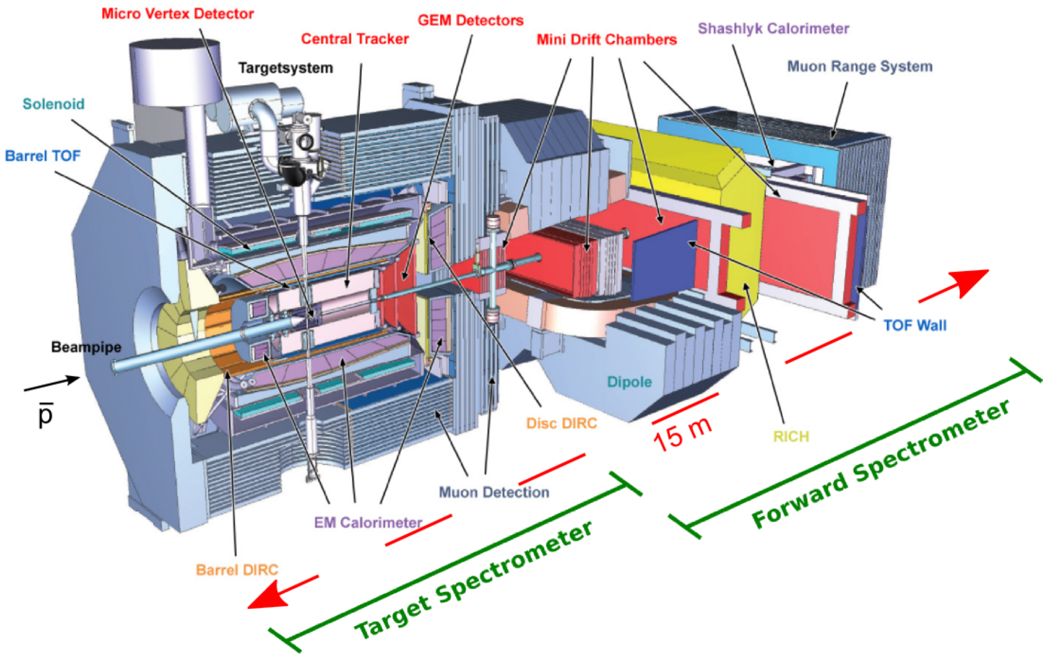

Figure 2.5: The PANDA detector with the target spectrometer and the forward spectrometer. The direction of the antiproton beam is from left to right.

Surrounding the beam pipe at the interaction point, a Micro Vertex Detector (MVD) is optimized essentially for the detection of secondary decay vertices from charmed and strange hadrons [17]. It consists of four barrel-shaped and six disk-shaped layers of silicon pixel and double-sided silicon strip detectors, with an inner radius of 2.5 cm, and outer radius of 13 cm, and a length of 40 cm. The vertex resolution is in the order of 100 μm in z-direction and a few tens of μm in radial direction.

Tracking is performed by a Straw Tube Tracker (STT). In total, 4636 aluminized mylar tubes are arranged around the MVD, each comprising an anode wire and filled with an argon-based gas mixture [18]. A radial track resolution of less than 150 μm is expected. Particles which are emitted towards the forward end cap region ($\theta \leq 22°$) are tracked by the GEM detector consisting of three disks based on gas electron multiplier foils [19].

The main subdetectors for particle identification (PID) are located outside the tracking systems. The Barrel DIRC (Detection of Internally Reflected Cherenkov light) in the barrel section and the Disc DIRC [20] in the forward endcap of the TS are capable of charged particle identification at track momenta up to 3.5 GeV/c and up to 4 GeV/c, respectively. The angular acceptance of the TS is covered up to track polar angles of 140°. A detailed description of the Barrel DIRC is given in Ch. 2.5.

A time-of-flight (SciTil) barrel is positioned outside the Barrel DIRC, at a distance of approximately 50 cm from the beam axis. A PID for slow particles will be provided with 5760 scintillating tiles and a silicon photomultiplier readout with an expected time resolution of 100 ps. The second important role of the SciTil is to deliver precise timing, necessary for event building in the continuous readout mode of the PANDA data acquisition.

Outside of the PID systems, electromagnetic calorimetry (EMC) is performed. A fast scintillator material, being composed of $PbWO_4$ crystals, combines high count rates and a good energy and time resolution [21]. Signals are read out with large area avalanche photo diodes in the barrel part and backward endcap part of the EMC as well as with vacuum photo triodes in the forward endcap part.

The outermost part of the TS is a muon range system (MUO) which is embedded into the flux return yoke of the solenoid. In total 13 sensitive layers alternate with iron absorbers acting as muon filters separating them from pions [22].

For the hypernuclear program, the MVD and the backward endcap will be removed to make room for a secondary target and additional photon detectors alternating with tracking detectors.

Forward Spectrometer

The FS contains similar subsystems to the TS. They are arranged sequentially along the beam line [23].

Tracking is performed by forward tracking straw tube stations before, inside, and behind the field of a dipole magnet. A Ring Imaging Cherenkov detector (RICH), similar to the HERMES RICH [24], is planned for charged particle identification as are time-of-flight walls inside the yoke of the dipole and behind the RICH. Electromagnetic calorimetry is performed by a so-called Shashlyk calorimeter, consisting of alternating blocks of scintillator material and absorbing lead. For the foremost part of the muon spectrum, a tracking system is placed at the downstream end with the additional ability to measure energies of neutrons and antineutrons. Further downstream, the luminosity counter is located to measure the absolute luminosity by detecting antiprotons from elastic scattering.

2.4. Particle Identification at PANDA

As pointed out in Ch. 2.1, particle identification (PID) is a crucial task for the PANDA experiment. The experimental aims as well as the angular, energy and momentum ranges of the particles to be observed, had to be considered before suitable PID systems were chosen. Since PANDA is a fixed target experiment, the reaction products are distributed non-uniformly in the phase space, mainly due to the forward boost. The requirements on PID include the full coverage of polar

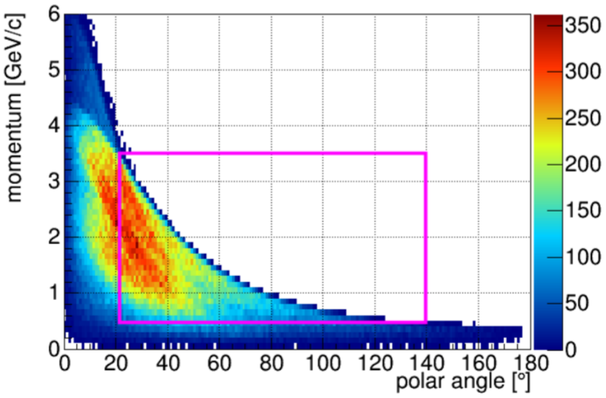

Figure 2.6: Cumulative phase space occupancy of final state kaons originating from open charm decays at the maximum beam momentum of 15 GeV/c [25]. The magenta box surrounds the region covered by the Barrel DIRC.

angles of all observable particles with maximum momenta which depend on the polar angle. Figure 2.6 shows the momentum vs. the polar angle occupancy of final state kaons obtained from Monte-Carlo simulation, taking into account certain benchmark channels of typical PANDA processes. The green box displays the Barrel DIRC acceptance region. The regions outside the box are covered by other subsystems, such as the tracking and vertexing systems for the lower momentum particles ($p < 1\,\mathrm{GeV}/c$), or the Disc DIRC detector and the FS for particles with smaller polar angles ($\theta < 22°$).

The PANDA detector uses several interactions of particles in matter to perform PID.

- The specific energy loss $\mathrm{d}E/\mathrm{d}x$, described by the Bethe-Bloch equation, is sensitive to the velocity of charged particles. It is used to identify particles heavier than electrons. The PID contribution of such detectors is limited to lower momenta (i.e. $< 600\,\mathrm{MeV}/c$ for pion/kaon separation).
- The Cherenkov effect occurs for charged particles with velocities above the phase velocity of light in a given material. It is sensitive to the particle velocity (see also Ch. 2.5). In the TS, the two DIRC detectors are responsible for pion/kaon separation for particle momenta down to 500 MeV/c and 4 GeV/c.
- With fast sensors and a sufficient distance between start and stop counter, the time of flight of particles can be measured to determine the particle velocity. PANDA has no start counter, but the SciTil and the forward TOF counter provide the possibility of relative time measurement for particle momenta up to 1 GeV/c [26].
- The shower shape within the crystals of the EMCs is used to identify electrons and photons. The full kinetic energy of these particles is absorbed in

subsequent Bremsstrahlung and photon conversion processes.

- Muons are identified via the signals they create in the outer sensitive layers of the muon range system, since they are the only particles that are not absorbed in the inner detector. Pions and muons can be separated by the penetration depth in the MUO. While pions are decelerated and eventually stopped in the iron absorber segments, muons pass the outermost layer of the detector due to the very large interaction length.

Most of these measurements require additional information (momentum, sign of curvature in STT, flight path length, etc.) as they do not directly provide the mass of the given particle.

2.5. Ring Imaging Cherenkov Detectors

Cherenkov light is created if a charged particle moves through an optical material with a velocity v that exceeds the speed of light in this material, given by $c_n = c_0/n$, with n being the refractive index and c_0 the speed of light in vacuum (see Fig. 2.7) [27]. The light is emitted conically along the particle trajectory with an opening angle θ_C defined by the speed of the particle ($\beta = v/c_0$) and the wavelength-dependent refractive index ($n(\lambda)$) of the material:

$$\cos(\theta_C) = \frac{1}{n(\lambda)\beta} \tag{2.1}$$

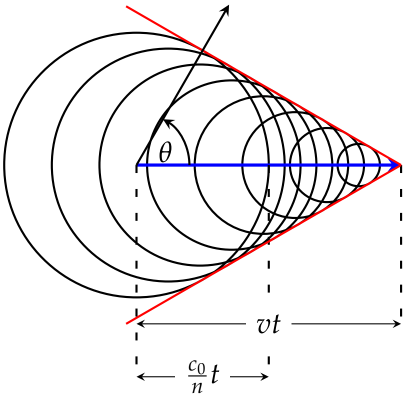

Figure 2.7: In a dielectric medium with a refractive index of n, a charged particle (blue) with $v > c_0/n$ emits Cherenkov radiation along its trajectory. The wavefront (red) of the light forms a cone.

The azimuthal angle ϕ_C of the emitted photons is distributed uniformly on the cone surface.

The intensity (per distance unit $\mathrm{d}x$) of the produced light depends on the wavelength and is, according to the work of Frank and Tamm [28], given by

$$I = \frac{\mathrm{d}^2 N}{\mathrm{d}x \mathrm{d}\lambda} = \frac{2\pi z^2 \alpha}{\lambda^2}\left(1 - \frac{1}{\beta^2 n^2(\lambda)}\right), \tag{2.2}$$

where α is the fine-structure constant and z the charge of the particle in units of e.

The properties of Cherenkov light can be summarized:

- Cherenkov light is only emitted if the charged particle is faster than a material dependent threshold velocity $\beta > 1/n$.
- At the threshold velocity, the Cherenkov angle is zero. It converges to the value $\arccos(1/n)$, at the limit of the particle velocity becoming the speed of light.
- The Cherenkov wavelength spectrum is continuous.
- The Cherenkov effect is faster than e.g. scintillation since the Cherenkov photons are emitted promptly.
- The number of photons created by the Cherenkov effect is much lower than the number of photons created by scintillation.

Cherenkov light and its special properties can be used for many purposes in different fields such as astroparticle physics [29], high energy physics [30], or medical applications [31]. The key role of Cherenkov light in particle identification for modern high energy and hadron physics experiments [32] is explained in the following chapters.

A common feature for all types of Cherenkov detectors is the usage of Cherenkov light emitting radiators and photon sensors. The radiator needs to be thick enough to ensure a sufficient number of photons, which itself depends on the kind and purpose of the counter. The choice of the radiator material also depends on the experiment and the type of Cherenkov counter. The main property is the refractive index, which can be close to 1 for gas ($CO_2 : n = 1.00045$) or higher for aerogel ($n = 1.007 \ldots 1.24$) and solid materials ($SiO_2 : n = 1.47$). In order to maintain the needed Cherenkov information and to propagate the photons efficiently, the radiator has to be as transparent as possible. The photon sensor has to be sensitive for the part of the spectrum that is transported to the sensors and which is most efficient for measuring single photons.

Some of the concepts of Cherenkov counters include focusing optical elements to provide a sharp image on the sensors.

2.5.1. RICH Detectors

Modern Cherenkov detectors are often realized as Ring Imaging Cherenkov detectors (RICH [33]), from which DIRC detectors are derived. The basic idea of a RICH counter is to determine the Cherenkov angle by measuring the radius of Cherenkov rings, created by projecting a Cherenkov cone on a photon sensitive surface. Figure 2.8 shows a possible design, using a spherical mirror and a spherical detection surface. Cherenkov photons are created along the particle trajectory, reflected and focused by a mirror towards the readout plane. A ring-shaped pattern is detected by the sensors and can be resolved spatially. For a spherical mirror with the radius R the readout surface is at $R/2$ and the Cherenkov angle can be calculated by measuring the radius r of the ring via $\theta_C = \frac{2 \cdot r}{R}$.

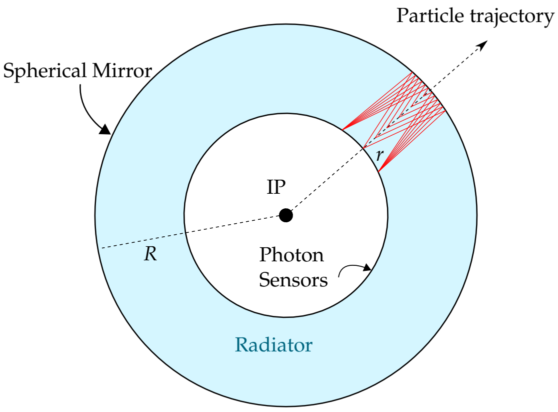

Figure 2.8: Simplified view of a RICH counter. A charged particle comes from the interaction point (IP) and creates Cherenkov photons (red) along the trajectory through the radiator material. The photons are reflected (outer sphere with radius R) and focused on the sensors (inner sphere) in a characteristic ring shape (radius r).

RICH counters have a large acceptance for charged particle directions and momenta as long as the Cherenkov conditions are fulfilled. They are capable of high precision β determination and are nowadays used in many different experiments as a typical PID device.

2.5.2. DIRC Detectors

A special kind of RICH detector where the light is guided to outer regions of the experiment before it expands, is known as DIRC counter. This type of detector is very compact in the radial direction, with respect to the beam axis, so that the outer detector layers can be compact as well. It typically uses synthetic fused silica as both Cherenkov radiator and light guide. The radiator thickness is in the order of a few cm, which is a compromise between the numbers of photons produced, the radiation length for subsequent detector components, and mechanical stability. Figure 2.9 illustrates the DIRC principle, which was initially introduced in 1992 [34] as a hadronic PID system for the BaBar experiment [35].

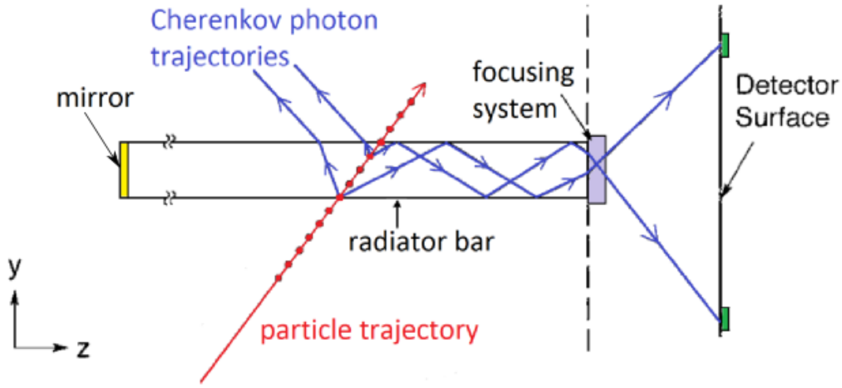

Figure 2.9: The DIRC principle: Cherenkov photons (blue) are created in the radiator bar and propagate through the radiator via total internal reflection, preserving the Cherenkov angle information. At the right end of the figure, they are decoupled out of the bar and registered by the readout sensors [35].

After being produced, a fraction of the Cherenkov photons bounce between the inner surfaces of the radiator via total internal reflection and propagate towards the readout sensors. Photons emitted in downstream direction are reflected at a mirror at the opposite end of the radiator. The surfaces of the radiator need extraordinary smoothness to allow photons to survive several 100 reflections without being absorbed. Excellent parallelism and squareness of the radiator pieces is mandatory to preserve the angle information of the photons. The radiator quality aspects are discussed in more detail in Ch. 2.6.2.

At the readout end of the radiator, which is typically in a region where no or few secondary charged particles are expected, the photons are coupled out with focusing optics into an expansion volume where the Cherenkov ring can unfold. Size and shape of this volume influence the hit patterns of the photons. A readout plane, usually consisting of an array of photomultiplier tubes (PMT), is situated at the back of the expansion volume. The photon sensors have to be capable of single photon detection with a high efficiency, a low dark count rate, and a good time resolution. Additionally, depending on the experiment, they need to function within strong magnetic fields.

DIRC detectors are very compact compared to conventional RICH counters, which allows detector components that are placed behind or in outer parts of the experiment (e.g. calorimeters) to be more compact and, therefore, less expensive.

2.5.3. The BaBar DIRC

Figure 2.10 shows the only existing DIRC detector to date, which was used at the BaBar experiment from 1999 to 2008, an experiment dedicated to the investigation of CP-violation in neutral B-mesons [36].

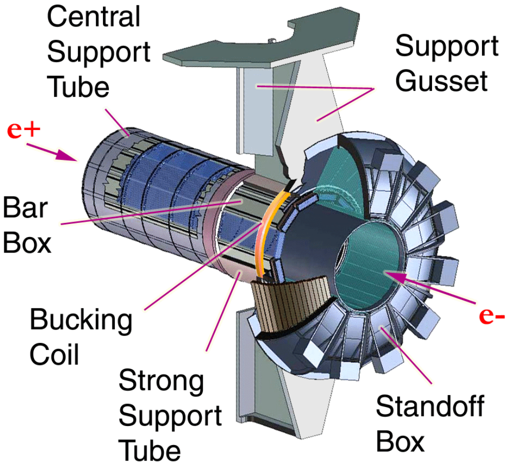

Figure 2.10: Scematic view of the principal components of the BaBar DIRC detector [35].

The DIRC counter is realized as a barrel around the drift chamber and the silicon vertex tracker [35]. Since at PEP-II, the SLAC asymmetric electron-positron collider, final state particles are emitted preferentially into the forward region of the experiment, the sensitive and large readout volume is placed at the backward end. Long rectangular bars are used as Cherenkov radiators to form the barrel. The radiators are made of synthetic fused silica because of its radiation hardness, long radiation length, large refractive index, optical purity, and low chromatic dispersion within the wavelength range of detected photons.

One radiator bar is composed of four identical pieces, each with a length of 1.225 m. The pieces are glued together to form a 4.90 m long radiator with a cross section of 17.25 mm×35.00 mm (Fig. 2.11). Twelve of the long radiators are contained in a box and twelve hermetical sealed boxes form the barrel of the DIRC.

A mirror is placed at the forward end of the long bar and a synthetic fused silica wedge is placed at the backward end between bar and expansion volume. The wedge reduces the emittance space of the exiting photons. As a result, the required detection surface is reduced and steep photons are recovered, which would otherwise be reflected back at the bar-expansion volume interface.

The expansion volume (*Standoff Box*, Fig. 2.10) is, in principle, a steel tank whose outer surface is equipped with 10 752 PMTs. The volume itself is filled with about

6000 *l* of purified water, which serves as cheap interface material between the radiators and the PMTs and has optical properties similar to that of the radiator.

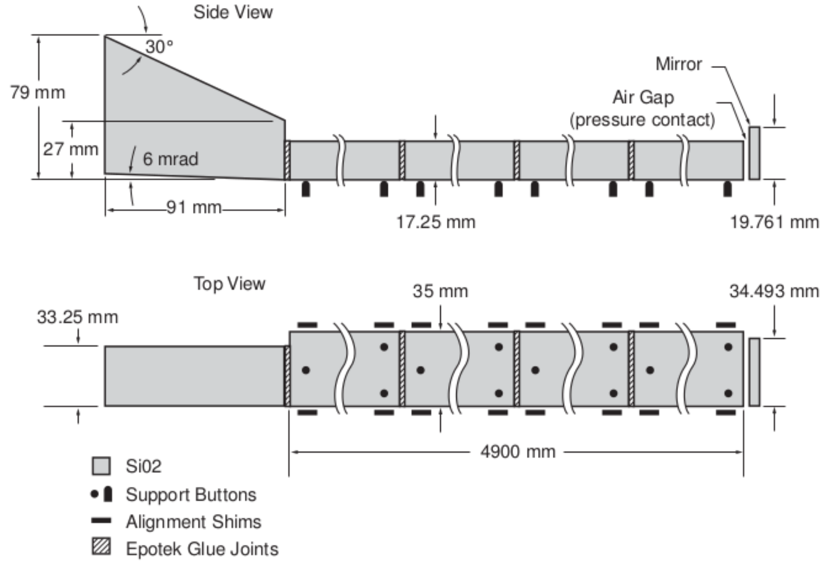

Figure 2.11: Schematic of a single BaBar DIRC radiator bar [35].

2.5.4. Other DIRC Counters

The success of the BaBar DIRC motivated the development of DIRC systems for other large experiments or experimental upgrades, which are currently being developed or constructed. The basic design of DIRC detectors has branched out into two geometries. The first, the traditional BaBar-like form, is a barrel around the main experimental interaction point (IP). The PANDA barrel DIRC follows this shape as well as the imaging Time-Of-Propagation (TOP) counter for the Belle-II [38] experiment and the FDIRC for the SuperB experiment [39]. The latter was planned to be located in Italy. It was supposed to reuse many parts of the BaBar DIRC together with new readout electronics, a new compact expansion volume, and a fast start counter. The experiment was, however, canceled.

Belle-II is an upgrade of the Belle experiment at the asymmetric electron-positron collider SuperKEKB in Japan [40]. The TOP DIRC counter is introduced to improve pion/kaon separation in the barrel region. The main part of the TOP comprises wide fused silica radiators (Fig. 2.12) with a length of 2.5 m and a width of 45 cm [38]. As an important difference to the BaBar DIRC, each of the 16 segments will consist of one wide plate instead of five narrow bars, inspiring the PANDA Barrel DIRC design option presented in this thesis. A spherical mirror will be attached at the forward end, while a small fused silica wedge serves as expansion volume at the backward end. Fast timing (about 100 ps per photon) is essential to the performance of the

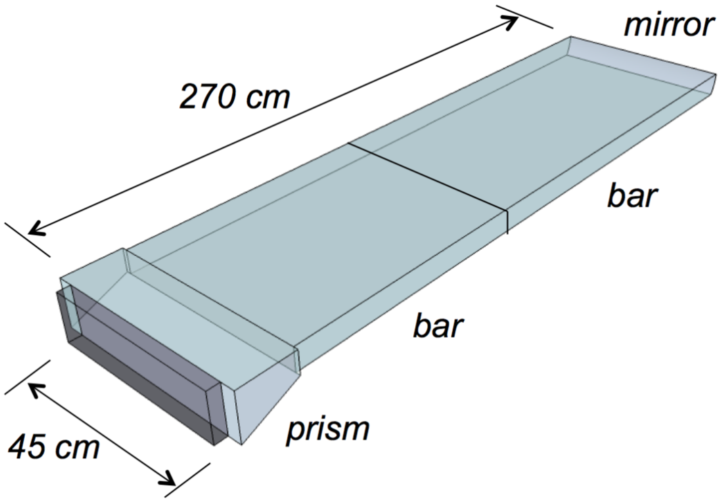

Figure 2.12: A segment of the Belle-II TOP. Wide plates instead of narrow bars are used as radiator shape [37].

TOP and will be delivered by micro-channel plate photomultiplier tubes. Since this work is inspired by the TOP and especially its reconstruction algorithms, a deeper look into the reconstruction will follow in Ch. 3.3.

The other branch is formed by forward DIRCs, a special kind of DIRC being basically described by a 90° rotation of the radiator direction. The PANDA Disk DIRC, located at the forward endcap in the PANDA TS, is an example for this type of detector. It is an octagonal fused silica disk (following the shape of the solenoid yoke) perpendicular to the beam axis. At PANDA, it is responsible for pion/kaon separation in the angular region below 22° and above 5° vertically and 10° horizontally. It poses new challenges to the detector development, as the momenta and the rate of incident particles are higher and the angular spread of the charged particles is smaller than in the barrel region [20].

A forward DIRC with an acrylic glass disk-shaped radiator was planned but canceled for WASA at COSY [41]. TORCH is a high-precision time-of-flight detector realized as quartz disk and scheduled for the upgrade of LHCb [42]. A DIRC counter is planned as PID device in the forward endcap of the upcoming GlueX experiment [43], reusing bar boxes of the disassembled BaBar DIRC. A common feature of the currently planned forward DIRC detectors is a compact expansion volume with the ability to focus incoming Cherenkov light on the detector surface.

2.6. The PANDA Barrel DIRC

2.6.1. Baseline Design

The Barrel DIRC at PANDA is based on the BaBar DIRC. By adapting the design and reconstruction approach, modifying it to match into the PANDA environment and improving key components, a baseline design was developed (Fig. 2.13).The detector has a radius of 47.6 cm and consists of 16 barrel segments, each containing one bar box container equipped with five radiator bars each. A bar is composed of two identical pieces which are connected at the small surfaces to form a long bar with a length of 240 cm. The cross section of a bar is 1.7 cm×3.2 cm.

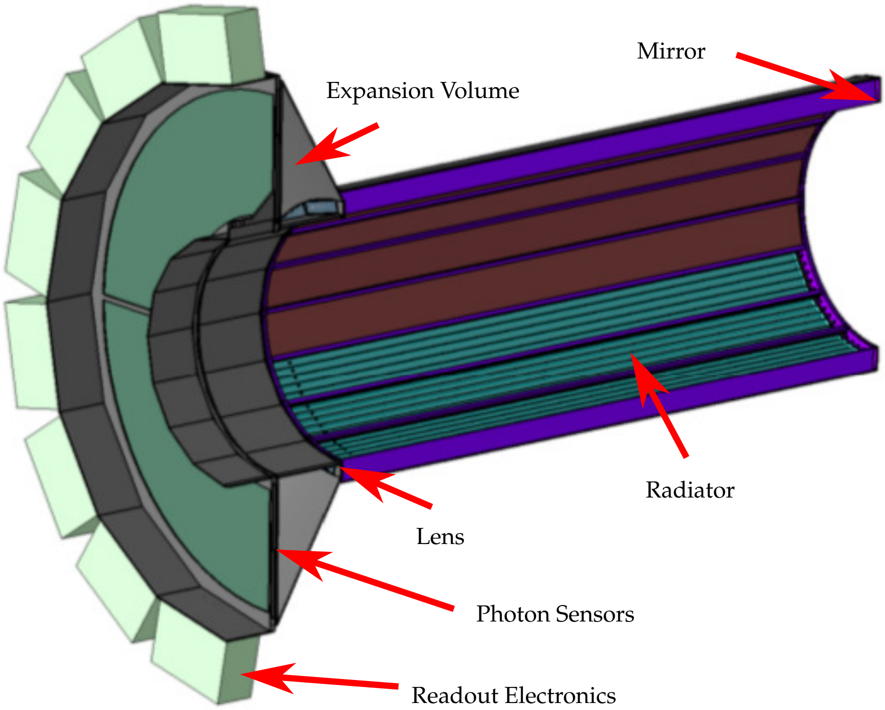

Figure 2.13: Longitudinal section of the baseline design of the PANDA Barrel DIRC. For a better visualization just half of the detector (8 segments) is shown.

Similar to the BaBar DIRC, a flat mirror is attached at the forward end of the bar to reflect Cherenkov photons. At the backward end, focusing lenses are used to improve the imaging of photons onto the detection plane. The expansion volume (EV) is a 30 cm deep monolithic tank filled with mineral oil, matching the refractive index of fused silica. Using micro-channel plate photomultiplier tubes (MCP-PMT), a fast timing in the order of 100 ps is possible. Approximately 15 000 channels will be used.

The baseline design meets the PANDA PID requirement, as shown in [25]. However, there are alternative designs under development, which will be highlighted in the next chapters.

2.6.2. Challenges

During the planning of detectors or detector components, certain challenges arise that are somehow typical for this kind of detector. Regarding RICH type counters, the choice of a suitable radiator material is an important question. Shape, size, and especially the thickness of the radiator are important issues and have to be optimized to match several internal and external criteria [2].

Following a Cherenkov photon along the propagation path, the next systems are the focusing optics and the EV. Different kind of lenses or mirrors of different shapes, materials, and sizes, etc. offer different focusing properties. The type of the EV is an important question, which is also mentioned in this work. A detailed study of the design options for the PANDA Barrel DIRC can be found in [25].

The final module is the readout system, consisting of several elements. The most prominent element here is the readout sensor. The next sections focus on the photon sensors and the radiator in order to emphasize the importance of this work.

Photon Sensors Requirements

The PANDA Barrel DIRC has strict requirements on the readout sensors. They have to be sensitive to single photons with a high detection efficiency and a low dark-count rate to fully exploit the rather small number of photons produced with the Cherenkov effect. It has to operate within the magnetic field of the PANDA solenoid with field strength magnitudes of about 1 T at the position of the sensors. Since the volume containing the sensors is not supposed to be accessible during the operation time of the PANDA detector, the sensors need to have long lifetimes to survive the integrated photon flux. During the PANDA runtime of about 10 years, it is expected that the sensor anodes accumulate a charge of up to $5\,\mathrm{C/cm^2}$ [45]. The requirements are summarized in Table 2.1.

The only type of sensors fulfilling all of these criteria are MCP-PMT. The peak quantum efficiency of a MCP-PMT is typically at the level of 25%. The dark count rate is below 1 kHz per pixel without additional cooling. The sensor is able to

---

[2] An internal criterion for the thickness is the fact that thinner radiators are difficult to produce and to transport. The amount of material in front of the electromagnetic calorimeter is an external criterion.

Requirement	MCP-PMT	MAPMT	SiPM
Single photon sensitivity	yes	yes	yes
Low dark count rate	yes	yes	no
Fast timing (<200 ps)	yes	yes	yes
Good position resolution (<2 mm)	yes	yes	yes
Operation in 1 T magnetic field	yes	no	yes
High rate tolerance (>200 kHz/cm^2)	yes	yes	yes
Long life time(>1 C/cm^2/year, 10^6 gain)	yes	yes	yes
Large active area ratio	yes	yes	yes
Resistance to neutron radiation	yes	yes	no
Availability and cost	yes	yes	yes

Table 2.1: Barrel DIRC requirements on photon sensors, together with the capabilities of different sensor types [44]. MCP-PMT: micro-channel plate photomultiplier Tube. MAPMT: multi anode photomultiplier Tube. SiPM: silicon photomultiplier.

operate within magnetic fields since the micro-channel plates, as electron amplifier, have small channel widths in the order of 10 µm. Recently developed techniques to reduce the photo cathode aging have improved the lifetime of the sensors and make MCP-PMTs feasible for the PANDA DIRCs [45].

The number of sensors, as planned in the baseline design, leave the situation unclear how to arrange the readout and the front end electronics. In addition, the sensors are a major cost driver for the Barrel DIRC . Theses two points motivate efforts to find alternative solutions for the counter with a reduced number of sensors and channels.

The oil filled EV has some disfavorable characteristics. It is a big and heavy structure with a large amount of oil and it requires potentially complicated infrastructure to be kept in place during the PANDA operation time. The inner sides of the EV have to be mirrored to reflect photons towards the readout sensors. That is a difficult task, as the mirrors are in contact with the oil and need to maintain a high refraction quality during operation time.

By using a compact synthetic fused silica EV instead of the oil filled tank, the number of channels can be reduced, because fewer sensors are needed to cover the readout area and the EV would optically match to the radiators. The barrel segments are optically separated from each other, as the system contains one prism per segment with its own readout (Fig. 2.14 shows a prototype prism). The independent and symmetric nature of the segments allows even further reduction of the amount of readout channels with insignificant loss of performance [25]. This is achieved by

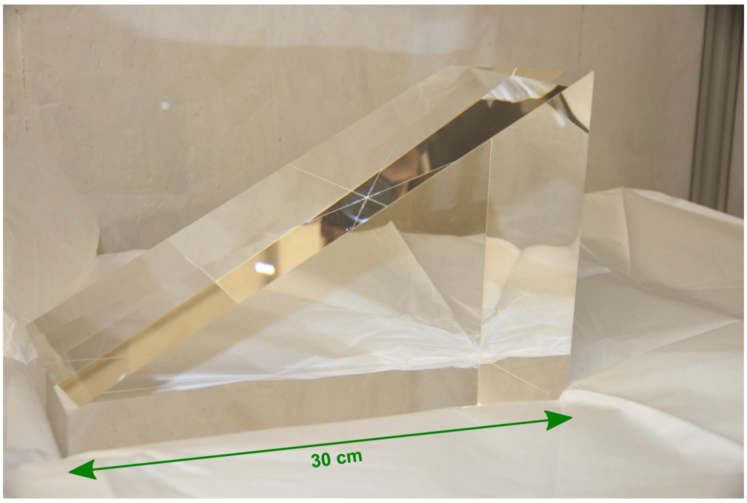

Figure 2.14: Compact fused silica expansion volume manufactured for and used in prototype tests. The opening angle of the prism is 30°.

combining the readouts of two azimuthal neighboring channels, as the requirements on the spatial detector resolution in azimuth is less strict than in radial direction.

Radiator Production

There are special requirements on the optical and mechanical quality of the Cherenkov radiators. To maintain the Cherenkov angle information of the propagating photons, the flatness, the squareness, and the parallelism of the radiator surfaces have to lie within tolerances, which were first specified for the development of the BaBar DIRC [46] and adapted to the conditions at PANDA [47]. The roughness of the radiator surfaces has to be about 10 Å or better, otherwise photons will not pass several hundreds of internal reflections. A maximum variation of the total radiator thickness of 25 μm and surface squareness values with tolerances within 0.5 mrad were specified in order to preserve the angle information of the photons during propagation. The treatment to achieve the required radiator quality level is the main cost driver in the system.

Using one wide plate instead of 5 narrow radiator bars per segment, the total number of radiators will reduce from 80 to 16 pieces (for the long bars). The width of the plates, being 5 times the width of the bars, keeps the Cherenkov active volume unchanged. Since the photons undergo fewer internal (side) reflections, the requirements on the optical quality of the side surfaces can be less severe. Figure 2.15 shows prototype bars and a plate in comparison. Specific information about the produced prototype plates can be found in Appendix A.

The solid prism and the wide plate are very attractive options for the Barrel DIRC, as they have the potential to reduce the cost of the system significantly. The ideas are motivated by the Belle-II TOP counter where a similar design will be realized [38].

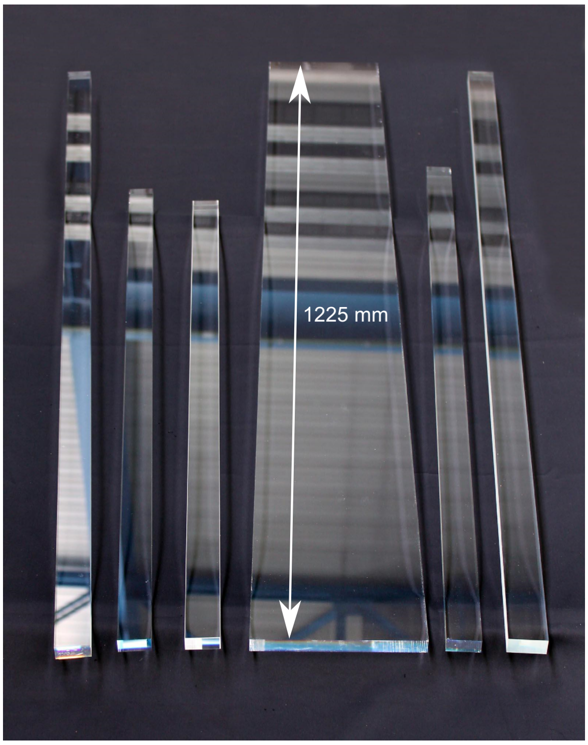

Figure 2.15: Selection of radiator prototypes produced for the PANDA Barrel DIRC R&D program.

2.6.3. Resolution Contributions and Requirements

As a performance requirement, the PANDA Barrel DIRC aims at more than 3 standard deviation separation of kaons from pions for momenta between 0.5 GeV/c and 3.5 GeV/c and angles between 22° and 140°. The separation power SP is defined (in the scope of the PANDA PID) as

$$SP = \frac{\mu_1 - \mu_2}{(\sigma_1 + \sigma_2)/2} \tag{2.3}$$

which reads as the difference of the mean values μ_1 and μ_2, divided by the average of the standard deviations σ_1 and σ_2 of two (Gaussian) distributions (Fig. 2.16). The unit of the SP is in multiples of the average standard deviation (s.d or σ).

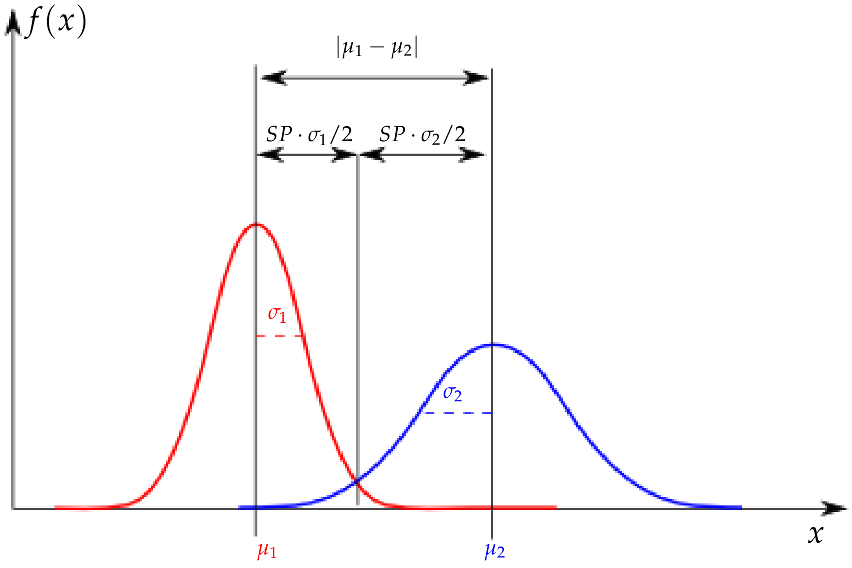

Figure 2.16: The separation power SP is defined as the distance of two Gaussian distributions, normalized by the average standard deviation.

Although the Barrel DIRC is responsible for the PID between *all* hadrons, it is sufficient to focus on the pion-kaon separation, since this hadron combination is the most challenging one. Figure 2.17a shows the momentum-dependent Cherenkov angles for different particle types, using Eq. 2.1 with $n(\lambda) = 1.473$, the mean refractive index for fused silica in the optical region [48]. Figure 2.17b shows the differences of two neighboring curves of Fig. 2.17a. It is clear that kaons are harder to separate from pions at 3.5 GeV/c ($\Delta\theta_C \approx 8.5$ mrad) than from protons ($\Delta\theta_C \approx 25$ mrad) or protons from pions ($\Delta\theta_C \approx 34$ mrad). Electron and muon identification is not in focus of DIRC detectors, since there are other powerful devices dedicated to these particle types. In order to achieve the desired separation power of 3σ between pions and kaons, a Cherenkov angle resolution per charged particle track of $\sigma_{\Theta_C,\text{Track}} = 2.8$ mrad or better is required for particle momenta $p = 3.5$ GeV/c, according to Eq. 2.3.

The single photon Cherenkov angle resolution (SPR) σ_{Θ_C} and the photon yield N_γ are the relevant figures of merit, as they can be determined from test beam data and allow a comparison between different design options and even between different DIRC counters. They are connected with the Cherenkov angle resolution per track via

$$\sigma_{\Theta_C,\text{Track}} = \sqrt{\sigma^2_{\Theta_C}/N_\gamma + \sigma^2_{\text{Corr}}}. \tag{2.4}$$

The term σ_{Corr} originates from effects which influence all created Cherenkov photons

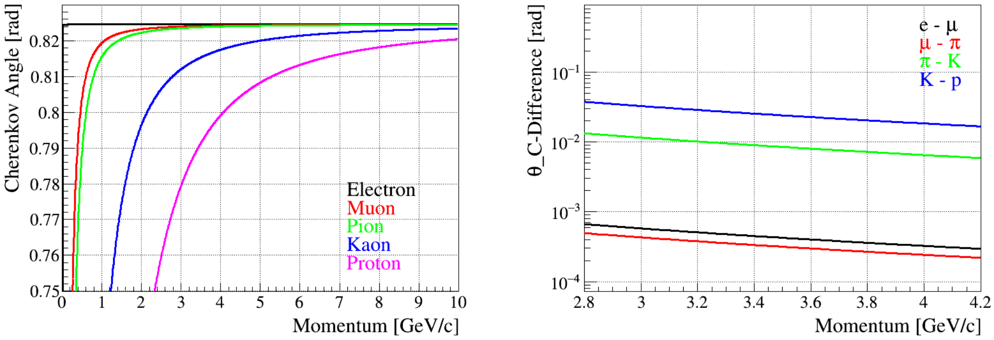

(a) Cherenkov angle as a function of particle momentum for different species.

(b) Differences in Cherenkov angles for adjacent particles on the mass scale.

Figure 2.17: Cherenkov angles in a material with $n = 1.473$, which is the average refractive index of synthetic fused silica.

in the same manner, such as the tracking resolution, errors due to multiple scattering, and misalignment of the system. These are external contributions to the resolution depending on the experimental environment. For the PANDA experiment the tracking resolution is expected to be around 2 mrad for track momenta of 3 GeV/c. The resolution value increases with lower momenta [25, 49].

The SPR comprises several terms and can be written as

$$\sigma_{\Theta_C} = \sqrt{\sigma^2_{\text{chrom}} + \sigma^2_{\text{pix}} + \sigma^2_{\text{bar}} + \sigma^2_{\text{trans}} + \sigma^2_{\text{dir}}}. \tag{2.5}$$

The different contributions are briefly explained:

- σ_{chrom} is the error contribution from chromatic dispersion (Fig. 2.18). Equation 2.1 shows that the Cherenkov angle depends on the phase refractive index of the material, which itself depends on the wavelength of the emitted Cherenkov photons. The expected value of the contribution can be calculated if the spectrum of Cherenkov photons is weighted with the distribution from Eq. 2.2 and inserted into Eq. 2.1. It yields a value of $\sigma_{\text{chrom}} = 5.4\,\text{mrad}$ for the wavelength range of a typical bi-alkali photocathode (300 - 700 nm).

- σ_{pix} corresponds to the finite pixel size, representing the uncertainty of the measurement of exact photon hit position. Assuming a uniform distribution, the pixel size of Planacon tubes (6.5 mm), and 30 cm prism depth gives

$$\sigma_{\text{pix}} = \arctan(6.5\,\text{mm}/300\,\text{mm})/\sqrt{12} \approx 6.3\,\text{mrad}.$$

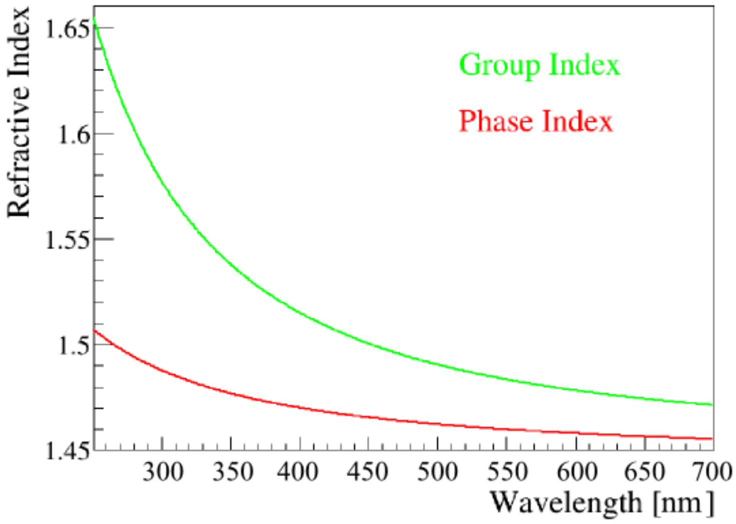

Figure 2.18: Dispersion of phase and group index for synthetic fused silica [48].

- The same calculation is valid for σ_{bar} which represents the uncertainty caused by the finite radiator thickness, i.e. the discrepancy from the pinhole approach. In the case of a radiator plate with a thickness of 17 mm, this computes to $\sigma_{\text{bar}} = 16.4\,\text{mrad}$.
- σ_{trans} is the contribution from the bar imperfections, such as non-squarenesses and non-flatnesses of the radiator surfaces. For the specifications described above, the error is expected be $\sigma_{\text{trans}} \leq 3\,\text{mrad}$.
- σ_{dir} is a systematic error contribution to the systematic uncertainty, caused by the curvature of the particle track inside the radiator. For higher track momenta this contribution decreases.

In order to optimize $\sigma_{\theta_C,\text{track}}$, the SPR has to be minimized, while maximizing N_γ at the same time.

3. Reconstruction for Radiator Plates

3.1. Simulation Overview

An efficient way to perform design studies is the simulation with Monte Carlo methods. The detector system can easily be modeled and tested in simulation, verified before a complex, elaborate prototype is build and tested under real conditions. The framework used by PANDA is PandaRoot [50], based on ROOT classes, using Virtual Monte Carlo as interface to several transport engines.

ROOT is a C++ software package providing tools for scientific applications and data analysis [51, 52]. Virtual Monte Carlo provides an interface to Geant3 [53], Geant4 [54, 55], and Fluka [56], which are the common physic engines in high energy physics.

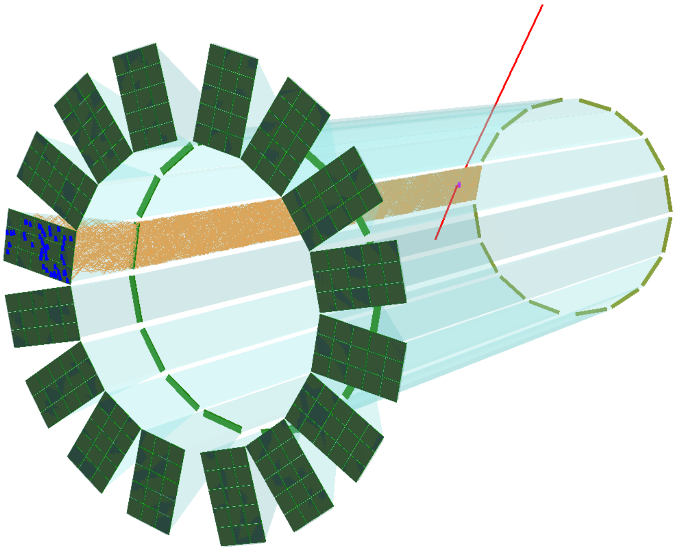

Figure 3.1: Simulated event of a muon generating Cherenkov photons in the PANDA Barrel DIRC. The full barrel consists of 16 segments, each containing a prism EV with 15 sensors attached. Red: Muons; Orange: Photons; Blue: Photon hits on sensors.

PandaRoot supports modular software development for the individual subsystems, using a common code base. The subdetectors are defined by specific geometry shapes, materials, and properties. After the geometry creation, an event generator creates particles (particle gun, physics channels, and background models). The transport engine simulates the passage of particles through the detector volumes, using Monte-Carlo methods. The underlying physic processes, such as ionization, Bremsstrahlung, or Cherenkov radiation, are provided by the physic engines. The detector volumes have physical properties, such as density, atomic weights, atomic numbers, etc. It is possible to include additional effects, such as magnetic fields, multiple scattering or backscattering, to the simulation. The engine used in the scope of this work is Geant4.

The simulation output with the real Cherenkov hit points is stored in data containers, where all relevant information is structured on an event-based level. For the Barrel DIRC simulation, the output is digitized to simulate pixel granularities, time resolutions, and electron cloud charge sharing within the simulated photon sensors. Real experimental setups can therefore be approximated very closely with simulation.

For the work described in the remaining chapters different kinds of simulations were performed. It would have been feasible to use as much details as possible in all the simulations, to get a very close approximation of reality. This was, however, in most of the cases not necessary and even obstructive, as it would have slowed down the simulation. A rather obvious simplification can be seen by comparing the graphic event display[1] in Fig. 3.1 with the displays in Fig. 3.16. The geometry in the former display shows the optical components forming a full barrel with 16 segments, while the other geometry consists of one segment only. Since the optical segments are totally independent from each other using the compact prisms, the full barrel geometry is redundant. All simulated scenarios in this work used (variations of) the geometry shown in Fig. 3.4.

For the geometric reconstruction method (Ch. 3.4) a further simplified simulation was used. The glue and grease layers between the optical components were left out, no magnetic field and no lens was implemented. The simulated charged particle passed symmetrically through the center of the width of the plate. The reconstruction approach relies partly on a precise determination of photon paths. This is much more complicated if the photons are refracted on optical interfaces or not propagating symmetrically through the plate (the magnetic field bends the charged particle within the radiator so the Cherenkov cone would have a curved axis). The glue and grease layers (and lenses) cause photons to become lost before getting measured and registered. The transition to a more realistic simulation was not done, as the reconstruction approach was not able to deliver sufficient PID even with this simplified setup.

---

[1] `EventDisplay.C`, a macro within the PandaRoot package, is used to provide snapshots of simulations. All figures depicting simulations in this thesis are created with this macro.

The simulation for the time-based likelihood approach (Ch. 3.5) was more realistic. The sensitive surface at the backplane of the EV was pixelated and segmented with gaps, in order to simulate the array of photon sensors. For other studies, lenses and glue layers were simulated and compared with simulations without lenses and glue layers. A magnetic field was simulated only to examine the influence on the PID performance. Since there was no meaningful decline of separation power (see Fig. 3.22c), the other simulations were performed without magnetic field in order to save computation time.

An undesirable effect was discovered during the studies of time-based likelihoods. The photon yield in the simulations generally followed the expected distributions. Sometimes, however, an additional tail towards small photon numbers occurred in the distribution. This tail was caused by charged particles which were absorbed somewhere along the way through the radiator. If this occurred, fewer photons were emitted and propagated. The effect was observed only with simulated pions and kaons, not with electrons and muons. Instead of a deeper investigation of a solution, which would have been far beyond the scope of this work, it was circumvented by a flag during the simulation stage. The flag was set in case the primary particle did not exit the radiator, and used to identify valid events during the reconstruction stage. It was discovered only recently, that a faulty setting deep in the standard installation of PandaRoot was the cause of this behavior. Unphysical values for refractive indices were assigned to photons with energies equal or higher than 5 eV. Whenever such a photon was created, Geant4 intercepted the event and stopped the further propagation of the initial charged particle.

For the comparison in the prototype test (Ch. 4), the simulation was modeled to be as close as possible to the prototypes. The geometry of the radiator plate and the prism was adapted, lenses, glue, and grease layers were modeled, and the correct alignment of photon sensors was used. Misalignments of the optical components were measured during the beam time and included in the simulation. While an estimated beam profile was included as well, various potential sources of scattered electrons (e.g. the aluminum cases of the optical components) or light leaks were not simulated.

In all types of simulations, the photon detection efficiency of the sensitive material was a product of the quantum efficiency and the collection efficiency. While the collection efficiency has a constant value of 65%, the quantum efficiency depends on the wavelength and peaks at 380 nm with values around 23.6%.

In some of the systematic studies, a thinner plate, infinitely small pixel size, and monochromatic sensor acceptance was simulated. For the thin plate setup, simply the thickness of the plate was set to the desired value (e.g. 2 mm in Ch. 3.4) during the geometry generation. For other tests, the pixel size was set to zero during the reconstruction stage, by using the real photon hit position instead of the pixel centers to perform reconstruction. The monochromatic acceptance setup was achieved by setting the sensor response to zero for photon wavelength values outside a narrow band. The photon detection efficiency of the readout sensors was generally applied before the photon was propagated. The computation speed was, therefore, much higher in the monochromatic simulation.

When many particles were simulated (tens and hundreds of thousands), in order to gather a solid statistical basis, the computer cluster at GSI was used to simulate in parallel.

3.2. Reconstruction for the BaBar DIRC

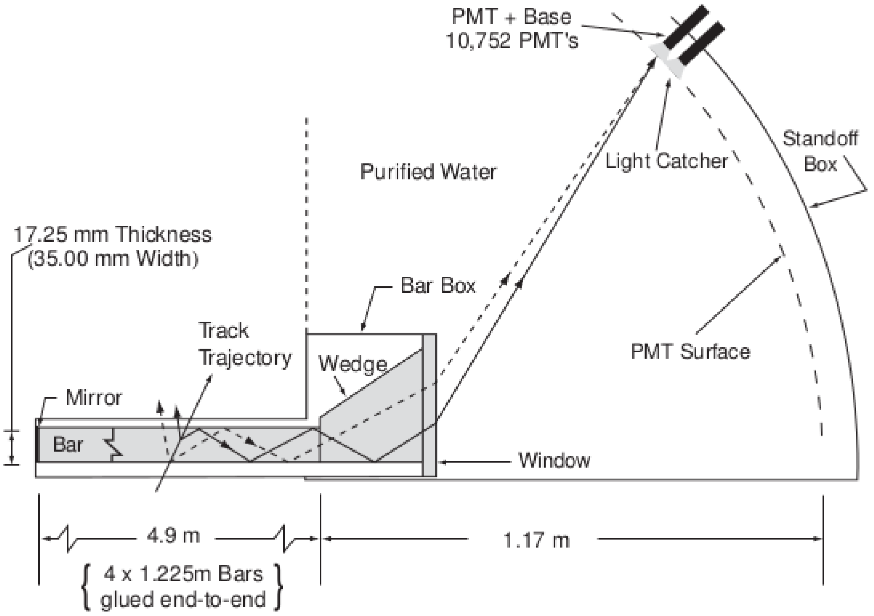

Figure 3.2: Imaging principle used for the BaBar DIRC. The Cherenkov photons are generated within the synthetic fused silica bar and coupled out at the bar end into a tank with purified water. The photons are imaged but not focused when they are detected by PMTs on the right so [35].

The BaBar DIRC reconstructs Cherenkov angles based on the principle of a pinhole camera [35]. Required information are the direction of the charged track and the direction of the Cherenkov photons at the production points. The photons exit the bar into a deep expansion volume (EV), shown as Standoff Box in Fig. 3.2. The tracking systems of the detector deliver the information which bar was hit by the particle and its direction as well as its location. The exact position, where a photon exits the bar, is not known but it can be approximated by assuming that the exit point is the center of the bar. Since the bar′s width and thickness is small, compared to the size of the EV, the contribution of the uncertainty from this assumption is small in comparison to other contributions.

The measured quantities of the DIRC detector are the two spatial coordinates of the position of the photomultiplier tube (PMT) and a hit time information. Together with the position of the hit bar, the spatial coordinates are used to calculate the photon vector at the bar exit. The photon direction inside the bar, before being coupled out, can be calculated using Snell's law. These calculations can be performed offline and stored in a database because the vectors are independent of the reconstructed particle direction or any other variable. After combining the extrapolated vector with the known particle direction, θ_C and ϕ_C of the photon can be obtained.

Due to the photon propagation and reflection inside the bar, the reconstructed photon direction is not unambiguous. Possible ambiguities are: forward/backward, top/bottom and left/right in the bar, and finally a possible reflection at the top of the wedge. A reflection at the bottom of the wedge is treated as resolution contribution and not as ambiguity. This results in 16 ambiguities, one being the true signal and the others being distributed and forming a combinatorial background. Only two of the three measured parameters are used to calculate the Cherenkov angles so the third (redundant) observable, the hit time, helps reducing the number of ambiguities.

The Cherenkov angle is determined based on a maximum likelihood algorithm. The likelihood value for each of the five particle species is derived by evaluating the corresponding probability density functions with the reconstructed Cherenkov angle θ_C.

3.3. Reconstruction for the Belle-II TOP

The Belle-II TOP uses a compact fused silica prism in each segment instead of a common EV for all segments as used in the BaBar experiment. This new concept, together with the usage of wide radiator plates, requires a new reconstruction approach. In Fig. 2.12 one of the 16 symmetric segments can be seen. The segments are optically independent, so it is sufficient to define the reconstruction process for a single unit.

The approach makes use of fast pixelated photon sensors to measure the spatial hit coordinates and the arrival time of photons with a resolution below 100 ps. It uses an extended likelihood method for particle identification based on an analytical construction of the likelihood functions [57]. The likelihood L_h for a given particle hypothesis is defined as

$$\begin{aligned} L_h &= \prod_{i=1}^{N} \left(\frac{S_h(x_i, y_i, t_i) + B(x_i, y_i, t_i)}{N_e} \right) \times P_N(N_e) \\ \Rightarrow \log L_h &= \sum_{i=1}^{N} \log \left(\frac{S_h(x_i, y_i, t_i) + B(x_i, y_i, t_i)}{N_e} \right) + \log P_N(N_e), \end{aligned} \tag{3.1}$$

where S_h is the signal distribution for a particle hypothesis h over all pixels and all arrival times. Since it is normalized to the expected number of signal photon hits per event N_S, it can be viewed as the probability density function (PDF) for a particle hypothesis[2]. Signal photon hits are the detector hits caused by Cherenkov photons of the charged particle, which include electronic crosstalk. Hits caused by detector noise contribute to the background distribution B and the expected number of background photons N_B. B is normalized to N_B. N_e is the expected number of detected photons, being the sum of N_S and N_B, and N is the number of actual measured hits.

The product of the expression in parenthesis in Eq. 3.1 is a likelihood function which is suitable to discriminate between particle hypothesis. The logarithm can be taken because it is strictly monotone and the actual value of the function has no meaning. Only the comparison between different likelihood values matters. In particular, it simplifies the computation of the equation. The last term in Eq. 3.1 accounts for the fact that different particle hypothesis have different expected numbers of hits for tracks with the same properties.

The function S_h depends on the track parameters and therefore has to be parametrized. A simulation of S_h is possible for development purposes but it is numerically not feasible to perform simulations for all track configurations during the experiment runtime or beforehand. The parametrization is done for each pixel j, resulting in one-dimensional time distributions:

$$S_h^j(t) = \sum_{k=1}^{m_j} n_k G(t - t_k; \sigma_k) \tag{3.2}$$

Each of the j functions is composed of normalized Gaussian distributions G with m_j peaks, each peak having n_k photons, a position at t_k, and a width of σ_k.

The analytical expressions and derivations for the quantities t_k, n_k, and σ_k are complicated and depend on the geometrical design of the TOP counter. The peak position t_{kj} is influenced by the photon propagation time until detection, the polar and the azimuth angle of the particle, the Cherenkov angle θ_C, and the position where the particle passes through the radiator. The number of photons per peak, n_{kj}, depends on the length of the particle trajectory in the radiator, the Cherenkov

---

[2] Technically, this is not true, as PDFs are normalized to unity. The expression in the parentheses in Eq. 3.1 is normalized to unity, so that would be the PDF.

angle, and the fraction of the Cherenkov azimuth angle covered by the channel j. The width σ_{kj} of the peaks depends on the terms coming from Eq. 2.4 and 2.5 and the time resolution of the photon sensors and the readout electronics. Detailed derivations of these dependencies can be found in Ref. [58] and will not be discussed here.

3.4. Geometrical Reconstruction

The variables and the reference frame used in the following chapters are shown in Fig. 3.3. The X-axis points along the width of the plate, the Y-axis along the thickness, and the Z-axis along the length. Since the Z-axis in this reference frame is identical to the Z-axis of the general PANDA reference frame, the axis points to the forward mirror of the DIRC (which is the beam direction) and the EV coordinates have negative Z-values.

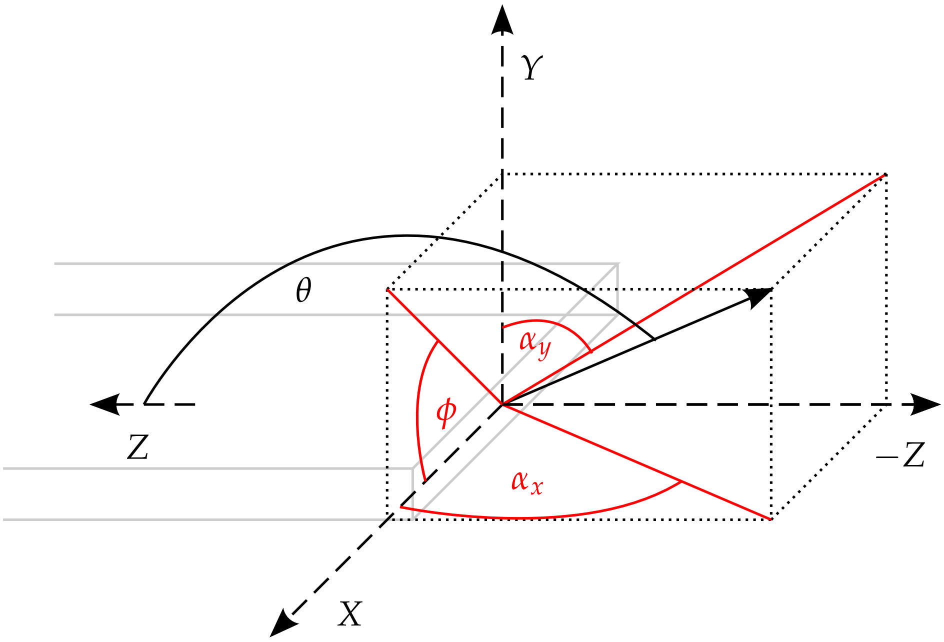

Figure 3.3: Schematic of the local coordinates system for the plate. The black non-dashed arrow represents the photon direction at the plate exit. The projections of this vector into the coordinate planes are indicated in red, together with the angles which need to be reconstructed in order to determine θ_C.

The geometrical reconstruction algorithm for the PANDA Barrel DIRC is based on the reconstruction method developed and used successfully for the BaBar DIRC. There, the photon directions were approximated by the connection line between the center of the bar end and the center of the hit pixel on the detection plane. This so-called pinhole focusing ignores effects due to the width and thickness of the bar, which was valid for the BaBar DIRC due to the small ratio of the bar cross section to the depth of the EV. The photon vectors were stored in databases and could be obtained by calculation or simulation. At BaBar, the contribution of the size of the bar cross section to the total θ_C error were in the same order of magnitude as the contributions from the size of the pixels and the θ_C smearing from dispersion. Since the baseline design of the PANDA Barrel DIRC has similar geometrical properties, this reconstruction approach with slight modifications can be applied to the PANDA Barrel DIRC as well. Performance results of various designs based on narrow bars are described in [25]. In order to evaluate the designs, the general goal of this reconstruction approach is to determine two figures of merit: The single photon Cherenkov angle resolution σ_{Θ_C} and the photon yield N_γ are used for a comparison between designs and between experimental data and simulation (see Eq. 2.4).

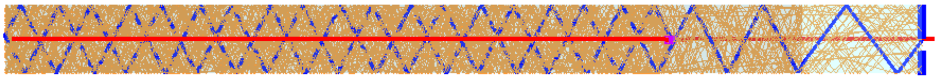

(a) X-Z projection.

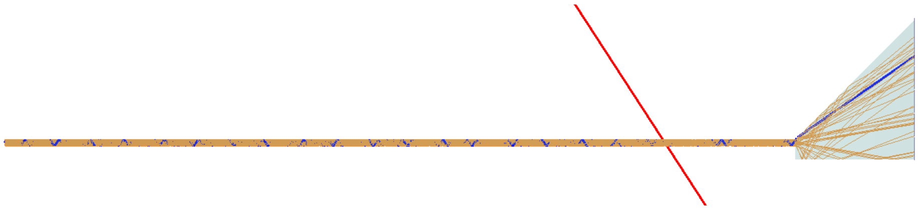

(b) Y-Z projection.

Figure 3.4: Geant simulation of Cherenkov photons (orange) created by one charged particle (red). One photon path is highlighted (blue). Some of the photons are reflected at the glue interface between plate and prism. The charged particle does not originate from the PANDA interaction point.

The wide plate geometry, however, requires a completely different reconstruction approach. The plate has the same thickness as the radiator bar, while the width is much larger, typically identical to the width of the EV. Figure 3.4 shows two projections of a DIRC module, where a charged particle crosses the plate. The position of the photon exiting the radiator in the X-Z projection (Fig. 3.4a) is completely uncertain and the projected angle between photon direction and (negative) Z-axis can take any value between -90°and +90°. The application of a pinhole focusing is only valid for the photon direction in the Y-Z projection (Fig. 3.4b).

The reconstruction task is therefore split into two parts. The angle α_y between the photon direction in Y-Z projection and the Y-axis is stored in a look-up table.

Depending on the Y-coordinate of the sensor hit, the value of the angle can be obtained very quickly. The resolution is determined by the width of the plate, the depth of the expansion volume, and the size of a sensor pixel. The corresponding angle in X-Z projection, α_x, is not obtained from a database but calculated directly with the information of the position of the charged particle, the sensor coordinates, the arrival time of the photon, and the reconstructed α_y.

Both angles are used to determine the photon direction in three dimensions, which is afterwards connected with the particle track direction to determine the Cherenkov angle. Due to the chromatic dispersion of the refractive index of fused silica and different sequences of photon reflections, ambiguous solutions for the reconstructed angles appear in both projections. The reconstruction is explained in detail in the following sub-sections.

Y-Z Projection

In the Y-Z projection it is assumed that the photon exits the radiator at the middle of the end surface (see Fig. 3.5), so, apart from a determination of the correct angular quadrant, the photon propagation needs to be described only inside the EV and not in the radiator to obtain α_y. The EV, realized as a fused silica prism, has reflecting side surfaces and therefore allows different sequences of reflections before the photon hits the photo detection (PD) plane. Figure 3.5 shows the situation for a prism with an opening angle γ of 45°. The geometry leads to four ambiguous photon directions from the plate end to each pixel (prism ambiguity; two ambiguities vanish for hits in the lower part of the PD plane.). The photon can go directly to the plate, it can bounce at the bottom of the EV or at the top, and it can bounce first at the bottom and then the top. In the case of a $\gamma = 45°$ these are all existing possibilities.

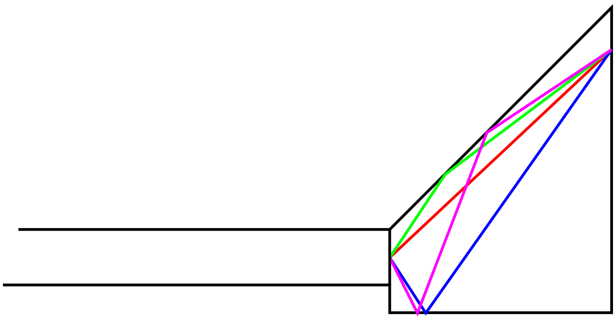

Figure 3.5: Schematic view of the expansion volume ambiguities in Y-Z projection. For $\gamma = 45°$, up to four different photon paths end up in the same pixel. Red: direct photon; blue: photon reflected at the bottom; green: reflected at the top; purple: reflected at bottom and top.

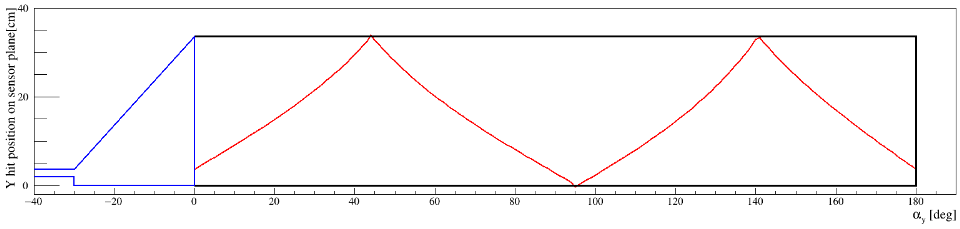

Figure 3.6: Analytic function to calculate the α_y-ambiguities. The geometry is displayed in blue on the left side (Y-Z projection): The plate has a thickness of 1.7 cm, the prism an opening angle of 45° and a step of 1 cm between bottom of the plate and bottom of the prism. The Y coordinate of a sensor pixel hit is on the Y-axis of the plot. At this value, a horizontal line can be drawn. The angle values of the α_y-ambiguities are the intersections of this line with the red function.

Due to the fact that α_y can be calculated analytically or by simulation beforehand and stored in a look-up table, it can be obtained very quickly. Figure 3.6 shows the analytical relation to obtain the values of α_y in a prism with 45° opening angle. A horizontal line can be drawn in the plot at the Y-coordinate of the hit. Intersections of this line with the red curve yield the ambiguities of α_y on the X-axis. The four slopes each belong to a different projection sequence in the prism.

It is not predictable which direction the photon initially took before it reached the plate exit, so more ambiguities arise by possible reflections on the top or bottom surface or the forward mirror (Fig. 3.7). Since we are only interested in the projection to the Y-Z plane, the reflections on the left/right surface can be ignored at this stage of the reconstruction. This results in (up to) $4 \times 2 \times 2 = 16$ ambiguous solutions for α_y.

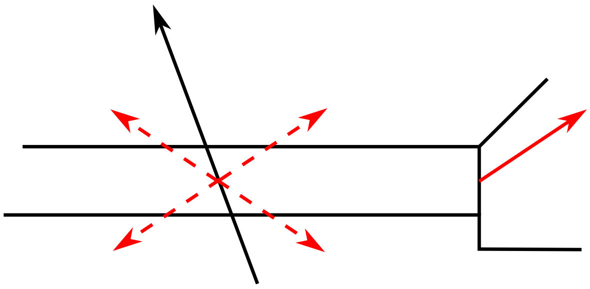

Figure 3.7: A photon at the plate exit (red solid arrow) could have started in four different directions (red dashed arrows). The black arrow marks the direction of the charged particle.

X-Z Projection

Up to now, only the Y-coordinate of the hit pixel has been used in the reconstruction. The information of the hit X-coordinate and the hit time were not considered yet and will be used for the calculation of α_x. Since the ratio of the radiator width and the length of the total photon path (see Fig. 3.4a) is relatively large in comparison to the ratio of the thickness and the length of the photon path, a full geometric path reconstruction (in X-Z projection) is much easier than in the case of radiator bars.

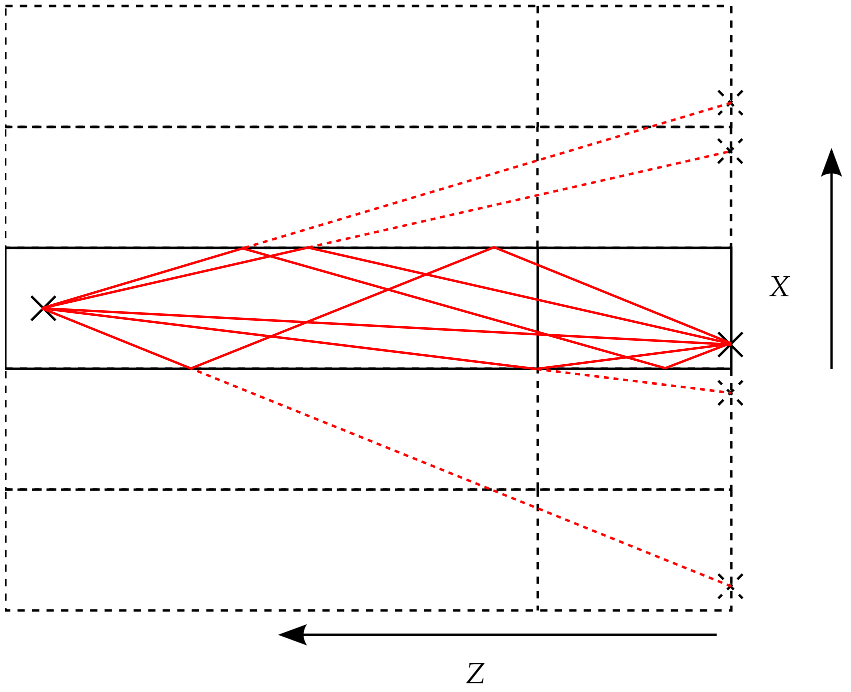

Figure 3.8: Five possible photon paths are shown with red solid lines. The dashed lines represent the unfolded photon paths.

The general strategy is to find the corresponding α_x ambiguities for every α_y ambiguity. A value for α_x is derived from the photon propagation path l, the corresponding α_y, the hit X-coordinate, and the hit time. The length of the photon propagation path can be obtained by unfolding the photon path on the reflecting sides of the radiator (see Fig. 3.8). The coordinates on the unfolded readout plane will be called x_u, y_u, and z_u (Fig. 3.9). The latter is the Z projection of the distance of the particle-plate intersection point to the readout plane, either directly or pointing to the mirror (and taking much higher values due to the larger propagation distance).

The photon path length l can be expressed as

$$l^2 = x_u^2 + y_u^2 + z_u^2. \tag{3.3}$$

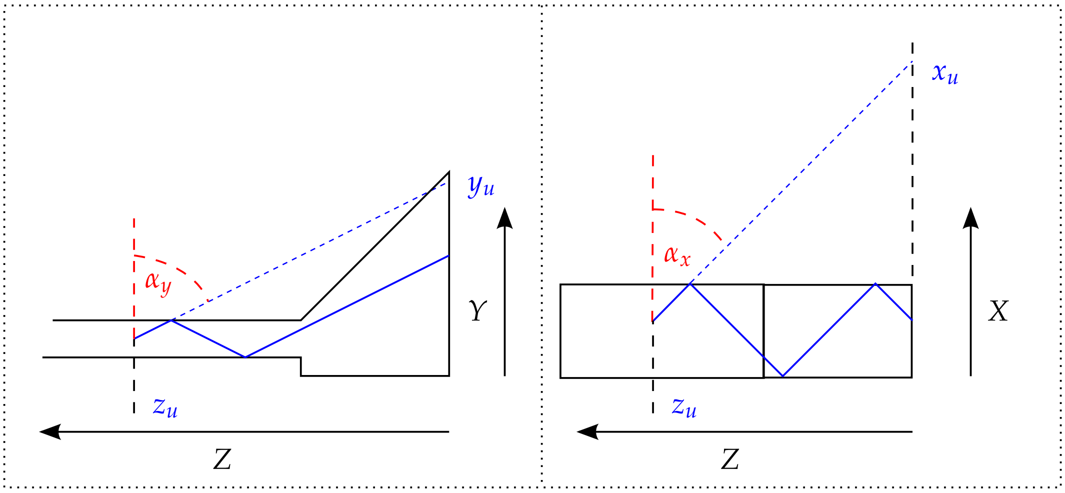

Figure 3.9: Derivation of α_x: The photon path becomes straight if it is unfolded at the reflecting surfaces. x_u, y_u, and z_u are the photon hit locations on the extended sensor plane, if the photon would have propagated on a straight line without reflections after production.

The length is related to the time of photon propagation T and the speed of the photon $c_n = c_0/n_{\mathrm{Gr}}$, which itself depends on the group index n_{Gr}.

$$l = c_n \cdot T = \frac{c_0 \cdot T}{n_{\mathrm{Gr}}} \tag{3.4}$$

c_0 is the speed of light in vacuum. According to Fig. 3.3, x_u can be expressed as

$$x_u = \frac{-z_u}{\tan \alpha_x} \tag{3.5}$$

and y_u as

$$y_u = \frac{-z_u}{\tan \alpha_y}. \tag{3.6}$$

These formulas can be combined and solved for α_x:

$$\begin{aligned} l^2 &= \frac{z_u^2}{\tan {\alpha_x}^2} + \frac{z_u^2}{\tan {\alpha_y}^2} + z_u^2 \\ \implies \frac{l^2}{z_u^2} \tan {\alpha_x}^2 &= 1 + \frac{\tan {\alpha_x}^2}{\tan {\alpha_y}^2} + \tan {\alpha_x}^2 \\ \implies \tan \alpha_x &= \frac{1}{\sqrt{\left(\frac{c_0 \cdot T}{z_u \cdot n_{\mathrm{Gr}}}\right)^2 - \left(\frac{1}{\tan \alpha_y}\right)^2 - 1}} \end{aligned} \tag{3.7}$$

A complication for this approach arises when taking chromatic dispersion into account. The wavelength dependence of $n_{\mathrm{Gr}}(\lambda)$ translates into a wavelength dependent photon propagation speed. Additional uncertainties or ambiguities are hereby added to the approach. Figure 3.10 illustrates the situation.

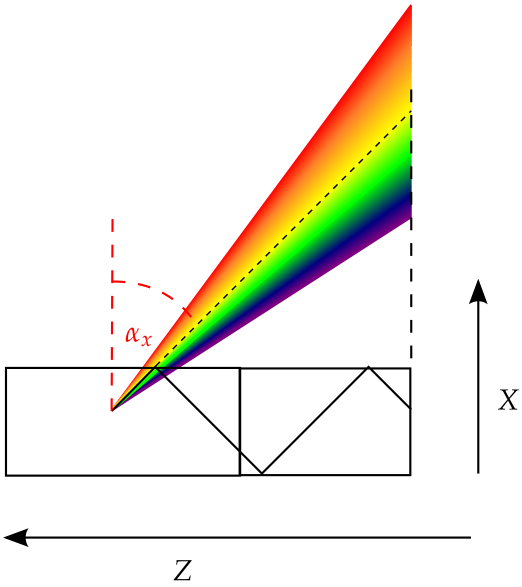

Figure 3.10: Influence of the dispersion on the uncertainty of α_x. Photons with different wavelengths, here indicated by the color, have different values for α_x. The dimensions of the plate and the EV are not to scale.

This issue is resolved by considering the two extreme cases for (detected) Cherenkov photons (e.g. “blue” and “red”) which are propagated to their expected positions on the unfolded pixel plane, defined by the measured arrival time. Since information about the photon wavelength is not available, every possible solution between the extreme cases is in principle valid. Combined with the constraints on the X-position of the hit on the plane, the number of ambiguities is reduced to discrete solutions. The number increases with larger values of z_u as more solutions for x_u values are found between the extreme cases (Fig. 3.8 and 3.10).

Polar and Azimuth Angle

Figures 3.3 and 3.11 illustrate how the polar and the azimuth angle of the photon in local coordinates can be calculated, using α_y and α_x. By definition, ϕ and θ are given as

$$\tan^2\theta = \frac{x^2+y^2}{z^2} \tag{3.8}$$

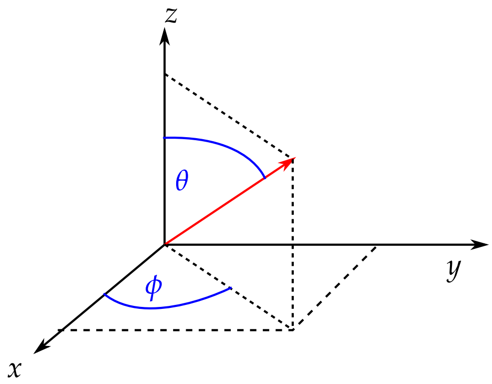

Figure 3.11: Derivation of the spherical angles θ and ϕ from Cartesian coordinates x, y, z.

and

$$\tan\phi = \frac{y}{x}. \tag{3.9}$$

Figure 3.3 shows that α_x and α_y can be expressed as

$$\tan\alpha_x = \frac{-z}{x} \tag{3.10}$$

and

$$\tan\alpha_y = \frac{-z}{y}. \tag{3.11}$$

Combining these equations yields

$$\begin{aligned} \tan^2\theta &= \frac{1}{\tan^2\alpha_x} + \frac{1}{\tan^2\alpha_y} \\ \Rightarrow \theta &= \arctan\left(\sqrt{\frac{1}{\tan^2\alpha_x} + \frac{1}{\tan^2\alpha_y}}\right) \end{aligned} \tag{3.12}$$

for θ and

$$\tan\phi = \frac{\tan\alpha_x}{\tan\alpha_y} \Rightarrow \phi = \arctan\left(\frac{\tan\alpha_x}{\tan\alpha_y}\right) \tag{3.13}$$

for ϕ. The mathematical dependencies of ϕ and θ lead to ambiguous quadrants. This can be resolved by looking to the quadrants of α_x and α_y. If, for example, α_y is between -90° and 90°, ϕ must have a value between 0° and 180°.

Performance

There are several contributions to the uncertainty of the reconstructed θ_C. The pixel size, the radiator thickness, the dispersion in the phase refractive index n_p and in the group index n_{Gr}, the uncertainty on the position where the track hits the radiator, and the resolution of the polar track angle, all influence the PID performance (see Ch. 2.6.3 and Eq. 2.5). The goal of the performance test of the reconstruction approach is now to demonstrate the effect of each source of uncertainty individually. Afterwards, the influences can easily be compared to the theoretical prediction. As was described before, the first step during the geometrical reconstruction is to determine the ambiguous values for α_y before these value are used for the α_x reconstruction. The same strategy was followed for the performance test: Simulations of charged particles were performed to determine α_y and the contributions that affect α_y were studied. The same was then done for α_x before the results of both steps were combined to determine θ_C.

For the tests, 10 000 single track events with identical track parameters were simulated. In order to avoid effects related to hadronic interactions, muons with momentum $p = 1\,\mathrm{GeV}/c$ were chosen as test particles. The muons originate from the interaction point in PANDA, with a polar track angle of 25° on a trajectory to traverse the plate perpendicular in azimuth direction. 25° is (cf. Fig. 2.6) a typical angle within the Barrel DIRC angular acceptance and many Cherenkov photons are created since the path of the charged particle within the radiator is long. For reasons explained in Ch 3.1 the simulation does not contain a magnetic field, no glue and grease layers, and no realistic photon sensors. In addition, exact track and photon start positions and times are used which are, of course, not available in a realistic scenario. Only photons with a wavelength between 400 nm and 700 nm are accepted by the reconstruction. Shorter wavelengths will be cut off by the glue and longer wavelengths by the quantum efficiency of the sensors. The simulation assumed a prism opening angle of 45° and a backplane equipped with 3×5 photon sensors for complete spatial coverage.

The only contributions affecting the resolution of α_y are the pixel size and the plate thickness because the determination of this angle does not require knowledge of the track and the specific photon path. The effects were minimized by using a plate thickness of 0.2 cm to minimize σ_{bar} and a non-pixelated sensitive plane to eliminate σ_{pix}. The step between the bottom of the plate and the bottom of the prism (see e.g. in Fig.3.5) is 1 cm deep to have a separation of photons heading towards positive Y-direction and towards negative Y-direction on the sensor plane.

Figure 3.12a shows the difference of the reconstructed α_y and the real angle $\alpha_{y,\mathrm{MC}}$ of the simulated photon. The central part of the distribution has a width of $\sigma = (1.425 \pm 0.004)\,\mathrm{mrad}$ and peaks at $\Delta\alpha_y = (2.43 \pm 0.75) \cdot 10^{-2}\,\mathrm{mrad}$. The expected resolution of the main peak results from the thickness of the plate (0.2 cm) and the distance to the prism backplane (30 cm). If the photon exits the plate near

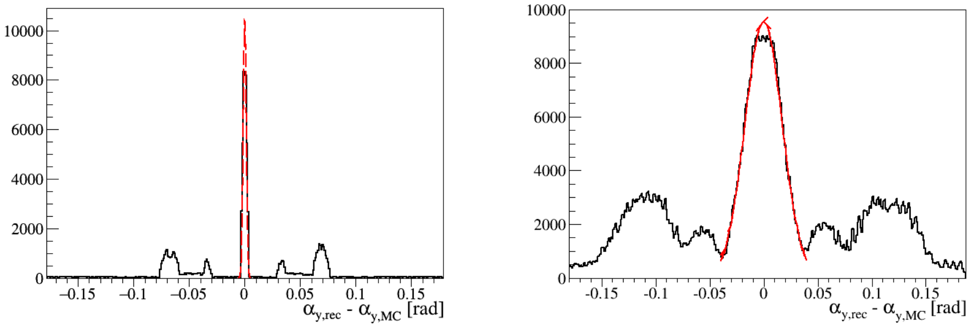

(a) Thin plate (0.2 cm) and unpixelated sensor plane.

(b) Realistic plate thickness (1.7 cm) and sensor pixelization (0.65 cm).

Figure 3.12: Difference of the reconstructed α_y and the real simulation angle $\alpha_{y,\mathrm{MC}}$. The result of a Gaussian fit to the center peak is marked in red.

the top or the bottom surface and propagates towards the readout plane parallel to the X-Z plane, the difference of α_y and $\alpha_{y,\mathrm{MC}}$ takes a value of

$$\Delta\alpha_y = \arctan(0.1\,\mathrm{cm}/30\,\mathrm{cm}) = 3.3\,\mathrm{mrad}. \tag{3.14}$$

In general, this difference is much smaller, as the photon does not travel parallel to the X-Z plane and does not exit the plate at the top or the bottom surface. The width of the peak is, therefore, consistent with the expectation. The smaller peaks, symmetrical around the central peak, depend on the size of the prism step. The bigger peak, for example, is located at

$$\Delta\alpha_y = \arctan(2\cdot\mathrm{stepsize}/\mathrm{EV\ depth}) = \arctan(2\cdot 1\,\mathrm{cm}/30\,\mathrm{cm}) = 66\,\mathrm{mrad}. \tag{3.15}$$

Figure 3.12b shows the same study for realistic values of the plate thickness and the pixel size. With a thickness of 1.75 cm and a pixel size of 0.65 cm, an analogue approach to Eq. 3.14 yields for the central peak a maximum difference of

$$\Delta\alpha_y = \arctan\left(\frac{\mathrm{thickness}/2 + \mathrm{pixel\ size}/2}{\mathrm{EV\ depth}}\right) = 40\,\mathrm{mrad} \tag{3.16}$$

which is in agreement with the central peak width of $\sigma = (17.19 \pm 0.03)\,\mathrm{mrad}$ in Fig. 3.12b.

Using Eq. 3.7, α_x can be calculated. The chromatic dispersion has an influence on the reconstruction of α_x, as Fig. 3.10 illustrates. The difference $\Delta\alpha_x$ of the reconstructed α_x and the real angle $\alpha_{x,\mathrm{MC}}$ can be seen in Fig. 3.13. The realistic simulation with the α_y values from Fig. 3.12b was used.

The central peak is very narrow ($< 1\,\mathrm{mrad}$) since σ_{α_x} is, in good approximation,

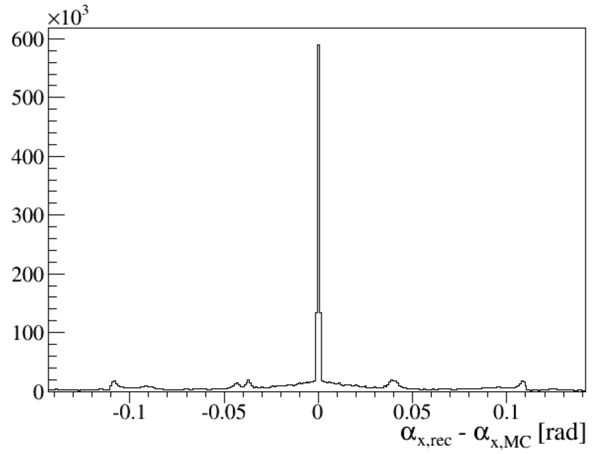

Figure 3.13: Difference of reconstructed α_x angle and real angle $\alpha_{x,\mathrm{MC}}$.

given by the ratio of the pixel size and the photon path length (several meters). The width of the peak increases with shorter photon paths (i.e. with higher track polar angles). The other ambiguities are spread widely in the remaining spectrum. They originate on the one hand from chromatic dispersion. Since the propagation time of the photon is taken to be exact within a (sensor) time resolution of 100 ps, the different possible photon velocities result in different path lengths and, therefore, different hit coordinates on the unfolded readout plane (compare the red dashed lines in Fig. 3.8). Some of these ambiguities accumulate in the smaller side peaks. On the other hand, many ambiguities are caused by wrongly reconstructed values of α_y, which are used in the determination of α_x. Even for these class of ambiguities, many values of $\Delta\alpha_x$ can be located in the central peak, as the photon start and end location is well determined and the real position x_u on the unfolded readout plane could be found during reconstruction.

Cherenkov angle reconstruction

The results for the reconstructed α_x and α_y can now be combined, using Eq. 3.12 and 3.13, to yield the photon polar and azimuth angle in the coordinate system of the plate. The physical condition for total internal reflection is used to reject some of the reconstructed photon ambiguities. This sharp cut is applied, because photons hitting the radiator surface with an incident less than 42° do not reach the sensor plane. Reconstructed photon ambiguities with Cherenkov angle values above 1000 mrad are unphysical and rejected as well. The number of ambiguities is given by the number of α_y-ambiguities (equal or less than 16 in a prism with 45° opening angle), multiplied with the average number of ambiguities from the X-Z reconstruction (≈ 10, depending on z_u or, equivalently, the polar angle of the charged particle track).

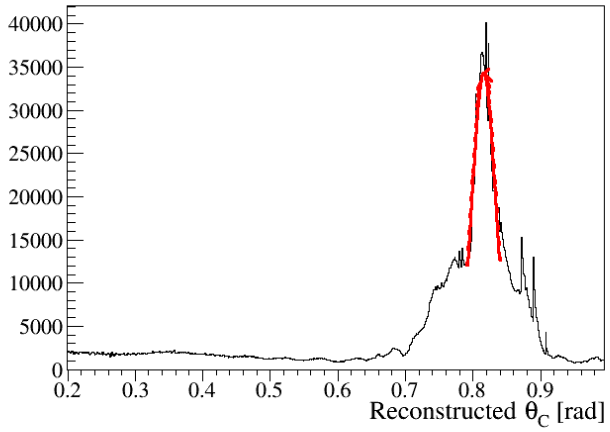

Figure 3.14: Distribution of reconstructed Cherenkov angles obtained by geometrical reconstruction. For the tests, 2 000 muons with a track polar angle of 25°and a momentum of 1 GeV/c were simulated. All resolution contribution effects were set to realistic values. The red line highlights the result of a Gaussian fit to the narrow peak of the structure.

The result of the Cherenkov angle reconstruction is shown in Fig. 3.14. A prominent peak is placed on top of a broader structure and a constant underground. A fit of a Gaussian function gives a position of $\theta_C = 816.6\,\mathrm{mrad}$ for the peak, which is in agreement with the theoretical prediction of $\theta_C = 817.4\,\mathrm{mrad}$.

The width of the peak is 16.6 mrad. The broad distribution below the peak has a complicated shape and is created by combinatorial background and pixelation effects. The distribution forms a significant part of the reconstructed θ_C-distribution and is the cause for a very unfavorably signal-to-background ratio. Studies of the composition of this background and methods to suppress it were performed and will be described in the remaining part of this chapter.

The main influences on the reconstruction of the single photon Cherenkov angle are the plate thickness, the pixel size, and the chromatic dispersion. Figure 3.15 shows how these effects act on their own or in combination with each other in different scenarios. The left column of the figure shows the results from the Cherenkov angle reconstruction for simulations with a thin plate (2 mm thickness); the right column shows the result for a realistic plate thickness (17.5 mm). By moving down the rows, the simulations evolve from idealized to more realistic scenarios. The top row represents the scenario with perfect hit position information (no pixels) and a small photon wavelength range between 398 and 402 nm to disable dispersion effects. In the second row, a scenario with realistic pixel sizes is shown, while for the third row a broader wavelength spectrum between 300 nm and 400 nm was used. The fourth row shows the full wavelength spectrum scenario with a non-pixelated sensor plane and in the last row all effects are included. In each plot, the resolution of the main

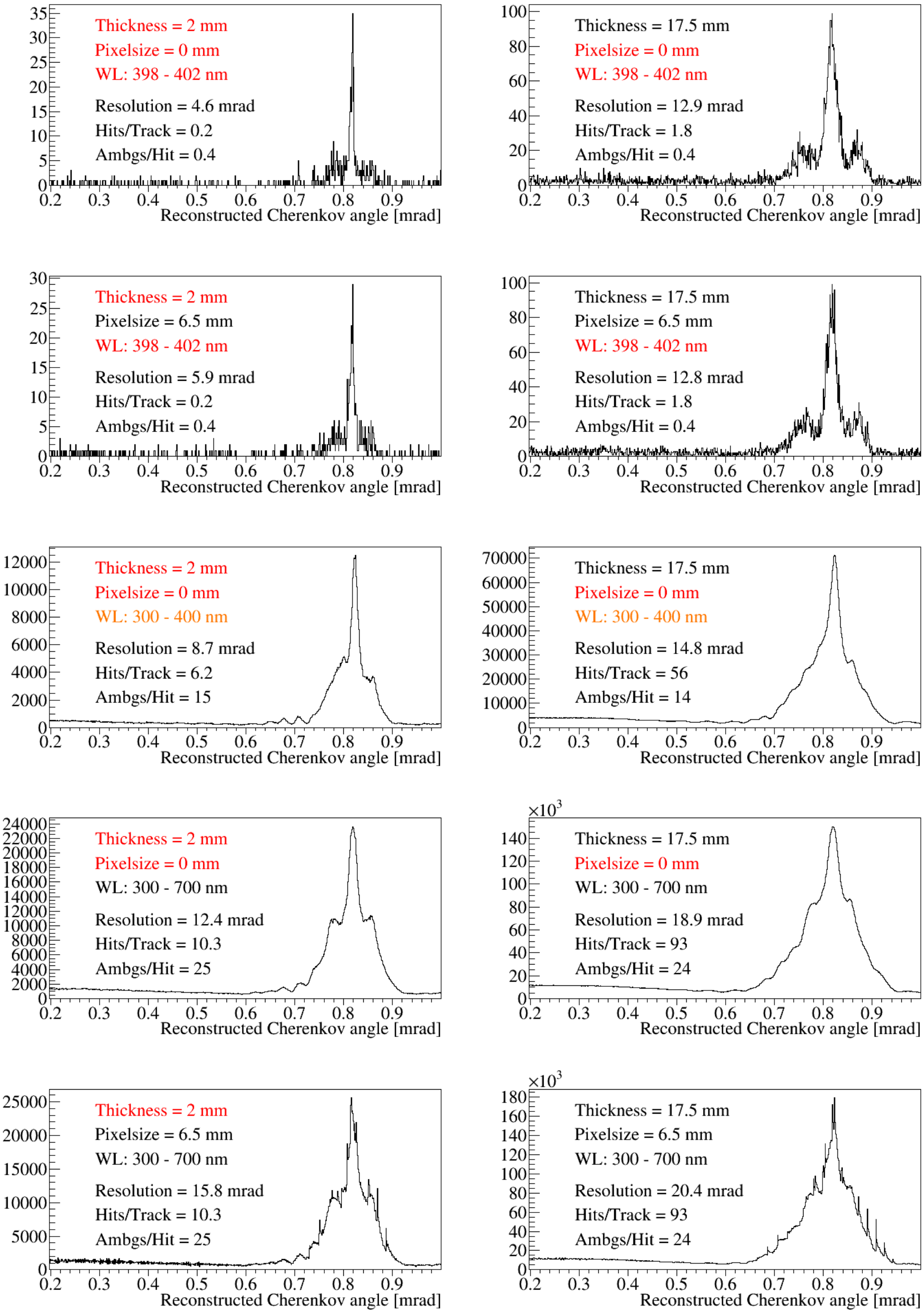

Figure 3.15: Study of the influences on the PID capability. For each scenario, 10 000 muons were simulated with θ=25°, and p=1 GeV/c. Text in red: idealized values; orange: semi-idealized.

peak or of the peak on top of the broad distribution for the lower rows is shown as well as the number of photon hits per track and the number of reconstructed θ_C-ambiguities per simulated photon hit.

It is a trivial fact, that the number of photons per hit is smaller for a thin plate (left column) than for a thicker plate. For the scenarios in the right column, a plate thickness roughly 9 times higher than in the scenarios on the left was used, and this ratio is reflected in the number of hits per photon between two scenarios in the same row. The number of hits per track is further reduced in the narrow wavelength range scenarios. The number of ambiguities per hit is fully determined by the number of α_x-ambiguities, since only geometrical considerations (opening angle of the prism) have influence on the number of α_y-ambiguities. In the scenarios of a narrow wavelength range, only one or zero values for x_u can be found (see Fig. 3.10). If the true α_y-ambiguity and one value for α_x was found, the reconstructed Cherenkov angle is very close to the real value.

Not much changes in the scenarios of the pixelated sensor plane (second row from the top). The pixel size only affects the reconstructed α_y-ambiguities. The effect on the uncertainty of the α_x values is negligible, since the pixel size is very small compared to z_u, which is used to determine α_x. In the right scenario the θ_C-resolution is even the same as in the non-pixelated scenario (top row), since the resolution is dominated by the contribution of the plate thickness.

The broader wavelength range (rows 3-5) has an effect on the θ_C-resolution and adds the large background structure to the θ_C-reconstruction. This can be explained by dispersion: Many more values for x_u are found between the extreme cases of the accepted photon wavelength (Fig. 3.10) and the number of α_x-ambiguities increases. The effects of dispersion are stronger at smaller wavelengths (see Fig. 2.18), so by cutting away the shorter wavelengths the θ_C-resolution would theoretically improve. Unfortunately, Cherenkov photons are preferably emitted in the lower wavelength spectrum (see Eq. 2.2), so the cut into the shorter wavelength spectrum, to improve the resolution, comes with the downside of losing the major part of the photons.

The bottom row displays pixelated versions of the scenarios in the fourth row. The same argument as in the second row is valid and the resolution does not change much. Sharp spikes appear in the spectrum due to pixelation effects.

Conclusion

It was shown that the geometrical reconstruction approach is able to find the correct Cherenkov peak position for the setup with wide radiator plates. However, the reconstructed spectrum is dominated by the combinatorial background and only a small part of the reconstructed angle spectrum corresponds to the actual signal. The biggest contribution to this background comes from chromatic dispersion which is an effect that can be, in principle, mitigated by applying optical band filters between radiator and EV. The influence of dispersion is largest in the shorter wavelength regime (Fig. 2.18), which is unfortunately the region where most of the photons are generated (Eq. 2.2). Optical filters would mitigate the effects of dispersion but also drastically reduce the number of photons, prohibiting a successful θ_C-reconstruction. Other problems arise with the transition to more realistic geometries. Issues such as the reduced acceptance of the sensor plane due to gaps between sensors or a more complicated calculation of the photon paths due to applied focusing optics are not discussed here. The geometric reconstruction is not applicable in this form and has to be discarded. It will, however, be shown later (Ch. 3.6) that a version of the principle method can successfully be applied to find the equations for an analytical description of the PDFs of the time-based likelihood reconstruction approach.

3.5. Time-based Likelihood Function

A different reconstruction approach follows methods developed for the Belle-II TOP counter (Ch. 3.3) [57]. The goal of this method is to provide likelihoods values for each track and particle hypothesis. The corresponding PDFs are based on the observed photon hit position and propagation time. Before deriving analytically the PDFs, a proof will be given that the reconstruction principle works.

The log-likelihood function $\log L_h$ is defined as

$$\log L_h = \sum_{i=1}^{N} \log \left(\frac{S_h(x_i, y_i, t_i) + B(x_i, y_i, t_i)}{N_e} \right) + \log P_N(N_e), \tag{3.17}$$

with the signal distribution S_h of particle hypothesis h, the background distribution B, the expected number of sensor hits N_e, including signal and background hits, and the number of measured hits N (further explanations are found in Ch. 3.3). The distributions S_h depend on the particle type as well as momentum and direction. They are simulated with specific charged particle parameters while B is estimated from the dark noise of the photon sensors. After Eq. 3.17 was used to determine values for $\log L_h$, likelihood ratio tests are performed to select the particle hypothesis h with the highest likelihood ratio (or, equivalently, log likelihood difference). In the course of this work, kaons and pions are compared, and the value of the log likelihood difference $\log L_K - \log L_\pi$ is determined to separate kaons from pions.

The precision of the PDFs increases with the number of simulated particles used to create them. Typically about 10^5 particles with the same parameters are generated for the simulation (for details on the simulations see Ch. 3.1) and the computing effort for the simulation is very high. During the running PANDA experiment, online simulations to produce PDFs with a good accuracy are not possible. The PDFs could in principle be calculated and stored beforehand, but the high dimensional input parameter space (particle type, particle momentum and direction) would require an enormous amount of stored data. Furthermore, static look-up tables would be very inflexible if environmental changes in the PANDA experiment or detector occurred. For these reasons, analytical expressions are desired, where the values of S_h can be calculated quickly and with high precision, depending on the particle information of the tracking systems in the PANDA detector. A derivation of these expressions will be given in Ch. 3.6.

Description of the Photon Hit Patterns

The principle of the time-based likelihood approach is explained in the following sections on the basis of a simulation of pions and kaons with 3.5 GeV/c momentum and 22° polar track angle, with the geometry shown in Fig. 3.16. To investigate the influence of focusing optics, a second configuration was simulated with a cylindrical, two-component compound lens (Fig. 3.17) that was designed and manufactured for application in the prototype tests. The lens provides focus in one dimension and consists of fused silica and high refractive index NLak33. The components of the lens have a curved surface with the same radius but opposite signs, so that they are arranged such that the whole lens is box-shaped. The lens can thus be connected between radiator and prism, that no air gaps occur between the surfaces. This arrangement has the advantage that fewer photons are lost at the lens interfaces as the refractive indices of the lens components are much closer to each other than with a configuration with a curved lens and an air gap, where photons with steep angles would get reflected on the fused silica/air interface.

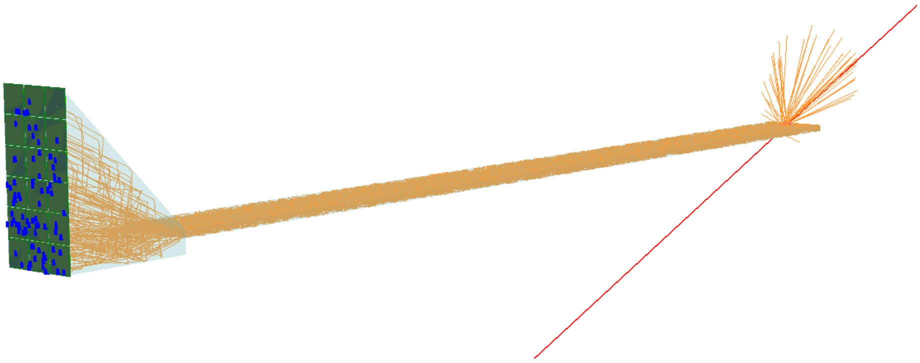

Figure 3.16: Event display of the simulation of a single pion event with $\theta = 22°$ and $p = 3.5\,\mathrm{GeV}/c$. The geometry contains a single segment of the DIRC barrel. The plate is directly attached to the EV without lens. The pion trajectory is shown in red, the Cherenkov photon trajectory in orange and the hits on the detector plane in blue.

The full usage of all three observables X, Y, and T is an important difference to the geometrical reconstruction, where the time is only used to define the extreme cases of the possible projected photon paths between which the α_x-ambiguities

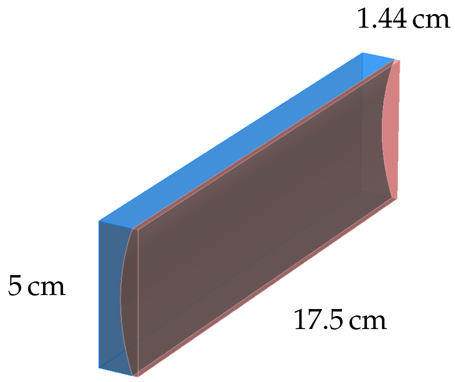

Figure 3.17: Simulated two component lens. The right face of the lens, highlighted with red color, is connected to the radiator and consists of NLak33. The material of the left side is fused silica [59].

are located (Fig. 3.10 and Eq. 3.7). The quality of the time-measurement does not have a big effect on the performance of the geometric reconstruction, whereas in the time-based likelihood approach, a good time resolution is as important as a good spatial resolution of the photon detection. Figure 3.18 shows the hit pattern as combination of two of the observables after simulating 10^5 pions. In order to understand the composition of these patterns, the simulation does not contain a smearing of the particle tracks, time resolution of the readout sensors, or additional photon reflections at glue joints. The plot on the left side shows the occupancy of the sensor plane. The 18 sensors with 64 pixels each are clearly visible, and the pattern of the Cherenkov signal is most prominent in the pixels at $Y \approx 5\,\text{cm}$ and $Y \approx 14\,\text{cm}$. The Y-T spectrum shows, that this fraction of the photons arrives first on the sensor plane. The two parallel lines in this plot can be explained with the step between the bottom of the plate and the bottom of the prism. Photons with parallel trajectories are detected at the same time[3] but in pixels with different Y-coordinates, depending whether the last reflection in the plate occurred at the top or at the bottom surface. The darker parts of the signal, e.g. the early photons in the pixel region above $Y \approx 18\,\text{cm}$, are caused by additional photon reflections at the entry windows of the sensors and in the EV. In general, Cherenkov photon trajectories are directed tangentially on a characteristic cone, so the hit pattern is a conic section with a planar surface. A fraction of the photons are not totally internally reflected on the sides of the plate, so (continuous) parts of the section are lost. The remaining pattern is folded within the geometrical constraints by the prism, where especially the inclined surface (the "top") introduces distortion to the pattern.

The core of the approach is the (extended) likelihood function from Eq. 3.1. The

---

[3] Actually not at the same time but they have the same time of propagation before they reach the prism. Since the path of the charged particle through the radiator is short compared to the length of the radiator, all the Cherenkov photons, which are created along this path, are created at the same time in good approximation.

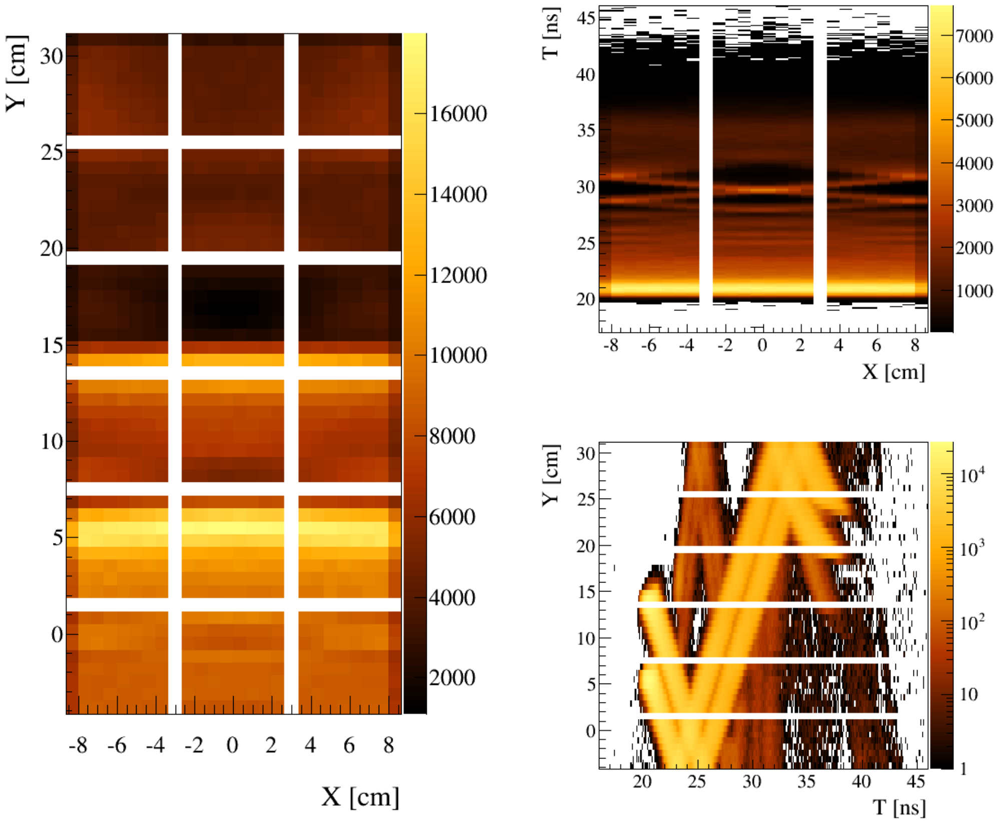

Figure 3.18: Photon hit pattern in X, Y, and T of 100 000 pions with $p = 3.5\,\mathrm{GeV}/c$ and $\theta = 22^\circ$. The time coordinate is binned with 100 ps, the spatial coordinates with 6.5 mm, which is the size of a pixel. The Y-T pattern is plotted with a logarithmic scale, in order to be able to see the features of the lowly occupied bins.

likelihood function is in general defined as

$$L(h) = f_h(x_1) \cdot f_h(x_2) \cdot \ldots \cdot f_h(x_i),$$

where f is the PDF, h a parameter of f, and $x_1, \ldots x_i$ are independent measurements of the random variable X.

Applied to Eq. 3.1, X is the photon hit position in space and time, h is the particle hypothesis, e.g. pions or kaons, and f is the (normalized) theoretical hit pattern density distribution. The spatial part of $S_h(x, y, t)$ is intrinsically binned by the channels of the pixelated photon detection plane (6.5 mm). According to the experimental requirements and the resolution limits of modern electronic readout chains, t is manually binned with 100 ps.

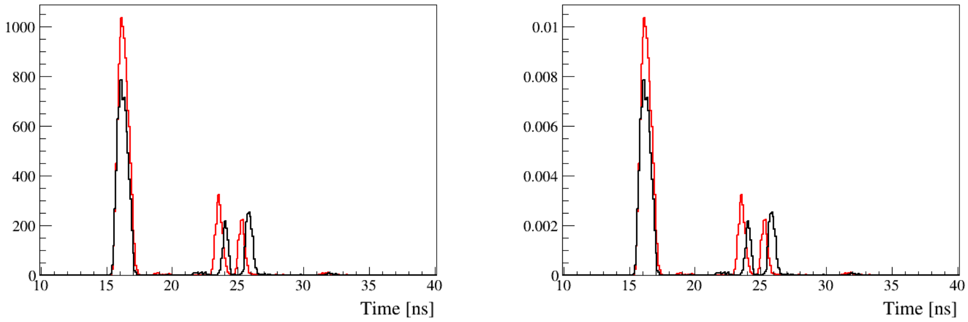

(a) Time distribution of 100 000 charged particle tracks.

(b) Normalized time distribution which is used in the likelihood determination.

Figure 3.19: Photon hit time distribution of a selected pixel, obtained with pions (red) and kaons (black) with $p = 3.5\,\mathrm{GeV}/c$ and $\theta = 22°$.

The photon hit time distribution of a selected pixel is shown in Fig. 3.19a. The red distribution is generated by pions, the black distribution by kaons. S_h is obtained (Fig. 3.19b) by dividing each distribution by the number of charged particle tracks, which results in S_h being normalized to the mean number of photon hits per track. The background distribution B is in good approximation a constant background, created by the dark count rate of the sensors. With a dark count rate of 1 kHz per channel and 100 ps bin width, B has in each time bin a constant value of

$$B = 1\mathrm{kHz} = 10^3 \frac{1}{s} = 10^{-7} \frac{1}{100\,\mathrm{ps}}.$$

For every hit per event, $\log(S_h + B)$ at the measured hit time and position is evaluated and summed up. The underlying assumption is, that the likelihood function $S_{h,\mathrm{true}}$ has, in average, a larger value for the true particle hypothesis h_{true} than for any wrong hypothesis.

The distribution of the number of photon hits per track follows a Poisson distribution which has to be considered in Eq. 3.1, as different charged particles create different numbers of Cherenkov photons. The differences of the detected hits statistics for pions and kaons can be seen in Fig. 3.20. As before, red represent the pion and black the kaon statistics. Particles with momenta of 1 GeV/c and polar angles of 140° were simulated for this comparison, as the distributions of pions and kaons are very similar with 3.5 GeV/c particle momentum. The expected number of photon hits per event can be taken from this distribution. This is of importance for the correct normalization in Eq. 3.1 (N_e is the number of expected signal photons plus the expected background hits).

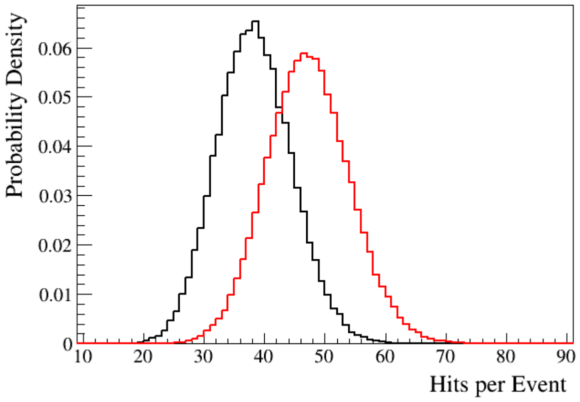

Figure 3.20: The photon hit multiplicity is described by a Poisson distribution. Pions (red) and kaons (black) with $p = 1\,\mathrm{GeV}/c$ and $\theta = 140°$ were simulated. The expected number of Cherenkov hits from pions is higher than from kaons, as described by the Frank-Tamm equation 2.2.

The expected number of background hits can be calculated with the dark count rate, the considered time window of 100 ns per event, and the number of channels. For 15 sensors with 64 pixels per sensor, it yields $N_B = 1\,\mathrm{kHz} \cdot 100\,\mathrm{ns} \cdot 64 \cdot 15 \approx 0.1$ hits per event.

More examples of hit patterns can be seen in Fig. 3.21. The X-Y pattern of kaons with $p = 3.5\,\mathrm{GeV}/c$ and $\theta = 22°$ is shown in Fig. 3.21a. It has a very similar appearance to the pion pattern in Fig. 3.18 and is shown here to emphasize the fact that the X-Y hit patterns are in general not sufficient enough to deliver pion/kaon identification. Since the difference of the Cherenkov angle is very small, the early parts of the photons are detected in the same pixels. Only in the darker part of the plot, above $Y = 15\,\mathrm{cm}$, small differences in the patterns are visible. A study of the contribution of early and late photons to the SP will be discussed later. The other two plots show simulations with $p = 1\,\mathrm{GeV}/c$ and $\theta = 140\,°$. Due to the low momentum, the hit pattern of kaons (Fig. 3.21b) can be distinguished from the hit pattern of pions (Fig. 3.21a), even in the 2D pattern.

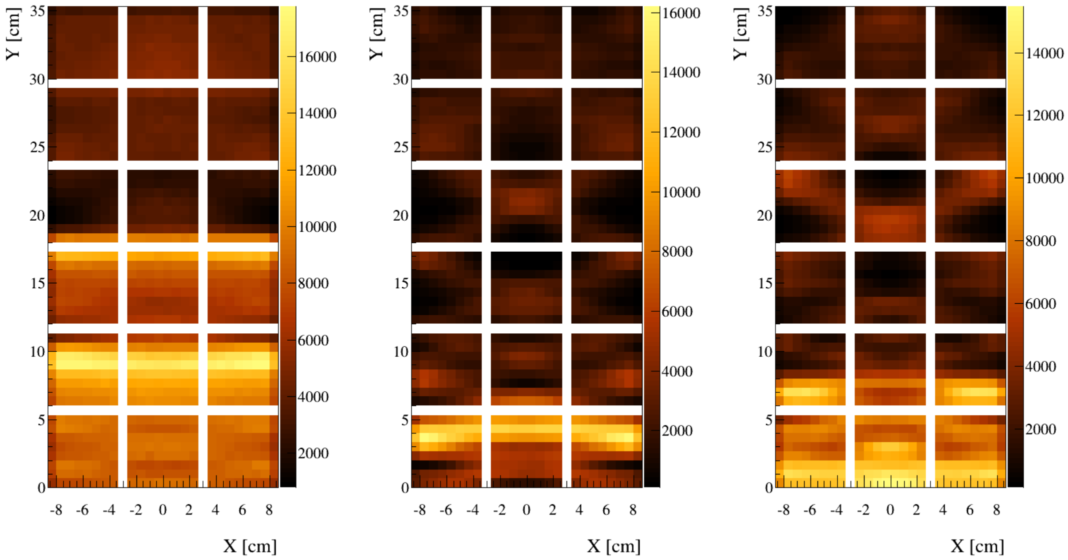

(a) Kaon pattern with $p = 3.5\,\mathrm{GeV}/c$ and $\theta = 22°$.

(b) Kaon pattern with $p = 1\,\mathrm{GeV}/c$ and $\theta = 140°$.

(c) Pion pattern with $p = 1\,\mathrm{GeV}/c$ and $\theta = 140°$.

Figure 3.21: Simulated sensor occupancy maps for different tested scenarios. Each pattern contains the Cherenkov photon hits of 100,000 charged particles.

Likelihood Ratio Test

The resulting likelihoods L_{h_i} for the particle hypotheses h_i can be assigned to the hypotheses for the global PID calculations or compared to each other by taking the difference $\log L_{h_1} - \log L_{h_2}$ of likelihood logarithms. Figure 3.22 shows log likelihood differences $\log L_K - \log L_\pi$ for pion (red) and kaon (black) samples. For each distribution, 1 000 test particles have been simulated. If the likelihood value for the pion hypothesis is higher than for the kaon hypothesis for a single particle, the difference turns out to be negative, otherwise it is positive. The two curves in each plot are clearly separated and normally distributed. The mean values and widths of the distributions do not have any physical meaning (other than the determination of the separation power, introduced in Ch. 2.6.3), as the likelihood itself is only a comparative figure. The only statement that can be made is that if the log likelihood difference is positive, the particle can be associated rather with the kaon hypothesis, a negative value indicates a better match with the pion hypothesis. Cuts on $\log L_K - \log L_\pi$ can be set to meet the requirements of PID efficiency and misidentification.

The SP calculation now yields (7.2 ± 0.2) standard deviations (s.d.) for the $3.5\,\mathrm{GeV}/c$

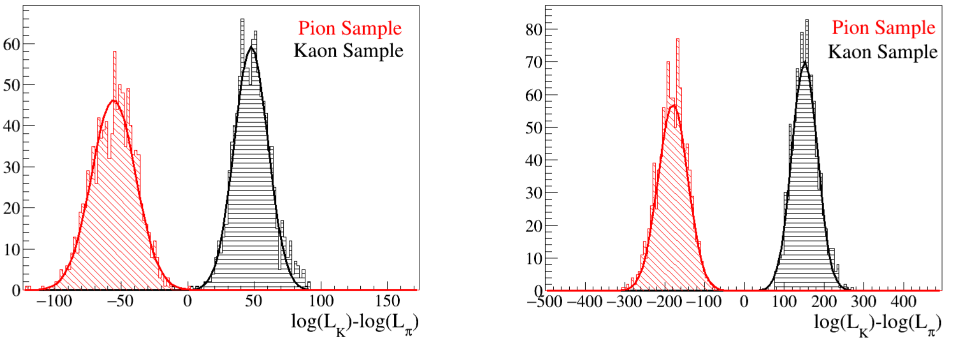

(a) Pion and kaon sample; $p = 3.5\,\mathrm{GeV}/c$, $\theta = 22°$.

(b) Pion and kaon sample; $p = 1\,\mathrm{GeV}/c$, $\theta = 140°$.

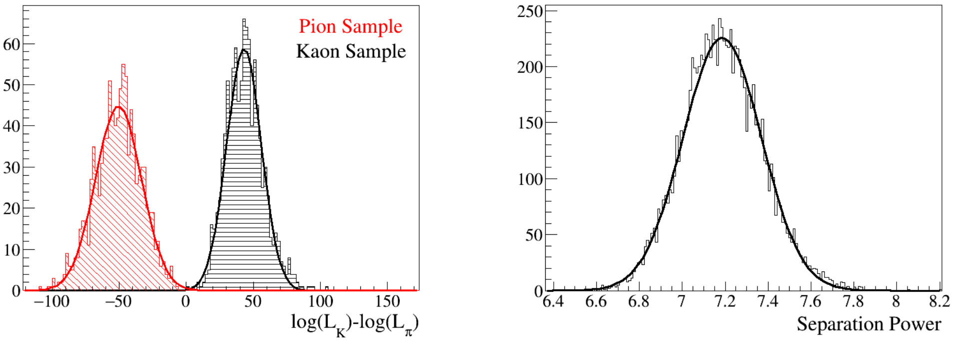

(c) Pion and kaon sample; $p = 3.5\,\mathrm{GeV}/c$, $\theta = 22°$. The simulation was done with magnetic field, the geometry contains glue joints between plate and prism.

(d) Separation Power distribution for the high momentum tests. The distribution is obtained by a resampling method known as bootstrapping.

Figure 3.22: Results of the likelihood ratio tests, performed with 1 000 charged particles of each kind. A clear separation between the simulated pions and kaons is visible in the investigated scenarios.

tracks (Fig. 3.22a) and (9.8 ± 0.3) s.d. for the 1 GeV/c tracks (Fig. 3.22b). A more realistic geometry with glue joints between the optical components and the magnetic field of the PANDA solenoid was simulated for the results shown in Fig. 3.22c. The SP value still fulfills the requirements ($SP = (6.4 \pm 0.2)$ s.d.) and is close to the value obtained with the simple geometry. The magnetic field forces the charged particle on a curved, non-symmetric track through the bar. This trajectory was also present in the simulation for the creation of the PDFs, so it seems reasonable that the field does not have an influence on the separation performance. The slightly worse SP value can be attributed to the glue joint between bar and EV, where a small fraction of the photons is reflected. The uncertainty on the SP measurements can be obtained either by repeated simulation and measurement, or, as done here, by resampling methods such as bootstrapping [60], which is exemplarily displayed in Fig. 3.22d for the high momentum track. The investigated cases match the performance criteria of the Barrel DIRC very well.

A detailed study was carried out for many points of the Barrel DIRC phase-space acceptance region (introduced with Fig. 2.6). Figure 3.23 shows the results with the idealized geometry without focusing in Fig. 3.23a, and with glue joints and focusing in Fig. 3.23b. All points in the diagram show sufficient π/K separation.

It is surprising that the setup with the lens shows worse performance, although a significant improvement to the unfocused setup is expected. The lens has to be coupled to the radiator and the prism with optical grease, so additional interfaces are introduced between the optical materials. This leads to a photon loss due to back reflections of a fraction of the photons, which depends on the track polar angle of the charged particle. For angles close to $\theta = 90°$, all the Cherenkov photons have a large incident angle (between photon direction and surface normal) at the lens surface. All photons would be totally internally reflected on the fused silica/air interface of a lens with air gap. This is not the case with the NLak33 lens but the reflectivity is nevertheless higher for photons with larger incident angles. For track polar angles different from 90°, many of the photons reaching the readout end of the plate have less steep angles, so the reflectivity is smaller. For the high momentum studies with track polar angles of 35°, 17% of the photons were lost at the glued interface between plate and prism. Another reason for the worse performance could be the fact that the focus of the lens is not optimized for the tested DIRC geometry. Figure 3.24 shows a Geant4 simulation of the focal plane (red curve) in Y-Z projection for the cylindrical lens depicted in Fig. 3.17. Photons were emitted from a point source near the end of the radiator and imaged through the lens. The superposition with the prism shows that the light is only focused sharply in the middle of the sensor plane, whereas in the top and bottom part of the plane the light is out of focus.

It was observed in several simulations and beam campaigns with the PANDA Barrel DIRC baseline design (using narrow bars as radiators), that, despite of the mentioned reasons, the reconstruction performance increases even with non-optimized lenses. The reconstruction method, however, was the BaBar-like reconstruction,

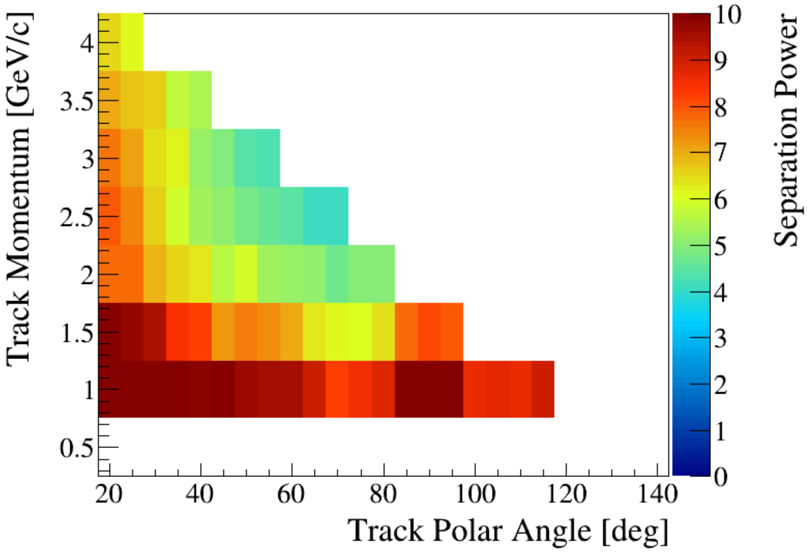

(a) Phase space scan with a DIRC geometry not containing focusing and glue joints between plate and EV.

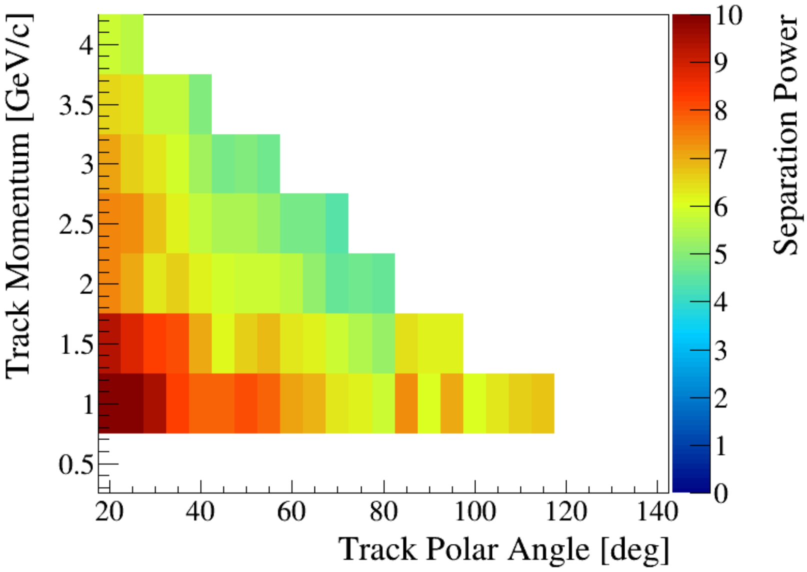

(b) Phase space scan with a DIRC geometry including a focusing, cylindrical NLak33 lens and glue joins between plate, lens and EV.

Figure 3.23: Likelihood ratio tests were performed for all relevant Barrel DIRC acceptance phase space points. All tests were able to deliver sufficient pion kaon separation. The scale of the SP is capped at a value of 10.

which is fundamentally different from the time-based likelihood approach. Conclusions drawn from investigations of focusing options for one reconstruction approach cannot be transferred to the other approach. A possible explanation for the worse performance of the lens based geometry is, that the requirements on the lens concerning the position of the focal plane is higher for the time-based likelihood approach.

A very close approximation of the focal plane with the sensor plane can be achieved by using lens systems with one or several focusing and defocussing stages, realized with different optical materials. A spherical 3-layer lens was designed and produced for beam tests with the narrow bar geometry. Such lenses do not exist yet for the radiator plate but the research is in progress [59].

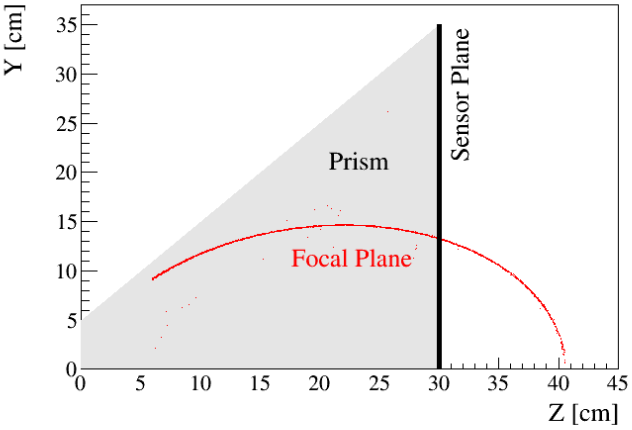

Figure 3.24: The focal plane of the simulated lens is displayed in red. The prism is drawn in gray. A comparison of the focal plane and the backplane of the EV shows that the choice of the lens geometry is not optimal [59].

Separation Power of Early and Late Photons

The reconstruction approach strongly depends on the correct photon hit time definition. It can be seen in Fig. 3.18 that many photons arrive early (at times around 20 ns in the depicted simulation) while at later times fewer photons are detected. The early photons are the ones which propagate more or less directly towards the readout plane (or the mirror, depending on the initial track direction). Since they experience the least number of surface reflections and the shortest paths in the bulk material, they have the highest detection probabilities. In Fig. 3.19 the hit time distribution of a single pixel is shown. The two PDFs have a strong overlap in the early part of the distribution, whereas in the later part, the differences are apparently larger. These two observations raise the question whether the early or the late photons have a bigger impact on the reconstruction performance.

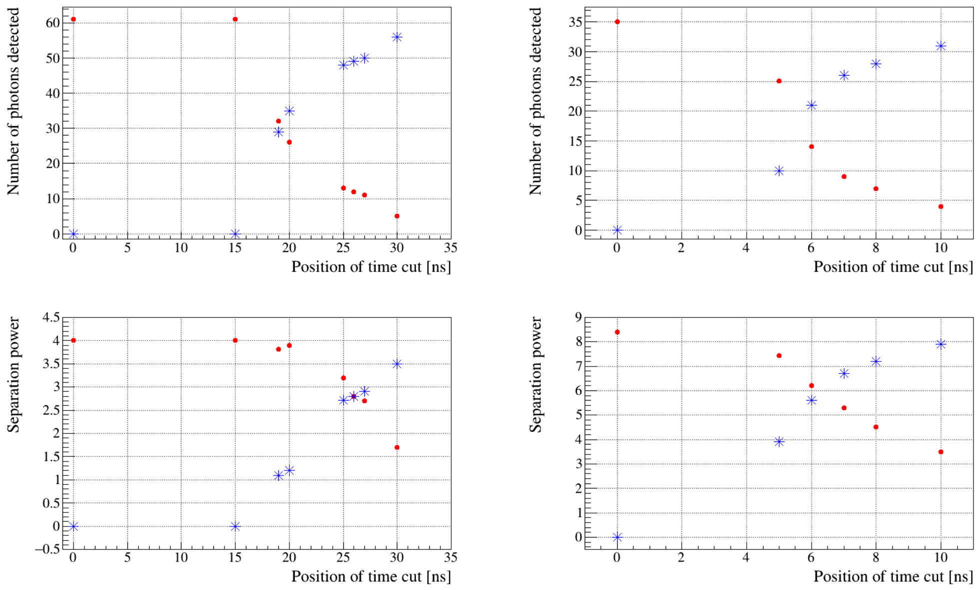

(a) Track momtentum $p = 4\,\mathrm{GeV}/c$, polar angle $\theta = 22\,°$.

(b) Track momtentum $p = 1\,\mathrm{GeV}/c$, polar angle $\theta = 140\,°$.

Figure 3.25: Study of the influence of the photon detection time on the reconstruction performance. Time cuts were applied during the PID. The number of photon hits (of pions) with smaller hit times and the corresponding SP are displayed in blue. The number of hits after the time cut and the corresponding SP are displayed in red. Both values are plotted against the position of the time cut.

Simulations with pions and kaons with $p = 4\,\mathrm{GeV}/c$ momentum and $\theta = 22^\circ$ polar angle, and with $p = 1\,\mathrm{GeV}/c$ and $\theta = 140^\circ$ were performed to investigate the issue. The plate was coupled directly to the EV, and the PDFs and the test particles were created as usual. A time cut was applied for the likelihood determination and the likelihood ratio test. In one case only Cherenkov photons with hit times smaller than the cut value were used for the PID, in the other case, photons with larger hit times were used. Figure 3.25 shows the result of the study. The high momentum case is shown in Fig. 3.25a, the low momentum case in Fig. 3.25b. The number of photon hits of the pions before the time cut is shown in the upper plots in blue, the number of hits after the cut is shown in red. The photon yield from kaons is not displayed as it does not differ much in both cases. The red and the blue value at the same time cut position add up to the total number of detected hits The first photons in the high momentum simulation were detected with $T \approx 16\,\mathrm{ns}$. In the low momentum simulation the first photons were detected with $T \approx 4\,\mathrm{ns}$.

In the lower plot, the SP contribution of the first (blue) and the last (red) photons is shown. In this case, the vertical data points do not add up to a constant value. It can be seen in the upper plots, that the photon yield distribution in time does decrease approximately exponentially with the position of the time cut. The SP, however, does not show this behavior. In the high momentum study, the SP has a value of $4\,\sigma$ with all 61 photon hits and drops to $3.8\,\sigma$ with the 26 photon hits after the time cut. An SP value of $2.8\,\sigma$ is achieved with the first 49 hits and with the last 11 hits. The low momentum study draws a similar picture. The SP has a value of $8.4\,\sigma$ if all 35 photon hits are used in the reconstruction and a value of $7.4\,\sigma$ by using only the 25 hits after the cut. Similar SP values are achieved with the first 10 photons and with the last 4 photons (SP$\approx 3.8\,\sigma$) or with the first 21 photons and the last 9 photons (SP$\approx 5.4\,\sigma$).

The conclusion is, that the early photons do not carry as much information of the species of the initial particle than the later photons. This can be understood qualitatively: The first detected photons have the shortest propagation paths, where the small difference of the Cherenkov angle for pions and kaons does not contribute much to the different 3D hit patterns. The likelihood function yields similar values for the early hits with the pion and the kaon hypothesis. For long photon paths, i.e. high hit times, the difference is magnified due to a high lever arm and has an impact on the hit position difference of the photons of pions and kaons. It is, therefore, important to have a high detection efficiency for the late photons. This point stresses again the need for excellent quality of the radiator surfaces.

Influence of Parameter Uncertainties on the Separation Power

It is interesting to see how stable the method is against parameter variations. Such variations occur, for example, during prototype tests due to uncertainties of the track

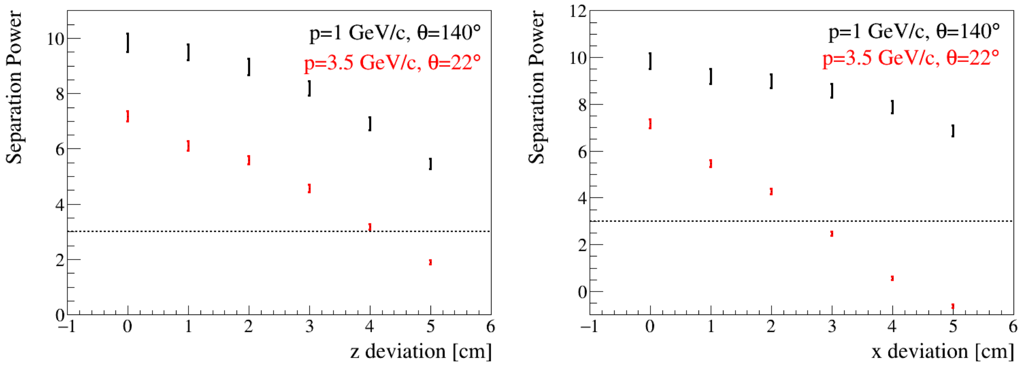

(a) z-position of the crossing of the charged particles with the plate.

(b) x-position of the crossing of the charged particle with the plate.

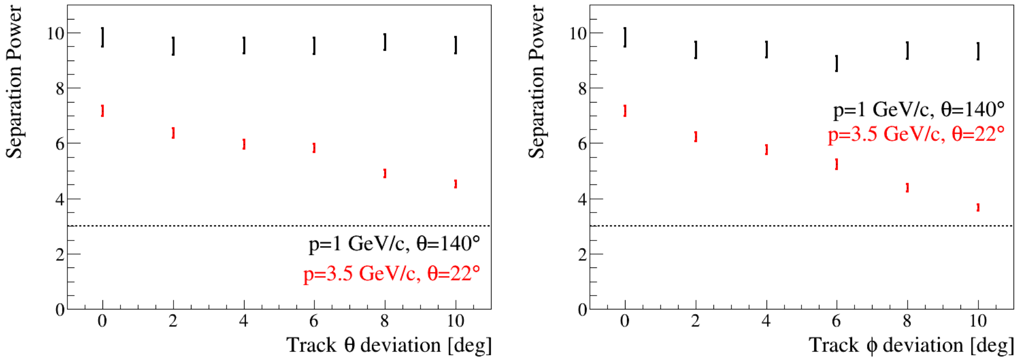

(c) Polar angle of the charged particles.

(d) Azimuth angle of the charged particles.

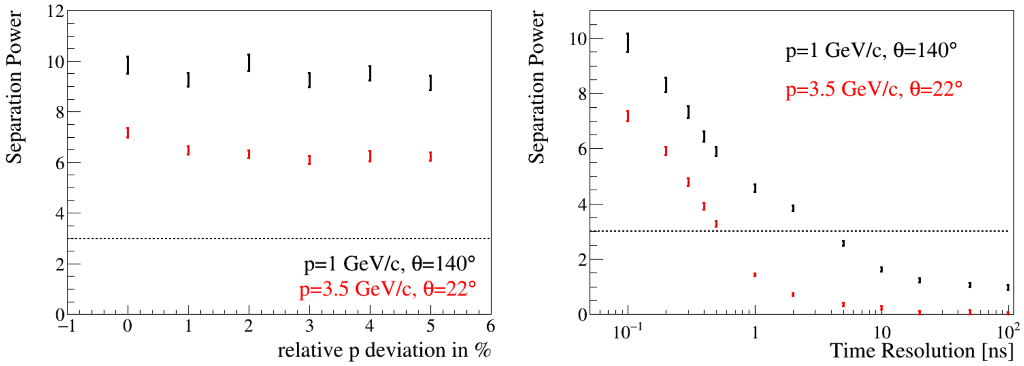

(e) Momentum of the charged particles.

(f) Sensor time resolution of the readout electronics.

Figure 3.26: Results of the variation measurements. Each plot shows the pion kaon SP after the selected parameter is varied while the others are fixed. The black dashed line highlights the 3σ-goal of the PANDA PID.

direction, misalignments (e.g. between radiator and EV), or unexpected behavior of the readout electronics. In case the analytic derivation of the PDFs is not successful or powerful enough, the PDFs will have to be simulated for the PANDA experiment. It was mentioned that this is an extensive task because of the multi-dimensional input parameter space. A variation study of the input parameters helps to identify the parameters with high requirements on accuracy for the reconstruction performance and the parameters with less severe requirements on accuracy. This information can be used to estimate the number of PDFs to be created. The variation study was performed by measuring and comparing the π/K separation. Two sets of track parameters were simulated in order to investigate the variation influence in a phase space region with larger separation ($p = 1\,\mathrm{GeV}/c, \theta = 140°$) and with smaller separation ($p = 3.5\,\mathrm{GeV}/c, \theta = 22°$). The geometry used did not contain focusing optics.

The tested parameters were the track momentum p, the x and the z-position where the track crossed the plate, polar (θ) and azimuth (ϕ) angle of the track, and the time resolution $\mathrm{d}t$ of the photon detection. For the $\mathrm{d}t$ measurements, photon sensors with the different $\mathrm{d}t$ values as time resolution were simulated for the creation of the PDFs. The time resolution of the photon hits of the test particles was set to $\mathrm{d}t$ as well. For the other parameter tests, the standard unchanged PDFs were used and the parameters of the test particles were varied with respect to the standard values.

The results are shown in Fig. 3.26. Studies of variations in z (Fig. 3.26a) and x (Fig. 3.26b) show that the necessity of a good spatial resolution of the track is more evident for high momentum particles. This can be understood, as the z-position where the charged particles cross the plate does not determine the photon hit position but the detection time. The high momentum hit patterns of pions and kaon resemble each other in the X-Y hit pattern (compare Fig. 3.18 and 3.21a), so a correct hit time has a larger impact on the reconstruction performance of high momentum particle than the spatial hit coordinates. A deviation of x does not significantly influence the hit time but it distorts the X-Y hit pattern. The influence on the reconstruction performance is not very evident. The assumption is, that the pion and kaon X-Y hit patterns still show differences for low track momenta after the distortion. The individual likelihood values are smaller but the likelihood ratio is high due to these differences. In the case of high track momenta, the likelihood values decrease and so does the likelihood ratio, since the X-Y-T hit patterns are similar for pions and kaons, and the SP is smaller anyway. Realistic values for the displacement of the reconstructed track at the PANDA experiment do not have a significant influence on the reconstruction performance as the spatial resolution of the particle track is expected to be better than 1 cm. The particle tracks during the prototype test are usually only defined within a few centimeters, so a good spatial resolution is crucial here.

A change in track polar angle induces a shift of the X-Y hit pattern in the Y-coordinate. Since the patterns for pions and kaons are shifted equally, no big effect on the SP is expected (Fig. 3.26c). The likelihood ratios do change however as the hit pattern of the kaon now resembles the PDF for the pion hypothesis or vice versa (Fig. 3.21b and 3.21c), which was recorded with the correct value of θ. In this case, the likelihood ratio for kaons is close to one, because the identification of kaons as pions is equally likely than as kaons. The likelihood ratio of the pions is much smaller than usual (i.e. the logarithm is more negative), since the comparison with the kaon hypothesis yields a very small likelihood value. A deviation of the track azimuth angle (Fig. 3.26d) has similar effects than a deviation of the x-value of the particle/plate crossing point. Since the momentum direction of the charged particle and the position of the plate intersection are very strongly correlated, and the polar and azimuth angle can be measured with a similar precision than the particle track position, angular resolutions smaller than 1° are expected. The decrease of the reconstruction performance with realistic values for track deviations is negligible.

The track momentum deviation was investigated up to 5%, because simulation studies of the PANDA Straw Tube Tracker showed a momentum resolution of 1.3% for low momentum particles ($p = 0.3\,\mathrm{GeV}/c$) and 3.6% for high momentum particles ($p = 5\,\mathrm{GeV}/c$) [18]. The results in Fig. 3.26e indicate that the time-based likelihood approach is also robust against momentum deviations.

The time resolution measurement is displayed in Fig. 3.26f, on a logarithmic scale. The larger the values for dt are the weaker the influence of the time measurement is on the reconstruction. The data point rightmost in the histogram at dt=100 ns corresponds to an exclusively spatial reconstruction, where just the X-Y hit patterns are evaluated. As explained in the introduction of this chapter, the time-based likelihood approach is a full 3D reconstruction and depends on X,Y, and T. On the one hand this is the strength of the approach, as the full hit information is used to yield the best possible separation. On the other hand this means that the time resolution can be the performance bottleneck. The plot shows that it is worthwhile to have a time resolution as good as possible (a few hundred ps and better) in order to have the best reconstruction performance.

3.6. Analytical PDFs

The time-based likelihood approach, introduced in the last chapter, provides excellent pion kaon separation with PDFs created with Monte Carlo methods. For the real experiment it is not practical to use simulation-based PDFs in look-up tables, as each PDF is simulated separately with 10^5 charged particles. Every set of parameters, including particle type, track direction, momentum, and position of the crossing of the particle through the plate, requires a unique PDF. Furthermore, it can be expected that not all of the optical components of the 16 segments of the Barrel DIRC are aligned during the assembly as accurate as in the simulation. If the symmetry of the Barrel DIRC segments is lost by such misalignments, another degree of freedom enters the parameter space. The time-based reconstruction approach is not feasible without a method to analytically determine the signal distributions S_h of Eq. 3.17. Analytical PDFs are created fast and only if needed, as soon as information of other PANDA systems is available.

The following derivation of the fundamental equations is inspired by the solution developed for the Belle-II TOP counter (Ch. 3.3 and [58]). It follows the same mathematical groundwork that was developed for the geometrical reconstruction approach (Ch. 3.4). The performance of the derived formulas can easily be compared with the simulated PDFs. For the approach described in this thesis, the unfocused geometry is used, as it simplifies the calculations. In addition, the optical grease and glue layers between all optical components is omitted to avoid additional reflections on the interfaces. If the fundamental equations satisfy the needs of the PID, more realistic geometries and different focusing options need to be included in the calculations.

The simulated geometry comprises a prism with an opening angle of 45°, a front face of 5 cm, and a step of 3 cm between the bottom of the prism and the plate (the same geometry was used for the studies of the time-based likelihoods in the previous chapter, see Fig. 3.16). A 3×6 sensor array with gaps of 0.7 cm between the sensors is used. A sensor comprises 64 quadratic pixels in a matrix of 8×8, with a size of 6.5 mm for each pixel. Figure 3.27 shows a simulation of the PDF, created by Cherenkov photons of 10^5 pions with momenta of $3.5\,\mathrm{GeV}/c$ and track polar angles of 22°. These plots are used as references in the following sections, as the results of the analytical derivation have to be compared with the simulation. Figure 3.27a shows the spatial Cherenkov photon hit pattern. This plot is a repetition of the X-Y hit pattern shown in Fig.3.18 since the same geometry and the same input parameters were used during the simulation. The green line was added to visualize a cut value on the center pixel column. The cumulated hit pattern in Y-T of the pixels under the green line (at $X = 0.3\,\mathrm{cm}$) is displayed in Fig. 3.27b. The pattern in this plot is a subset of the Y-T pattern in Fig. 3.18. Each horizontal line represents a pixel and the green line indicates again the position ($X = 0.3\,\mathrm{cm}$, $Y = 9.6\,\mathrm{cm}$) of a selected pixel. The time distribution of the photons in this pixel is shown in Fig. 3.27c. The principal features within the occupancy patterns were described and explained in Ch. 3.5. A transition from the 3-dimensional occupancy plots to 3-dimensional probability density functions is realized by normalization.

The cause of the failure of the geometrical reconstruction approach was the large number of photon vector ambiguities, which formed the combinatorial background in the reconstructed θ_C-distribution. Each of them was a possible photon vector and indistinguishable from the other solutions. This means, on a more abstract level, that the observed "signal", in terms of hit patterns, reconstructed quantities, photon sensor signals, etc., does not allow an unambiguous reconstruction of the input parameters, meaning the Cherenkov angle, the particle mass, photon start

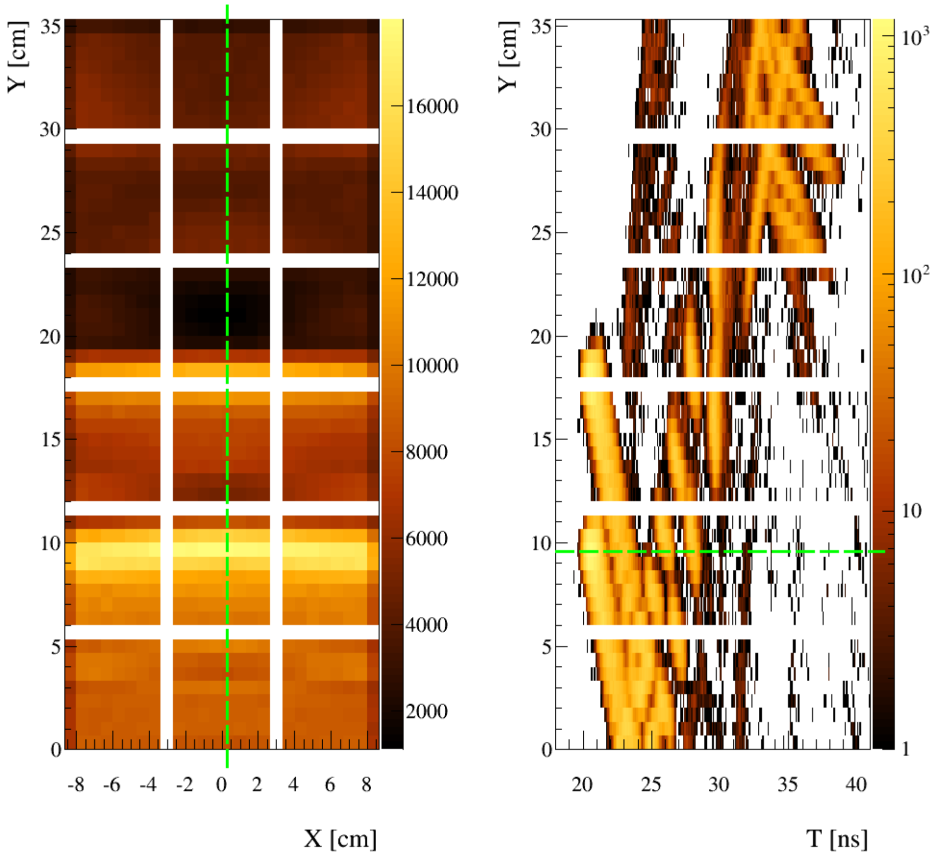

(a) Spatial hit pattern. The middle column is marked with a green line to indicate the pixels used for the Y-T distribution in the right plot.

(b) Y-T projection of the middle pixel column($X = 0.3\,\text{cm}$). The green lines highlights the position of a single pixel.

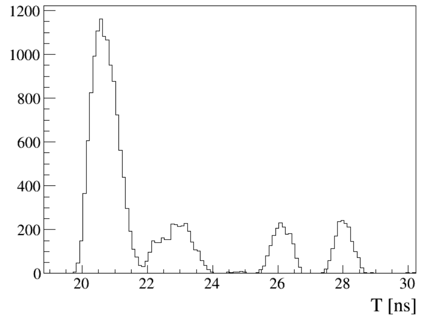

(c) T distribution of a single pixel (X=0.3 cm, Y=9.6 cm).

Figure 3.27: Simulated hit pattern in X, Y, T of 100 000 pions with $p = 3.5\,\text{GeV}/c$ and $\theta = 22°$.

directions, etc. It means also, from another point of view, that different sets of input parameters can yield the same observed signal. The conclusion in the context of geometrical reconstruction is, that each photon vector ambiguity contributes with a certain weight to the hit pattern in Fig. 3.27. One goal within the derivation of the PDFs is, therefore, to identify all the relevant photon vector ambiguities and the corresponding weights. The more ambiguities are found, the better the hit pattern can be approximated, whereas in the geometrical reconstruction approach the goal was the minimization of the number of ambiguities.

The Ansatz is made that for each pixel, the time distributions S are composed of m single Gaussian contributions (see Eq. 3.2)

$$S(t) = \sum_{i=1}^{m} n_i \cdot g(t - t_i; \sigma_i), \tag{3.18}$$

where m is given by the number of relevant ambiguities for this pixel. The mean value t_i is the calculated hit time of one photon path, the width σ_i corresponds to the spread of the hit time, and the height n_i is determined by the aforementioned weight of each ambiguity. The goal of the derivation in the following sections is to find equations for t_i, n_i, and σ_i. After an expression for a variable is found, the resulting total distribution $\sum_{\text{pixels}} S(t)$ over all pixels is compared qualitatively with the simulation in Fig. 3.27 and Fig. 3.18. The most revealing comparison is the time distribution in a single pixel and the Y-T hit pattern of the sensor plane.

Expression for the Mean Hit Time of the Photon Ambiguities

The variables used for the calculation of t_i are defined as shown in Fig. 3.28, a repetition of Fig. 3.3. Since the mathematical approach is very similar to the approach to identify the photon ambiguities for the geometrical reconstruction, many principles and variable names are reused. The photon vector is factorized into a component in the X-Z projection α_x and a component in the Y-Z projection α_y. The Y-coordinate of a photon hit is used to obtain the α_y ambiguities by calculation or from a database, as was done in the geometrical reconstruction. With a 45° prism, up to 16 ambiguities are possible, four coming from different reflection types in the prism (Fig. 3.5) and each of these with a reversed Y and/or Z component (Fig. 3.7). An α_y-value contains the information whether the initial photon direction was headed toward the mirror ($-180° < \alpha_y < 0°$) or the readout end ($0° < \alpha_y < 180°$), so each α_y ambiguity, together with the position of the particle plate crossing (known from the tracking systems), yields the Z projection l_z of the path length of the photon ambiguity. If the ambiguity has a reflection on the top side of the prism, l_z will be shorter.

The next step is to find the values of α_x, matching the X-coordinate of the hit. Since there are infinite solutions, it is advisable to apply the total internal reflection condition before calculating (Fig. 3.29). At a certain value of α_y, a maximum and

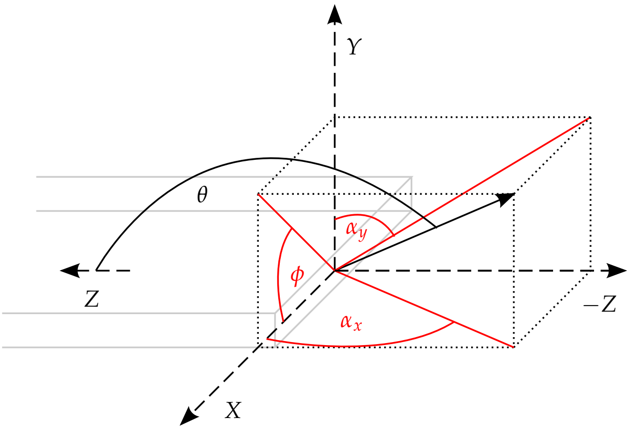

Figure 3.28: Schematic of the local coordinates system for the plate. The black non-dashed arrow represents the photon direction at the plate exit. The projections of this vector into the coordinate planes are indicated in red, together with the angles which need to be reconstructed in order to determine θ_C.

minimum α_x can be calculated, at which propagation through the radiator is still possible. If an α_x-value is outside these boundaries, the photon incident angles with the plate surfaces would be too steep and the condition for total internal reflection would not be fulfilled. Together with l_z, the remaining values of α_x can be calculated by artificially extending the readout plane and using the unfolded hit coordinates x_u. After this procedure was applied, a photon vector with initial polar angle θ and azimuth ϕ can be calculated (using Eq. 3.12 and 3.13) from the α_y ambiguity and each value of α_x.

Up to now only the spatial positions of the photon hits and the position of the particle/plate intersection has been used. The calculations are independent of any hypothesis about particle type, momentum, and direction. For the next step, the hypotheses are used to calculate two sets of Cherenkov angles. Each of the photon vectors is subtracted from the charged particle direction in order to yield a value for θ_C. In addition, Eq. 2.1 is used with the information of the particle type and momentum to calculate a range of θ_C-values, taking radiator dispersion into account. For the intersection of these two sets, the propagation time of each remaining ambiguity can be calculated as

$$t = \frac{l}{v} = \frac{l_z \cdot n_{\mathrm{Gr}}}{\cos(\theta) \cdot c_0}, \tag{3.19}$$

with the path length l, the photon speed $v = c_0/n_{\mathrm{Gr}}$, and the polar angle θ of the photon in the local plate coordinate system. The determined values are the mean values t_i of the Gaussians in Eq. 3.18. Figure 3.30d shows a histogram filled with the 13 values of t obtained with this method. A comparison to the simulated PDF in the same pixel (Fig. 3.30c) shows a very good general agreement of the peak

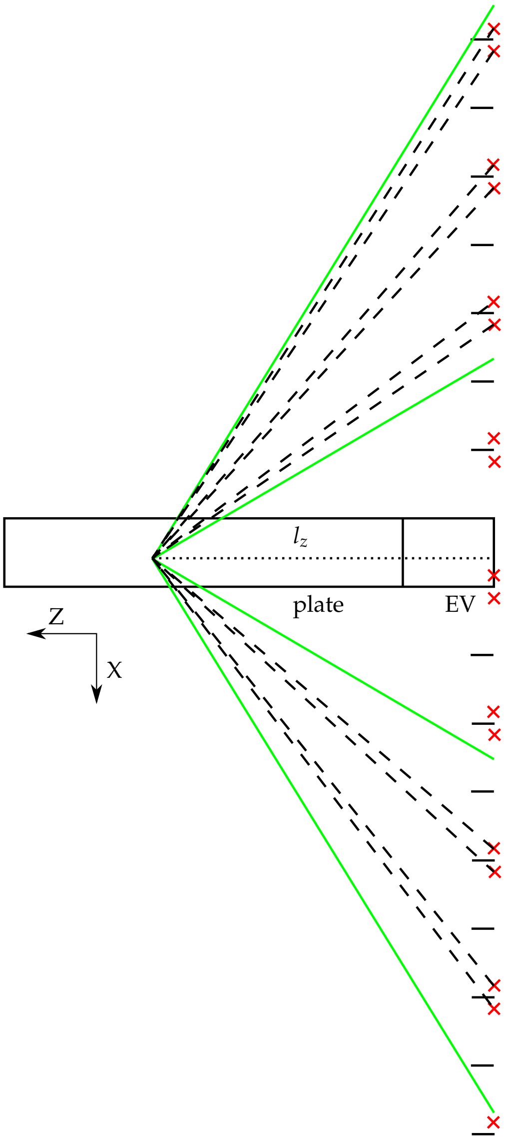

Figure 3.29: Plate and EV in the X-Z projection (not to scale). The red cross marks the X-position of the photon hit at the readout plane and at the unfolded readout plane. The green lines represent the threshold angle values of α_x between which the photons are totally internally reflected. This zone is determined analytically with the value of the α_y ambiguity. The only possible values for α_x (dashed lines) are within this zone.

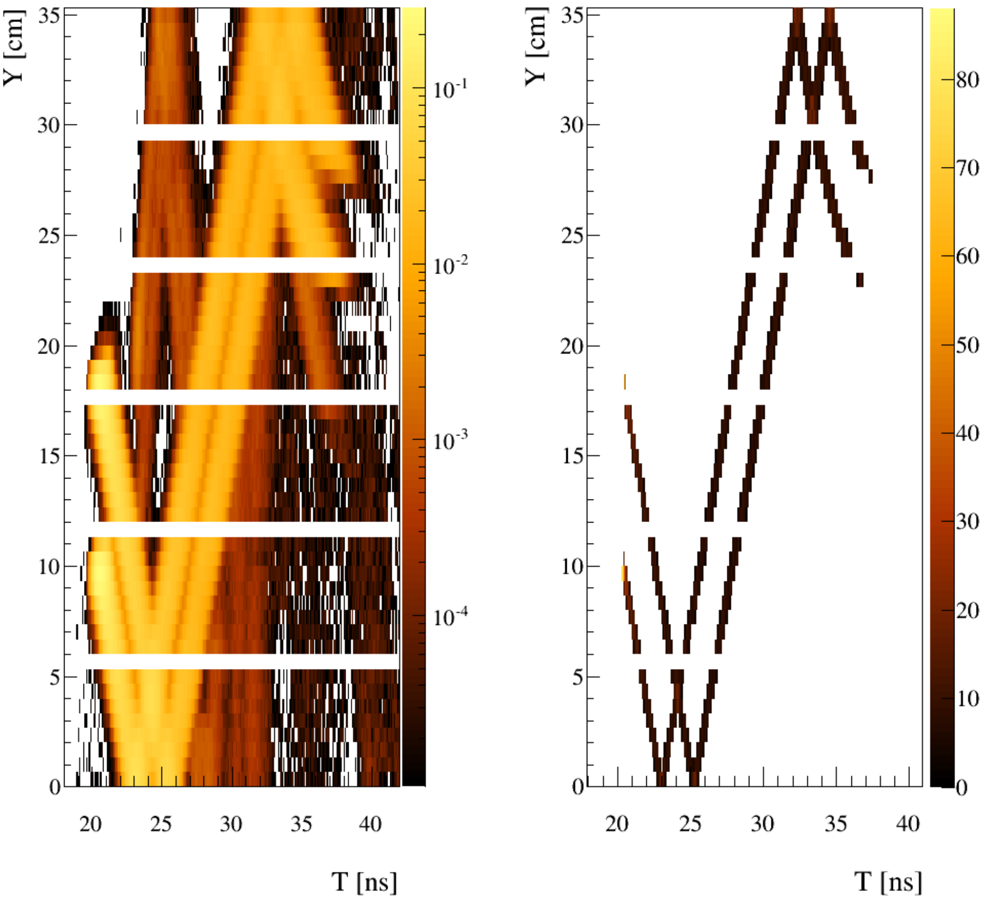

(a) Simulated hit pattern in Y-T (normalized color axis).

(b) Analytic time peak position in Y-T.

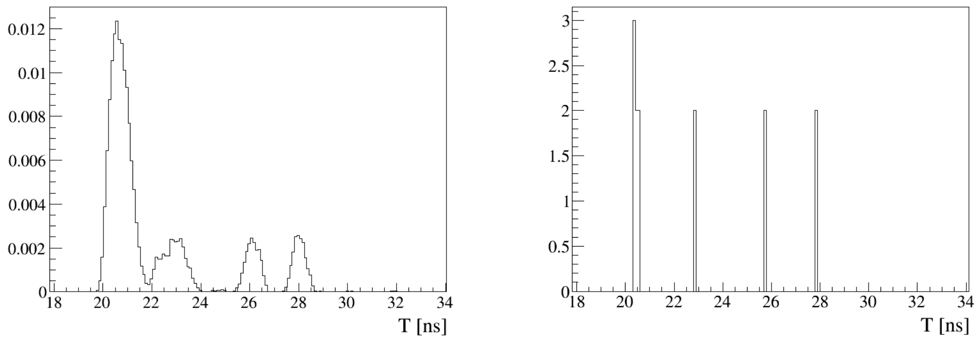

(c) Simulated and normalized pixel time distribution (X=0.3 cm, Y=9.6 cm).

(d) Analytic pixel time distribution (X=0.3 cm, Y=9.6 cm).

Figure 3.30: Comparison of simulated and calculated time peak position.

positions. The agreement is even more evident when the calculated peak positions of all pixels (Fig. 3.30b, Y-T projection) are compared to the corresponding simulation (Fig. 3.30a). In conclusion, it is possible to find the right position of the primary Cherenkov signal by this method. The darker parts of the pattern in Fig. 3.30a are created by additional reflections (as explained in Ch. 3.5) and are not discussed here.

Expression for the Width of the Time Peaks

All of the σ-values in the following section are derived in detail in Appendix B. The results of the derivations are presented here.

The width σ_t of the time peak is proportional to the peak position in t and determined from Eq. 3.19 by error propagation.

$$\begin{aligned}\sigma_t &= \sqrt{\left(\frac{\partial t}{\partial l_z}\sigma_{l_z}\right)^2 + \left(\frac{\partial t}{\partial \theta}\sigma_\theta\right)^2 + \left(\frac{\partial t}{\partial n_{\mathrm{Gr}}}\sigma_{n_{\mathrm{Gr}}}\right)^2} \\ &= t\sqrt{\left(\frac{\sigma_{l_z}}{l_z}\right)^2 + (\sigma_\theta \cdot \tan(\theta))^2 + \left(\frac{\sigma_{n_{\mathrm{Gr}}}}{n_{\mathrm{Gr}}}\right)^2} \end{aligned} \tag{3.20}$$

The polar angle θ of the photon depends on the projected angles α_x and α_y (Eq. 3.12) The uncertainty σ_θ is given by:

$$\begin{aligned}\sigma_\theta &= \sqrt{\left(\frac{\partial \theta}{\partial \alpha_x}\sigma_{\alpha_x}\right)^2 + \left(\frac{\partial \theta}{\partial \alpha_y}\sigma_{\alpha_y}\right)^2} \\ &= \frac{\cos^2(\theta)}{\tan(\theta)}\sqrt{\left(\frac{\sigma_{\alpha_x}}{\sin^2(\alpha_x)\tan(\alpha_x)}\right)^2 + \left(\frac{\sigma_{\alpha_y}}{\sin^2(\alpha_y)\tan(\alpha_y)}\right)^2} \end{aligned} \tag{3.21}$$

The projection α_x depends on the photon path (Eq. 3.10):

$$\begin{aligned}\sigma_{\alpha_x} &= \sqrt{\left(\frac{\partial \alpha_x}{\partial x}\sigma_x\right)^2 + \left(\frac{\partial \alpha_x}{\partial l_z}\sigma_{l_z}\right)^2} \\ &= \frac{1}{x^2 + l_z^2}\sqrt{(x \cdot \sigma_{l_z})^2 + (l_z \cdot \sigma_x)^2} \end{aligned} \tag{3.22}$$

Only the size of a pixel determines the uncertainty σ_x:

$$\sigma_x = 0.65\,\mathrm{cm}/\sqrt{12}, \tag{3.23}$$

The uncertainty σ_z of the photon path projection depends on the specific path within the prism. If the photon (ambiguity) is not reflected at the top side of the prism, σ_z equals zero, as the only other contribution could come from the particle track uncertainty, which is not accounted for in this simplified approach. If there is a top reflection, the projected path length l_z is shorter, depending on the pixel Y-coordinate. The uncertainty is in this case given by

$$\sigma_z = \sin(2\gamma) \cdot 0.65\,\mathrm{cm}/\sqrt{12}, \tag{3.24}$$

with γ being the opening angle of the prism.

For the determination of σ_{α_y}, another simplified approach is made. The largest value of α_y with a hit on the pixel and the smallest value of α_y are calculated. It is assumed that all intermediate values are equally likely. The extrema depend on the plate thickness a, the size of the step s between the bottom of prism and the bottom of plate, the pixel size p, and the prism depth d.

$$\sigma_{\alpha_y} = \left| \arctan\left(\frac{d}{y - p/2 - s - a}\right) - \arctan\left(\frac{d}{y + p/2 - s}\right) \right| / \sqrt{12} \tag{3.25}$$

The last term in Eq. 3.20 is the uncertainty of the refractive index resulting from dispersion. From Fig. 2.18 the relative error is taken to be

$$\sigma_n / n_{\mathrm{Gr}} = \frac{n_{\mathrm{Gr}}(300\,\mathrm{nm}) - n_{\mathrm{Gr}}(700\,\mathrm{nm})}{1.515\sqrt{12}} = 0.02, \tag{3.26}$$

with an average n_{Gr} of 1.515.

The results of the width calculation can be seen in Fig. 3.31. Figures 3.31a and 3.31c display the simulated cases and Fig. 3.31b and 3.31d the calculations, as before.

Expression for the Number of Entries of the Time Peaks

The peaks need the right normalizations, i.e. number of entries, for the correct relative height as well as for the global PDF normalization. The main contribution is the fraction of the ϕ_c ring that falls into the observed pixel. Cherenkov photons are created isotropically in azimuth, and each ϕ_c value belongs to a specific photon ambiguity (if the photon was detected). The second contribution is the number of created photons given by the path length l of the particle track in the radiator and the Cherenkov angle of the photon (see Eq. 2.2). According to [58], the number n_i in Eq. 3.18 can be expressed as

$$n_i = N_0 l \sin^2\theta_C \frac{\Delta\phi_C}{2\pi}, \tag{3.27}$$

with N_0 being a constant of proportionality. N_0 has a value of 2.5 and was chosen manually to match the simulated and the calculated patterns. The results of this last

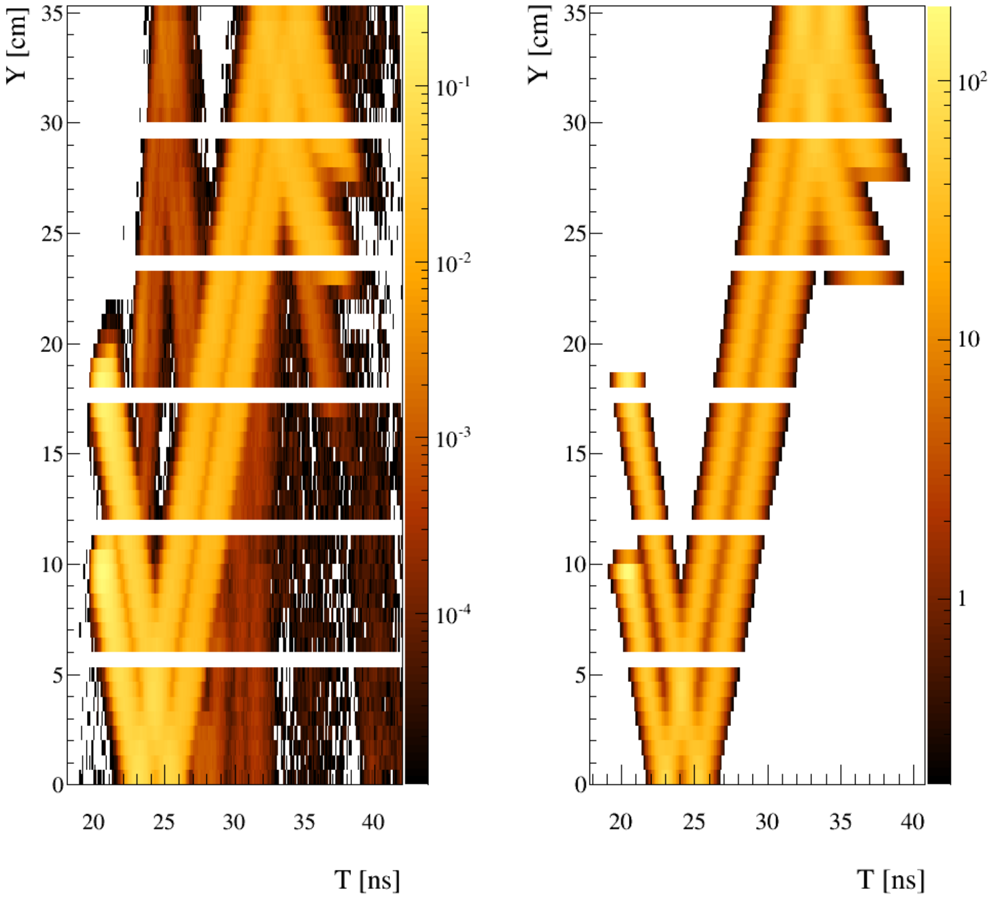

(a) Simulated hit pattern in Y-T.

(b) Analytic time peak position and widths in Y-T.

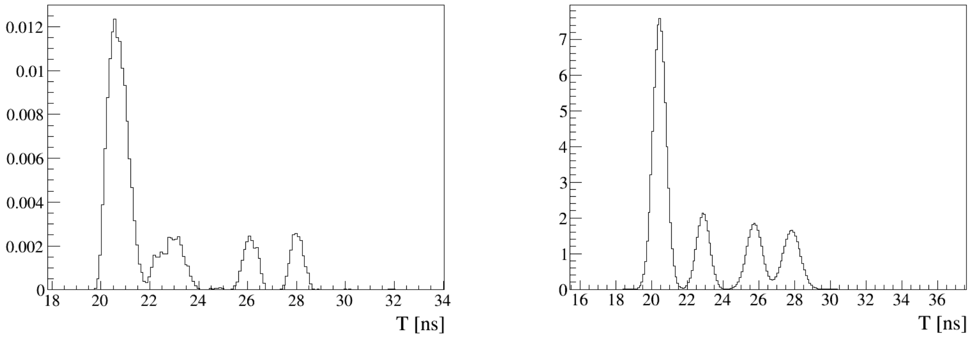

(c) Simulated pixel time distribution (X=0.3 cm, Y=9.6 cm).

(d) Analytic pixel time positions and widths (X=0.3 cm, Y=9.6 cm).

Figure 3.31: Comparison of simulated and calculated time peak width.

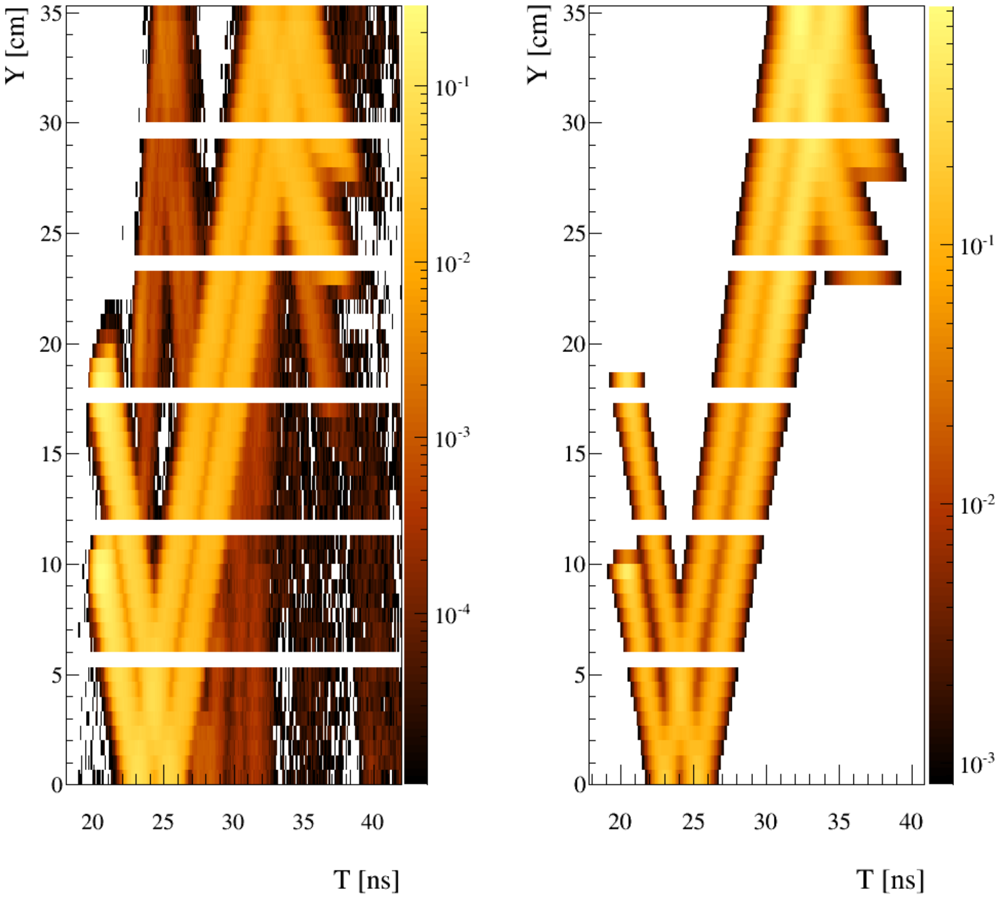

(a) Simulated hit pattern in Y-T.

(b) Analytic time peak positions, widths, and normalizations in Y-T.

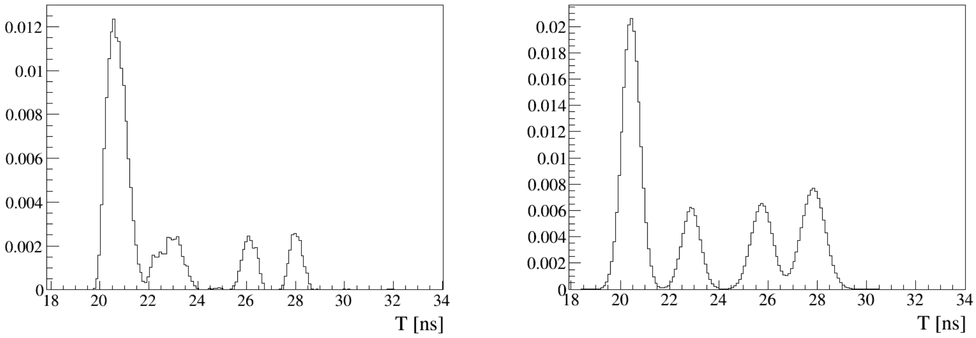

(c) Simulated pixel time distribution (X=0.3 cm, Y=9.6 cm).

(d) Analytic pixel time positions, widths, and normalizations (X=0.3 cm, Y=9.6 cm).

Figure 3.32: Comparison of simulated and calculated time peak normalizations.

step in the PDF calculation can be seen in Fig. 3.32.

Conclusion

The derivation shown here is only the first step and shows that it is possible to find an analytical model to describe the observed distribution and to create the PDFs. As the relative height of the peaks are apparently not well described (as can be seen in Fig. 3.32b and 3.32d), a better equation for n_i has to be found. Since the study of the analytic PDFs was intended to be a proof of principle only, the photon propagation probability, which decreases with the length of the photon path and the number of internal reflections, was not considered. Another ignored influence on the detection probability is the wavelength of the photon. The width of the peaks is influenced by the uncertainty of the z-component of the photon creation point, which can be obtained from the inclination of the charged particle track to the plate.

The inclusion of all this contributions is expected to improve the equations for better precision. Other approaches could aim to simplify the equations to make computation easier or faster. All of this has to be tested in detail with studies of simulations and PID performance tests, but that is beyond the scope of this work. It is important to investigate which parts of the calculations can be performed at what stage in the later experiments, as the complete calculation of the PDFs need to be fast enough for an online reconstruction at PANDA DIRC rates. The cut on photons, not fulfilling the total internal reflection condition, can, for example, already be applied (to a certain extend) as soon as the particle track direction in the plate is known and before the Cherenkov photons are measured.

4. Test of Prototypes with Particle Beams

4.1. Prototype Components

During the course of this thesis, two beam campaigns (2012 at CERN and 2014 at GSI) were conducted to test the performance of a PANDA Barrel DIRC prototype with a plate geometry. Results of both beam times were analyzed for this thesis. The different modules of the two prototypes and the different methods used in these beam times will be discussed during the explanation of the experimental setup. Four days of measurements at CERN in 2012 served as entry point to a series of plate-based prototypes and resulted in qualitative concurrence with simulated hit patterns. The second beam campaign in 2014 at GSI was dedicated to validating the performance of the plate design regarding resolution and photon yield.

Thickness	17.11 mm
Width	174.75 mm
Length	1224.94 mm
Material	Spectrosil 2000
Manufacturer	InSync, Inc.
Finishing	pitch polishing

Table 4.1: Manufacturing properties of the prototype plates.

Two identical synthetic fused silica plates had been fabricated as Cherenkov radiators and one was tested in the 2012 and 2014 beam campaigns. Table 4.1 shows details of the plate properties; more technical informations from the manufacturer data sheet can be found in Appendix A.

The prism used in 2012 has an opening angle of 30°(see Fig. 2.14). In 2014 a different prism was used with an opening angle of 45°. Both prisms are made of Corning Fused Silica 7980 [61] from Advanced Glass Industries [62]. The width of the prisms is 17 cm, the depth is 30 cm, and the front face height is 3 cm for the 30° prism and 5 cm for the 45° prism. The height of the back planes differs due to the different opening angles.

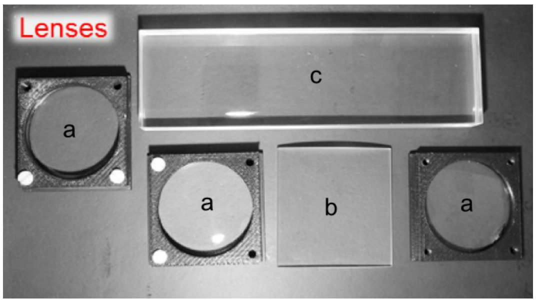

Figure 4.1: Lenses used for the prototype tests. a: Spherical 1-component lens; b: Cylindrical 1-component lens; c: Cylindrical 2-component lens (NLak33 lens) [44].

Some of the tests were performed with cylindrical lenses (Fig. 4.1). A two-component lens with a transition from optically less dense fused silica to optically more dense NLak33 (top lens in Fig. 4.1 and simulated version in Fig. 3.17) was used in the prototype tests. Three identical pieces of a fused silica lens were used together (only in 2012). The advantage of the NLak33/fused silica lens system over the pure fused silica lenses is that it does not require an air gap between the lens and the prism. This eliminates a big contribution to photon loss during photon propagation. The NLak33 lens has an anti-reflective coating for wavelengths below 460 nm and a focal length of 30 cm with a curved surface radius of 7.35 cm. The length is 17 cm, the thickness 1.43 cm, and the width 5 cm.

At the opposite end of the plate, a plane mirror was placed with a very small air gap between the plate and the mirror. Photons with appropriate incident angles were totally internally reflected at the fused silica/air interface, while photons with steeper incident angles were reflected by the mirror. The optical grease EJ-550 from Eljen [63] was used to couple the plate-to-lens, lens-to-prism, and prism-to-sensor interfaces.

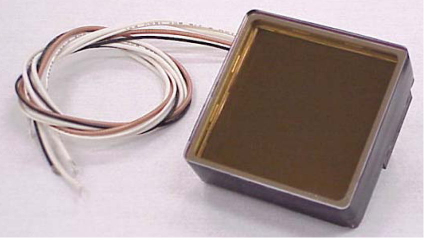

Figure 4.2: PHOTONIS Planacon XP85012 [64].

Planacon XP85012/A1 micro-channel plate photomultiplier tubes (MCP-PMT) from PHOTONIS [64] were used in both beam times as photon sensors. Figure 4.2 shows a sensor similar to the ones used for the tests. The tube has a square $59 \times 59\,\text{mm}^2$ housing and an active area of $53 \times 53\,\text{mm}^2$, with $8{\times}8$ pixels (6.5 mm pixel size). The bialkali photocathode has single photon sensitivity and a dark noise rate of typically 1 kHz/cm^2. The transit time spread is in the order of 30 ps [65]. The tubes were operated at a gain of 10^6. Matrices from ABS plastic were designed and produced to hold the tubes in a fixed position during the tests. The optimal positions for the tubes were determined via simulation before the tests.

The whole setup was mounted on a supporting structure with rails and a rotating table to translate (x, z direction) and rotate (polar angle θ) the prototype relative to the beam.

4.2. Supplemental Devices

Auxiliary counters were added to the setup for beam control and monitoring. Two scintillator paddles with 40 mm diameter of active area each were placed in front and behind the prototype and read out with PMTs. The upstream counter served in some of the tests in 2014 as event trigger. The coincidence of the two trigger signals was recorded as well and used for event triggering during the 2012 tests.

Two time-of-flight stations (TOF) were installed as the first and the last element along the beamline. Each station consists of an acrylic glass Cherenkov radiator, coupled with Bicron BC-630 optical grease to a PHOTONIS Planacon XP85012-D MCP-PMT. The radiator block has an area of $59 \times 59\,\mathrm{cm}^2$, fitting the dimensions of the MCP-PMT. The purpose of the TOF stations was to provide charged particle tagging and an event trigger (upstream TOF) for some of the runs in 2014. More on the TOF stations can be found in Ref. [45].

For time and occupancy calibration, a pulsed 405 nm PiLas laser diode [66] was routed with optical fibers into the covered and light-tight prototype box.

The data acquisition (DAQ) for the prototypes as well as for the auxiliary counters was performed by Trigger and Readout Boards (TRB) which were developed for the HADES experiment and modified and adjusted to the needs of other FAIR-related experiments [67]. In 2012 the second generation (TRBv2) of the versatile readout module was used, in 2014 the third and so far newest generation (TRBv3 [68]) was employed. The raw data stream is saved with 32-bit hexadecimal data words in binary files. For each event all hit entries are saved with TDC identifier, channel number, and leading and trailing edge time. For the TRBv2 data, a converter was developed by the HADES group at GSI. The conversion for the TRBv3 data was written at Mainz University. Since there are some significant differences between the TRB generations, the further description of the DAQ will follow when the beam times of 2012 and 2014 are described separately.

4.3. 2012 Test Beam Campaign

The prototype test campaign of 2012 took place in the T9 beam line area at the CERN Proton Synchrotron (PS) [69]. Secondary hadron enriched beams with momenta ranging from 1.5 to 10 GeV/c were used with typical intensities of 10^4 per 400 ms spill length. Focusing and beam momentum were adjustable by the user without the need to enter the experimental zone. The highest intensities were possible with beam momenta of 10 GeV/c, while at lower momenta the intensities decreased by several orders of magnitude. The focus of the beam was for most of the runs set to parallel mode with a beam spot size of about 20 mm rms.

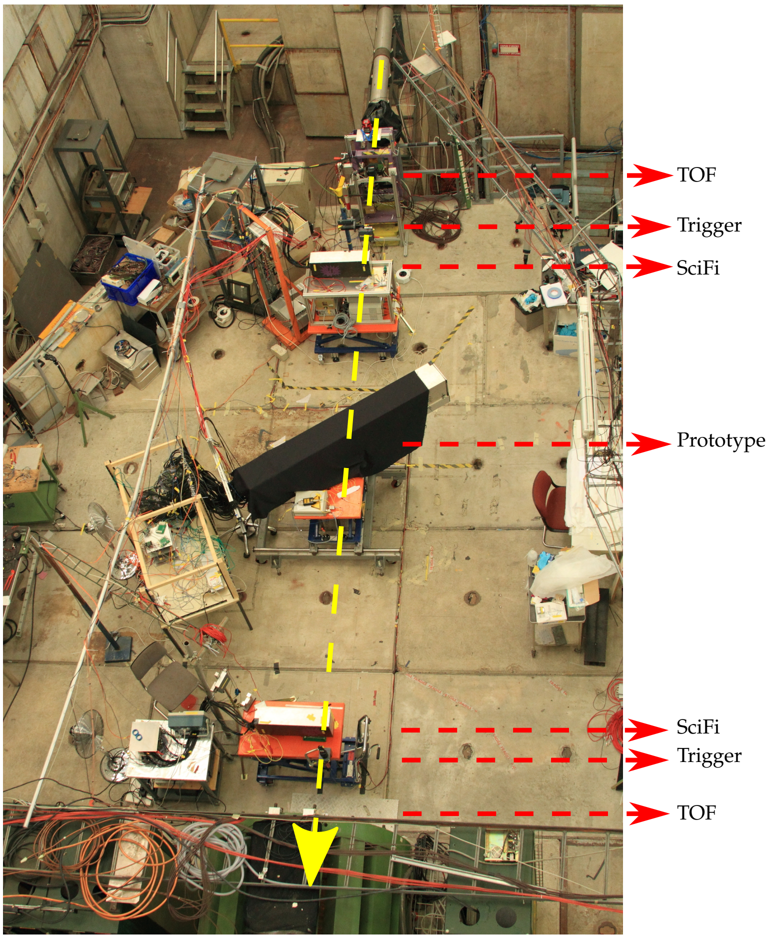

Figure 4.3: Top view of the experimental area. The particle beam (yellow line) passes the following components (from the top to the bottom): Beampipe, MCP-TOF station, trigger counter, SciFi station, DIRC prototype, SciFi station, trigger counter, and second MCP-TOF station.

Figure 4.3 shows the view from top into the experimental zone with all installed counters. Approximately 8 m of space was available for the counters in the area. A schematic view of the setup can be seen in Fig. 4.4, the distances of the components are found in Table. 4.2.

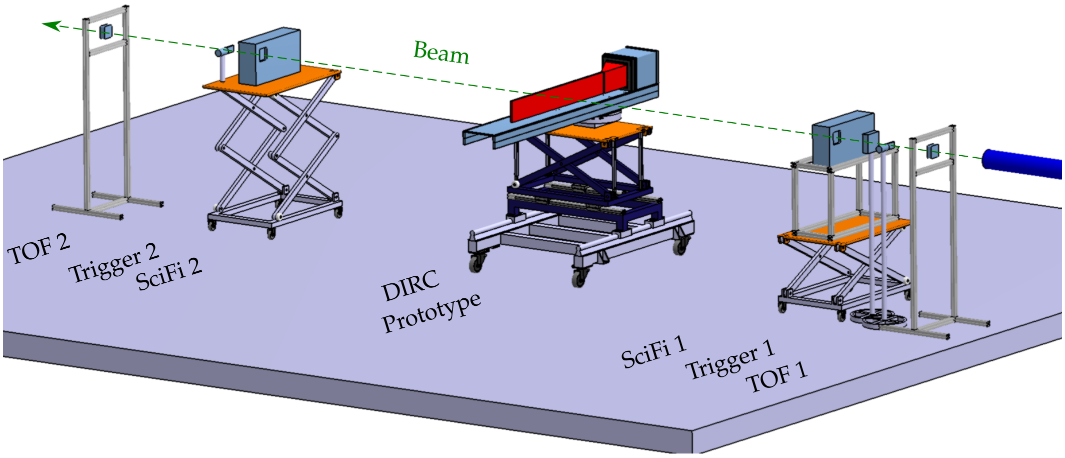

Figure 4.4: Technical drawing of the 2012 prototype arrangement.

	TOF1	Trigger1	SciFi1	DIRC	SciFi2	Trigger2	TOF2
[cm]	50	142.3	193.1	468	694.3	725.3	808

Table 4.2: Distances of the components measured in cm from the beam pipe exit.

The MCP-PMTs were arranged in a 3×3 matrix with horizontal gaps of 9 mm and vertical gaps of 2 mm. The gaps and the limited number of sensors resulted in a total coverage of the imaging plane of 64.5%. This number includes the ratio of the active sensor area to the total sensor area. Figure 4.5 shows a photo of the prism and the sensor plane with optical grease applied before assembly.

Readout Electronics

The DAQ board (TRBv2) uses an ETRAX FS CPU and four time-to-digital converter chips (CERN HPTDC [70]) with 32 channels and 98 ps binning (high resolution mode) or 8 channels and 24 ps binning (very high resolution mode). The board has 100 Mbit/s Ethernet connectivity, a 2 Gbit/s optical link and programmable logic based on field-programmable gate arrays (FPGA). A 128-channel time-of-flight (TOF) front-end discriminator module was used as addOn board to convert the detector pulses into timing signals. The TOF addOn includes amplifiers (BGA2712 [71]) as

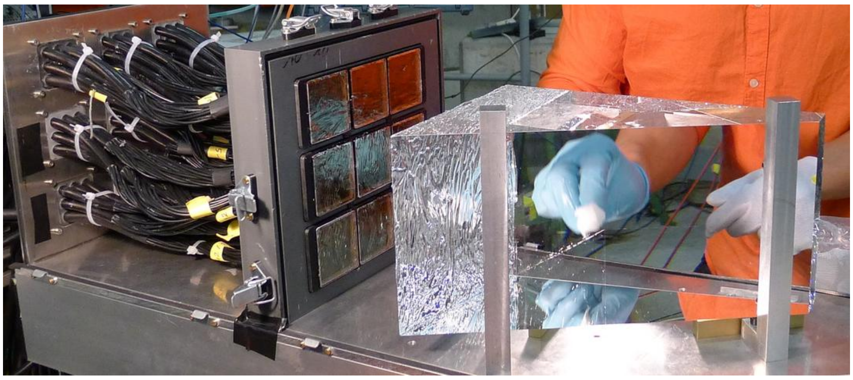

Figure 4.5: Prism with applied grease, sensor plane and part of the readout box.

well as discriminators (NINO-ASIC [72]) and is optimized for the use with MCP-PMTs.

An additional TRB was used as Central Trigger System (CTS) to collect the external trigger signal (either the trigger counter or the PiLas laser) and to distribute it as clock to all other boards. Another board was responsible for setting registers, threshold levels, and other parameters of the DAQ.

In total, seven TRB and TOF addOns were used for the sensor readout, resulting in 896 channels (576 channels for the DIRC MCP-PMTs). On each board, four channels (one per TDC) were not usable for data signal input, as they were reserved for the reference clock, provided by the CTS. The time signal from the trigger counter was distributed to all readout boards so that a time synchronization of channels from different TRBs was possible. Relative timing between channels on the same board did not require the trigger signal.

Data Analysis

In total, 218×10^6 triggers were recorded during the CERN beam campaign in 2012, of which 35×10^6 triggers were taken with the prototype plate in the beam. Typically 1 - 1.5×10^6 triggers were used for each run. Various parameter scans were performed, including the track polar angle, particle crossing position on the plate area, particle momentum, and track azimuth angle. The runs were taken with several types of focusing (no lens, air-gap lens, NLak33 lens). Figure 4.6a shows a simulation of the prototype geometry and particles crossing the plate with an angle that translates to 54° polar track angle in the PANDA simulation and a momentum of $3\,\mathrm{GeV}/c$. Figure 4.6b shows the simulated hit pattern for 6 000 tracks in this selected configuration.

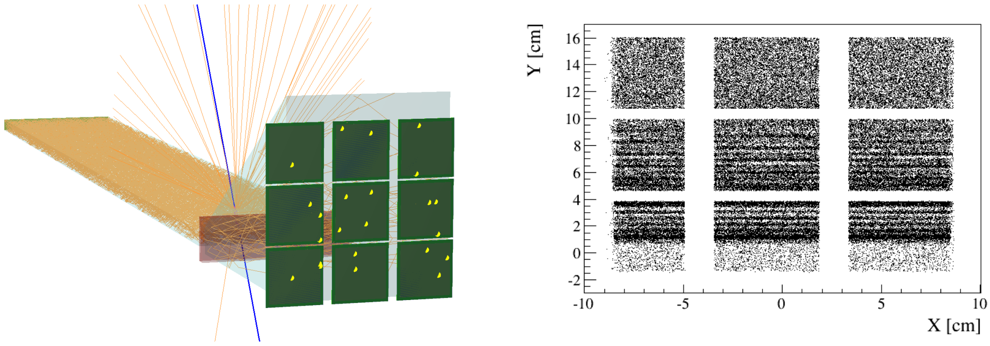

(a) A single pion (blue) event in the 2012 prototype geometry. Hits on the readout plane are marked in yellow.

(b) Scatter plot of true hit locations after 6 000 simulated tracks.

Figure 4.6: Simulation of pions with $p = 3\,\mathrm{GeV}/c$ and $\theta = 54°$.

Time Calibration

The reconstruction methods of the wide plate depend strongly on the correct time synchronization between boards and channels, and a time resolution in the order of 100 ps for the whole DAQ chain. Under realistic conditions, all data channels had unknown time offsets of up to several nanoseconds. The most promising way to correct these offsets within each sensor was by using charge sharing information. Charge sharing occurs in an MCP-PMT when the electron cloud coming out of the MCP spreads to neighboring anode pads, causing additional sensor hits. A higher probability of hits in neighboring channels in the same event is the consequence. The differences of coincidental leading edge hit times of neighboring pixels are plotted in Fig. 4.7a. The position of the peak in the time distribution has a value equal to the time offset between these two pixels.

Subsequently, the sensor time offsets were eliminated by fitting time peaks to the simulation. Figure 4.7b shows the time offsets of all data channels that were found with this method. Some of the channels have very extreme offset values. This was mostly the case for dead channels with a few hits only. These channels were not used for the data analysis anyway.

Time-of-Flight Information

The TOF counters help to tag charged particles with momenta up to $5\,\mathrm{GeV}/c$. In addition, it is possible to obtain information about the beam composition. However, most of the runs were taken with $10\,\mathrm{GeV}/c$, since sufficient beam intensities were available only at higher momenta. Thus, particle species could not be separated

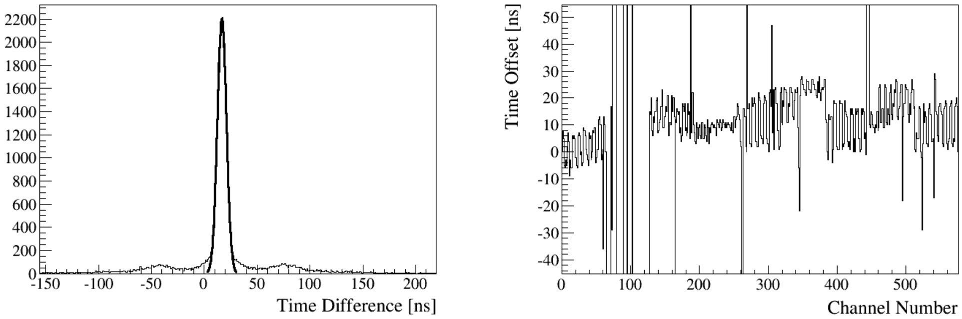

(a) Hit time difference of specific neighbouring pixels.

(b) Fitted time offset for each data channel.

Figure 4.7: Hit pattern after time correction.

from each other with the TOF or the DIRC for a majority of the data. Table. 4.3 gives an overview of the number of runs taken at different momenta and the typical statistics.

Momentum [GeV/c]	**Runs**	**Triggers per run**
10	51	700k - 1M
7	1	350k
6	1	370k
5	1	380k
4	1	280k
3.5	1	210k
3	1	170k
2.5	1	17k
1.5	1	184k

Table 4.3: Beam momenta with number of runs and recorded triggers per run.

Figure 4.8 shows the PID results determined by subtracting the MCPout times of the two TOF counters. Since the counters were read out with the same DAQ board, a time correction between the two MCPout signals was not necessary. At the depicted 10 GeV/c run (Fig. 4.8a), a single peak is visible without any distinguishable structure. At lower momenta (Fig. 4.8b), several time peaks become visible and can be associated with pions and protons. The hit time resolutions for the TOF can be improved by using the trailing edge information of the data. This allows to define the time over discriminator threshold, a value correlated with the pulse height. It can be used to partly correct the time-walk of the leading edge by several tens of picoseconds. The time-walk correction of the TOF system was not effective for the DIRC analysis since the uncorrected time resolutions were an order of magnitude worse than the correction. Results together with a comprehensive analysis of the 2012 TOF data can be found in Ref. [45].

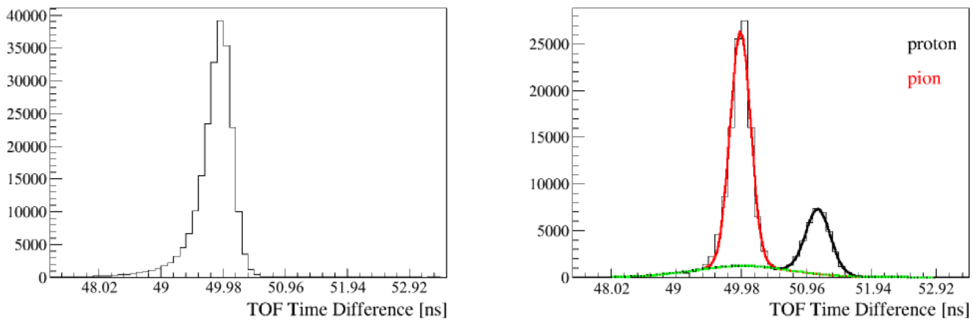

(a) Data taken with $p = 10\,\mathrm{GeV}/c$. The beam momentum is too high for a thorough TOF analysis.

(b) Data taken with $p = 3\,\mathrm{GeV}/c$. The red curve is a fit to the distribution tagged as pions, the black curve is a fit to the distribution tagged as protons. The green curve represents the background of the fit.

Figure 4.8: Time differences of the sum signals of TOF1 and TOF2 for two different beam momenta.

The results in Fig. 4.8b show that the beam was mainly composed of pions and protons, whereas kaons could not be identified over the background spectrum. According to Eq. 2.1, the Cherenkov angle difference of pions and protons at $10\,\mathrm{GeV}/c$ is 4 mrad, which corresponds to a pion/kaon separation at $5\,\mathrm{GeV}/c$. This is beyond the momentum acceptance of the DIRC. Table 4.4 shows the Cherenkov angle differences at the measured momenta and the momentum, at which the same difference between pions and kaons would occur. The particle tags are used to evaluate the performance of the DIRC reconstruction algorithm.

Momentum [GeV/c]	10	7	6	5	4	3.5	3	2.5	1.5
$\Delta\theta_C(\pi - p)$ [mrad]	4	8	11	16	25	33	44	64	180
π/K sep. at [GeV/c]	5.1	3.6	3.1	2.5	2.0	1.8	1.5	1.3	0.8

Table 4.4: θ_C difference of π and p at the measured beam momenta. The third row contains the π/K momentum at which the same θ_C difference would occur according to Eq. 2.1.

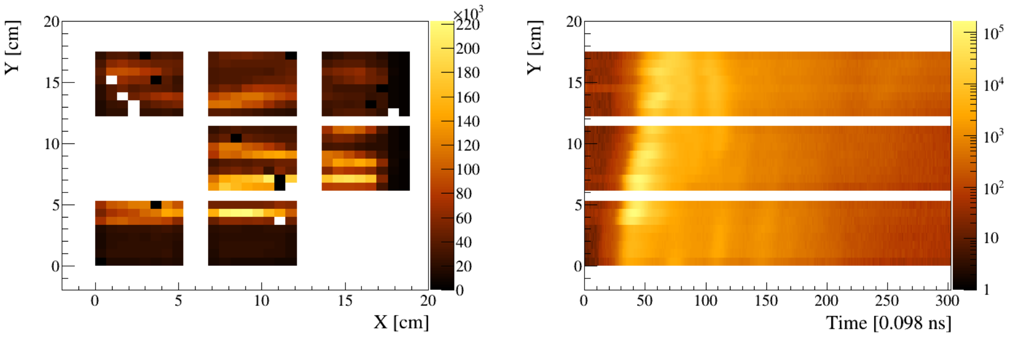

(a) *X*-*Y* occupancy of beam data.

(b) *Y*-*T* occupancy of beam data.

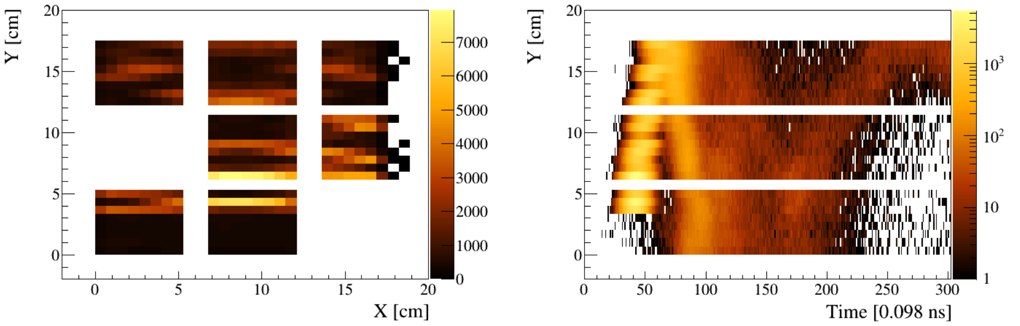

(c) *X*-*Y* occupancy of simulation.

(d) *Y*-*T* occupancy of simulation.

Figure 4.9: Occupancy plots of data (upper plots) and simulation (lower plots). The brightness shows the number of hits in the pixels. Coupled with the NLak33 lens, momentum at 10 GeV/c, polar track angle at 124°.

Occupancy and Photon Yield

The 10 GeV/c runs were of limited use to draw any performance conclusions but they were useful for sharpening the tools for data analysis as well as for the comparison of data and simulation. Figure 4.9 shows the occupancy map for a data run and the corresponding simulation. The NLak33 lens was used in the setup. For the color axes in the Y-T projections, a logarithmic scale was used (Fig. 4.9b, 4.9d). The data channels were time-wise corrected and aligned, and a time cut of 50 ns was applied. Two of the sensors were cut out due to low efficiency. This was also applied in the simulation. It is worth mentioning that the main signal is similar in both, data and simulation. However, regarding the data, the noise level is higher and the time resolution is worse. It was found that the readout electronics were not able to deliver the sub-100 ps time resolution as expected, but resolution values of several hundreds of picoseconds. A detailed study of the underlying reasons was done after the beam time. The results can be found in [73].

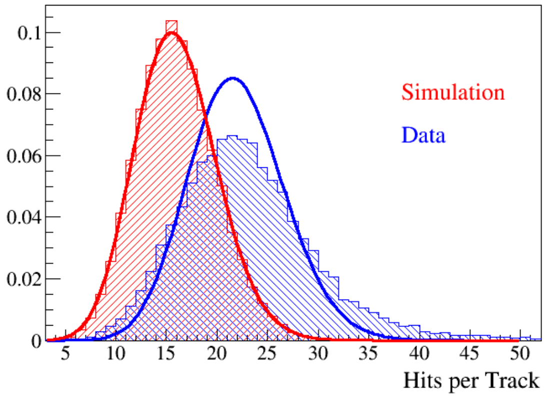

Figure 4.10: Photon yield comparison of data and simulation (pions with $p = 10\,\mathrm{GeV}/c$ and $\theta = 124°$). The solid lines represent fitted single Poissonian distributions.

Figure 4.10 shows the distribution of the number of hits per track for the same set of data and of the corresponding pion simulation. The mean number of hits per track of the data is apparently not well described by the simulation. Additionally, the expected Poissonian shape of the distribution is not visible in the data. The reason for this is unknown, especially since a similar mismatch between data and simulation was not observed during the analysis of the data with the narrow bar geometry [44]. A possible cause could be the multiple coincidental tracks crossing the plate in each event. The probability of this to happen is larger with the plate than with the bar, due to the larger area of material the smeared particle beam can hit. However, no simulation with multiple random particles was able to reproduce the observed photon yield distribution. For the reconstruction of high momentum particles, an incorrect mean number of hits per track is not a serious problem in terms of calculating the right likelihoods. The Poissonian term in Eq. 3.1 vanishes when taking the log likelihood difference for protons and pions at higher momenta, since the expected photon yield is approximately the same for all particle types. If the hits are indeed generated by multiple tracks, fake hits are introduced which add to the noise background and worsen the reconstruction performance.

Reconstruction and Conclusion

A reconstruction was performed for the data run with a beam momentum of $3\,\mathrm{GeV}/c$ and the likelihood ratio distribution was compared with the simulation. No focusing optics were applied. According to the TOF result in Fig. 4.8b, 68% of all the particles were tagged as pions, the rest mostly as protons. For the likelihood analysis, the same number of pion-tagged and proton-tagged particles were used. A time resolution of 500 ps for the readout was used in the simulation, in order to be consistent with the situation of the experiment. The results of the likelihood ratio test of the simulation and the data can be seen in Fig. 4.11. The red distribution represents the particles that were tagged as pions with the TOF, while the black distribution represents the protons.

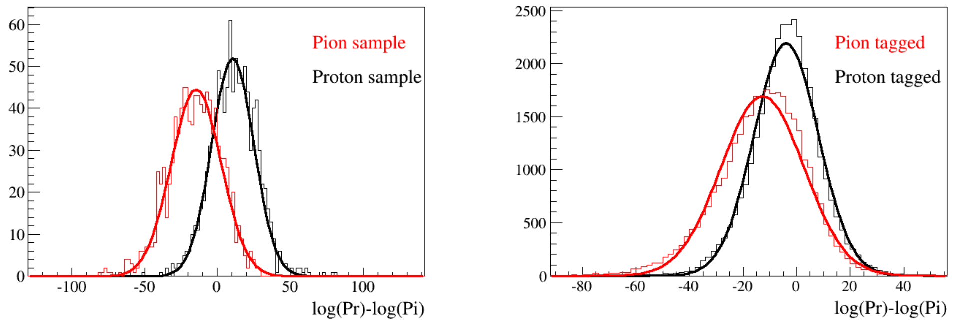

(a) Likelihood ratio test with 1000 simulated particles for each species. The time resolution is set to 500 ps.

(b) Likelihood ratio test with beam data. The same number (33 600) of pions and protons were used.

Figure 4.11: Likelihood ratio test of protons and pions with 3 GeV/*c* of beam momentum and 54° of track polar angle.

Even in the simulation (Fig. 4.11a), a successful pion/proton separation with sufficient separation power is not possible. The reason for this is the poor time resolution of the DAQ. The beam momenta were above the momentum acceptance of the DIRC for the majority of the other data during this campaign. A small separation of 0.6 s.d between pions and protons is visible (1.6 s.d in the simulation) after the likelihood ratio test in the beam data (Fig. 4.11b). The mean value of the likelihood ratio of the kaon tagged particles is, however, with a value of -3.9 smaller than zero, which means that more than half of these particles yield higher likelihood values with a pion hypothesis than with a proton hypothesis. As a conclusion of the discussion of these results, it is not possible to validate the reconstruction methods with the data taken in 2012. The hit patterns of simulation and data are similar but the poor time resolution permits only a small separation between the particle species, which cannot be described comprehensively by the simulation, due to unknown effects influencing the time resolution and the photon yields. The time resolution problems were partly solved after this beam time, while the beam momenta at the subsequent beam time at GSI were much lower and thus more suitable for this prototype.

4.4. 2014 Test Beam Campaign

The beam time at GSI in 2014 was split into three parts. Four days in April were used for tests of the new readout electronics without the DIRC prototype. About 13M triggers were recorded with the plate prototype on seven days in July. In July and August 21M triggers were taken with the plate and 20M triggers with the radiator bar. The beam was operated with a fixed momentum of 1.7 GeV/c and was almost entirely composed of pions[1]. An analysis of the separation power of the pions and any particle species was therefore impossible with the beam data. A LH ratio analysis can nevertheless be performed, comparing the data with pion and kaon hypotheses. The pions were, in addition, used to tune the simulation properly, as will be elaborated in a subsequent chapter.

Pictures of the beam cave can be seen in Fig. 4.12. After approximately 3 m in air, the particle beam enters a solenoid. The space in front of the magnet was used for the first TOF station. Behind the magnet, the other beam counters and the prototype were located on a total length of 8 m (Fig. 4.12a). An upstream view of the backside of the magnet and the prototype is shown in Fig. 4.12b.

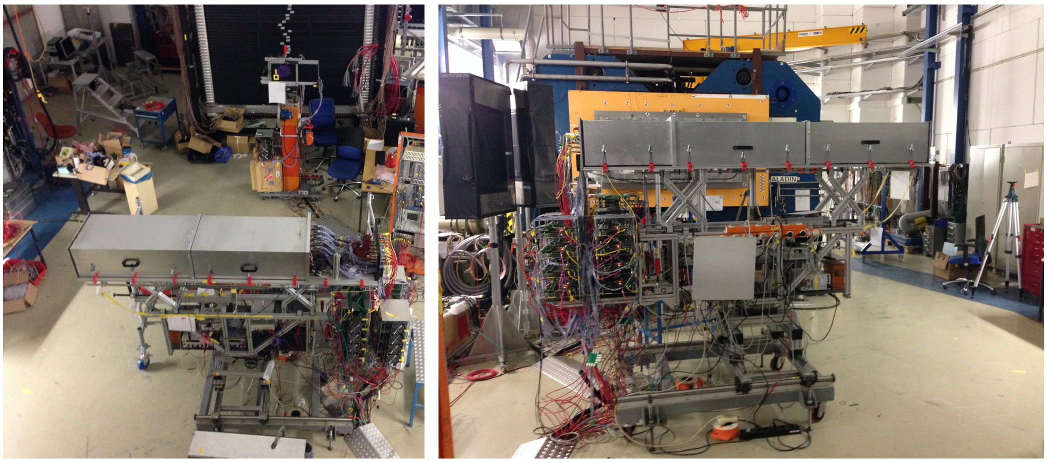
(a) Downstream view. ***(b)*** Upstream view.

Figure 4.12: Pictures of the DIRC prototype in the GSI beam cave.

The first component behind the magnet was the first trigger counter, flanked by two veto counters and followed by the first (dysfunctional) scintillating fiber tracker. The next component was the DIRC prototype. At the end of the available space, the second scintillating fiber tracker, the TOF, and the second trigger were located. Table 4.5 shows the distances from the first configuration in July. The scintillating fiber trackers were not working and thus removed before the August tests. For the majority of runs in August, the second trigger counter was moved between the prototype and the second TOF station.

One beam spill had a duration of approximately 2 s and was repeated typically after 3 s. The typical intensity was about 2k - 4k particles per spill but showed variations

---

[1] This was evident from the TOF analysis.

TOF1	Veto	Trigger1	SciFi1	DIRC	SciFi2	TOF2	TOF3	Trigger2	unit
0	648	657	745	943	1337	1344	1352	1446	cm

Table 4.5: Distances of the components in cm measured relative to the upstream TOF station.

over three orders of magnitude, depending on the settings of the accelerator dipoles. It is not clear how the focus of the beam was set up. For a detailed data analysis, the coincidences of the two trigger counters were used to narrow down the beam profile.

Readout Electronics

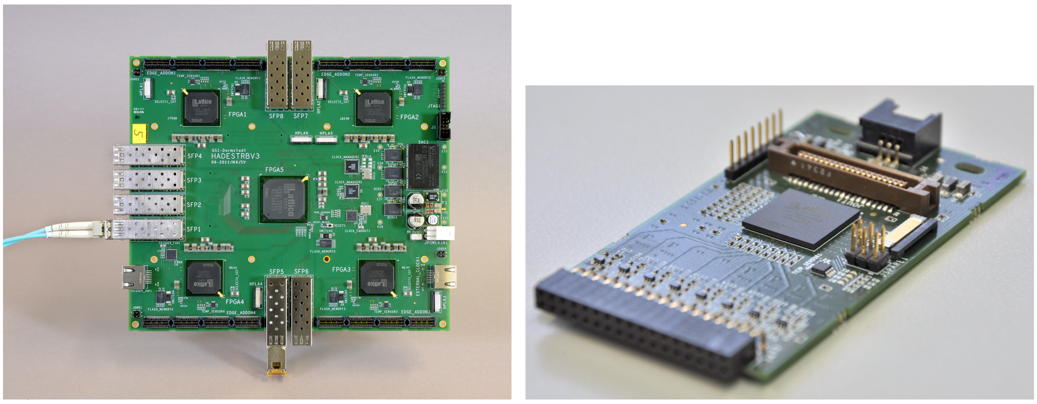

(a) DAQ board (TRBv3).

(b) Frontend card (PADIWA).

Figure 4.13: Main components of the readout electronics [68].

The data acquisition was performed with TRBv3 boards (Fig. 4.13a) [68], a complete new version of the trigger readout boards developed by the HADES collaboration. Each board has 256 data channels and a high precision time resolution better than 14 ps [74]. The time-to-digital converters (TDC) are realized in four FPGA modules per board, while a fifth FPGA provides trigger functionality, Gigabit Ethernet connectivity, and slow control [68]. By combining two of the data channels, the leading edge and the width of a time signal could be measured, reducing the number of input channels by a factor of two. Another factor of two in channel reduction was caused by firmware restrictions so in total 64 input channels were available on each board.

As front-end electronics, PADIWA[2] boards (Fig. 4.13b) were directly connected to the PMTs, four boards per tube. Based on FPGAs, a PADIWA contains leading edge

---

[2] The PADIWA is named after PANDA, DIRC, WASA

discriminators for 16 analog input signals, a wide-band amplifier, and RC low-pass filters [68].

Prototype Components

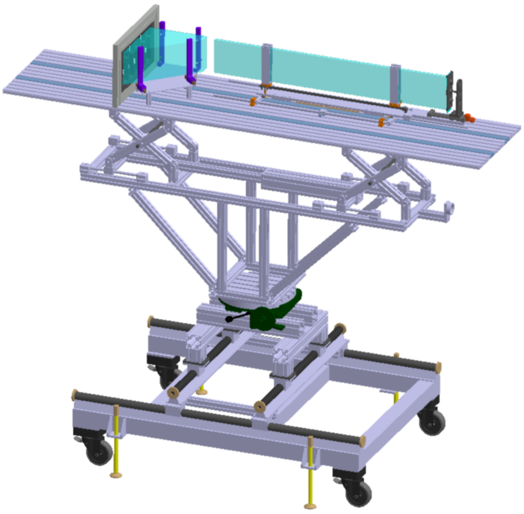

Figure 4.14: Schematic drawing of the prototype stage, the radiator, and the prism.

Figure 4.14 shows the main components of the prototype excluding the readout sensors and electronics. A new prism with an opening angle of 45° was used as expansion volume, while the radiator plate and the lens have been the same ones as in 2012. Since the back plane of the prism was bigger than of that used in 2012, more sensors were used for the readout. Figure 4.15a shows the fifteen MCP-PMTs embedded in a plastic matrix, after the optical grease was applied and before the prism was coupled. The optimal sensor arrangement was simulated before the beam campaign and yields a 65% coverage of the sensor plane. The fully mounted prism can be seen in Fig. 4.15b together with the two component NLak33 lens and the prototype plate. The PiLas signal (yellow fiber) was initially coupled into the big prism with a small prism but was later attached directly to the big prism as a measure to get a more uniform illumination on the sensor plane.

The optical components were placed on a height adjustable and rotating table, which was, during the experiment, lifted up in order to move the plate into the beam at a height of 2 m. The table resided on a frame which itself contained a turntable, with the purpose to perform angular scans with different beam polar angles. Rails were used for measurements at various positions alongside the length of the plate. By

(a) Senors embedded in plastic matrix with optical grease applied.

(b) Prism, sensor plane, lens and radiator.

Figure 4.15: Expansion volume and MCP-PMTs in 2014.

means of elevation, different points along the width of the plate were placed in the beam.

Data Analysis

	lens		no lens	
alignment	center	top	center	top
θ scan	67°- 127°	112°- 126°	65°- 125°	110°- 122°
x scan	1 mm - 61 mm			
z scan				16.2 cm - 104.2 cm
High statistic runs	123°,125°,127°	120°	113°,123°,125°	

Table 4.6: Prototype configurations in 2014. The alignment corresponds to the position where the plate and the prism (or lens) are aligned.

The plate tests in 2014 were performed with the NLak33 lens and without it. A summary of the prototype configurations can be seen in Table 4.6. Two different alignments of the plate and the prism (or the lens) were used. Either the top side of the plate was aligned with the top side of the prism or the lens, or the centers of the plate and the prism/lens were aligned (Fig. 4.16). The left part of the table shows the data runs with the lens. Only a small number of runs was taken with the top alignment, since large photon losses are expected in this configuration. After July, one MCP-PMT was exchanged for a tube with higher efficiency and several other tubes were rearranged in order to obtain an optimum sensor coverage of the Cherenkov patterns with selected beam polar angle configurations.

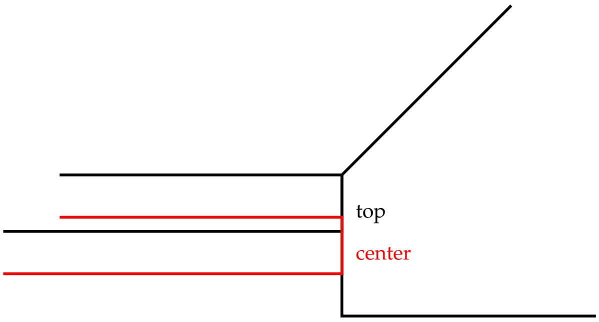

Figure 4.16: Schematic of the two alignment configurations used during the experiment, not to scale. Black: The top side of the plate coupled to the top of the front face of the prism. Red: Aligned centers of the front faces of plate and prism. If focusing optics were applied, the different alignments were between the plate and the lens.

Cherenkov Signal Hit Pattern

Figure 4.17a shows the hit pattern (after time cuts are applied) of the data recorded with a beam polar angle of $\theta = 70°$ and with the lens attached, and the comparison with the simulation (Fig. 4.17b). 80 000 triggers were used for the plots. The simulation smears the tracks uniformly to the trigger areas. This means, that a track in the simulation was only accepted in case it had a starting and an end position on trigger-sized circles of 1.5 cm radius and 6 m distance.

The occupancy plot of this run is particularly well-matching by the simulation, while other runs with $\theta = 120°$ and higher do not match as well. It was found out during the beam time, that the table, where the plate and the prism were placed, was not entirely parallel to the ground in the area, i.e not orthogonal to the rotation axis of the prototype stage. This was probably caused by the weight of the prism and introduced a $\Delta\phi$ angle between the particle track and the prism with values of $\Delta\phi = 3\,\text{mrad}$ for a track angle of $\theta = 127°$, $\Delta\phi = 0\,\text{mrad}$ for $\theta = 90°$ and $\Delta\phi = -2\,\text{mrad}$ for $\theta = 70°$. An additional $\Delta\phi$ of 7 mrad was found between the prism and the radiator plate during the polar track angle scan. The total ϕ-tilt between plate surface normal and the beam vector was therefore smallest for $\theta = 70°$.

The two highly occupied sensor columns in Fig. 4.17 are the positions of the hits of the early photons. The distance of these two columns in X depends on the alignment position of the plate. Photons with increasing propagation times were detected on the right side of the occupancy plot with increasing X-positions. At small X-positions (left side of the plot), only the latest and fewest photons were detected. The MCP-PMTs around $X = 32\,\text{cm}$ are either less sensitive or were not operated at the proper high voltage.

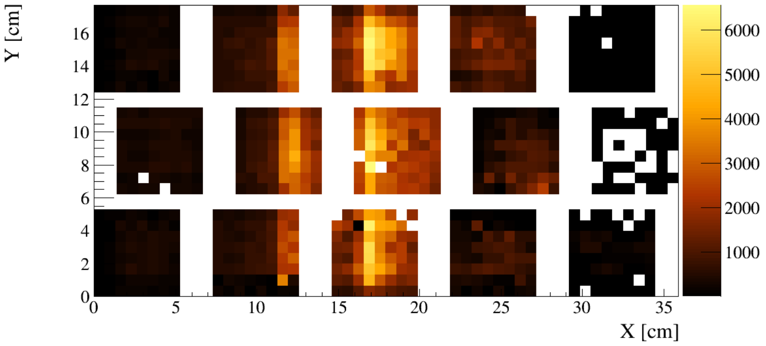

(a) Prototype data.

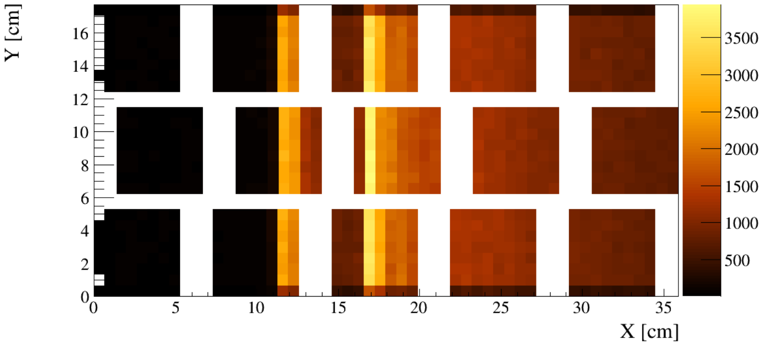

(b) Simulation.

Figure 4.17: Hit pattern of the data with $\theta = 70°$and focusing. The color represents the number of hits in the pixels.

Time Resolution of the Readout Chain

The time resolution of the electronic channels in the 2014 setup was again worse than expected, with values between 140 ps and 300 ps (instead of $\approx$ 70 ps, as evident from the TOF analysis), albeit not as bad as in 2012. A time over threshold correction did not significantly improve the timing. The channels had different time offsets which had to be corrected in order to get meaningful time information. In 2014, the PiLas light could be used for that task. The PiLas runs were performed each day before and after the beam data taking. The trigger of the PiLas light source was fed into one channel of the DAQ. Different runs showed the same relative time offsets between the channels, so runs with the best sensor occupancies were used to get an offset table (similar to the histogram in Fig. 4.7b) for the correction of the prototype data runs. Figure 4.18 shows the resulting correction map with the peak positions of the channels on the Z-axis. The fits of the pixels in the rightmost sensor column did not converge due to the bad sensor efficiency. This is, however, not crucial to the analysis, as run configurations were chosen such that not many photon hits are expected at high X values.

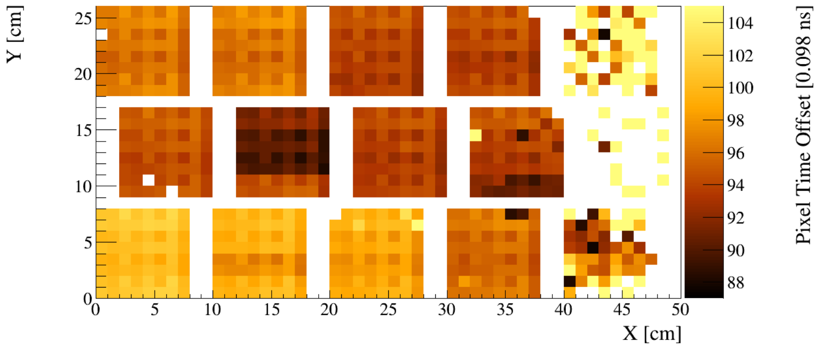

Figure 4.18: Time offset for each pixel taken from PiLas calibration runs.

Determination of the Time Offset

Maximum LH fits of the beam data can be applied to calibrate the track parameters, such as beam/plate crossing point, exact polar and azimuth beam angle, exact alignment of the optical prototype components, or the time offsets between simulation and data. Several PDFs with different parameter deviations from the expected value are created. The LH values of the observed beam data hit pattern with the PDFs are evaluated. The parameter value with the highest LH (i.e. the maximum LH estimator) is considered to be the best fit of the parameter to the data. Since many of the parameters are correlated, improving one of the parameters could deteriorate another one. A fit of a correlated parameter requires the simultaneous fit of the other parameters, which increases the dimension of the parameter space and exponentiates the effort of the fit. For the analysis of the data runs, only the time offset T_0 between the simulation and the data was calibrated with this method. The reason on the one hand is that T_0 is only correlated with the Z-position of the plate/beam intersection (different Z results in different photon path lengths and a constant offset of T_0), so the parameter space is one-dimensional. A correct value of T_0 is on the other hand crucial for a correct LH ratio test of the data as the PDFs are time-based, while the uncorrected values of the correlated parameters do not change the result of the LH ratio test much, because these parameters affect mostly the spatial hit coordinates. Another point is that the effort for the T_0-calibration is particularly small as it is done by shifting the simulated PDF successively by 100 ps and evaluating the LH values. No additional PDFs have to be created by simulation. The result of the T_0-fit is shown in Fig. 4.19.

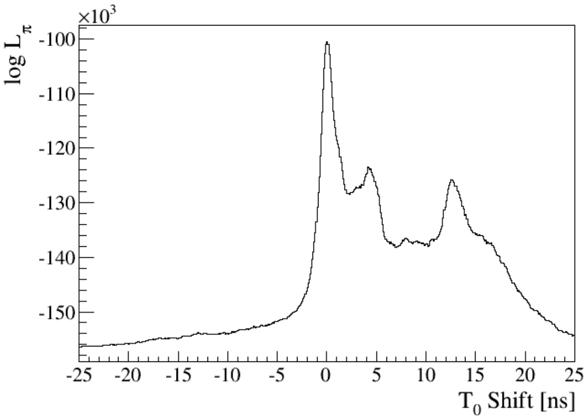

Figure 4.19: Results of the maximum log-LH fit of T_0. The maximum LH estimator is close to zero because T_0 was beforehand correct by eye.

Pion Likelihood Ratio

A LH ratio test was performed for the data with focusing and $\theta = 70°$. Pion and kaon PDFs were created by simulation and the pion PDF was used to determine T_0 of the data. The LH of each charged particle track was evaluated with the hypotheses. Figure 4.20 shows the log LH difference distribution of 340 000 charged particles. As was mentioned earlier, it is impossible to perform a proper study of separation power of pions and kaons (or protons) as the beam was composed only of pions. It is, nevertheless, possible to obtain certain quantitative results. As indicated by the red separating line in Fig. 4.20, 90% of the pion tracks have a higher LH with the pion

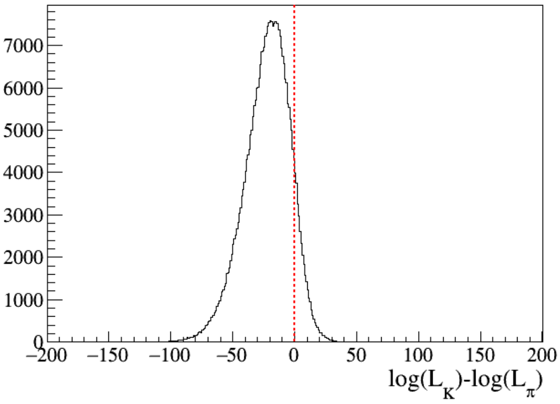

Figure 4.20: LH ratio test for the $\theta = 70°$ run. 90% of the beam pions have a larger likelihood value for the pion hypothesis than for the kaon hypothesis. The red line indicates the cut value between the pion selected particles and the kaon selected particles.

hypothesis than with a kaon hypothesis. It was observed during the study of the time-based LHs, that the pion and the kaon LH ratio distributions are usually nearly symmetrical about the point where both LH values are equal. With the assumption that this is also the case if the beam contained kaons, a value for the separation power can be calculated. The distribution in Fig. 4.20 has a fitted mean value of $\mu = -21.9 \pm 0.04$ and a width of $\sigma = 17.4 \pm 0.03$. Using Eq. 2.3, this yields a SP value of $SP = 2.518$. A (symmetrical) cut value of zero for the log LH difference separates the pion selected particles from the kaon selected particle. The pion identification efficiency (number of identified pions divided by the total number of pions) has a value of 90%, and the kaon misidentification of the pion selected particles (number of kaons identified as pions divided by the number of kaons) has a value of 10%. Due to symmetry, the same figures are true for the kaon selected particles.

Conclusion

The 2014 beam campaign was not optimal for the validation of the time-based likelihood reconstruction method. The particle beam had very unstable and low intensities, the beam focus was not defined, and the beam was composed only of pions. The time resolution of the readout electronics was again worse than expected. It was possible to show that the pions were identified as pions with the reconstruction method, although the performance did not meet the PANDA PID goals. This result can be attributed mostly to the bad time resolution of the readout.

Concerning the time resolution, an improvement to the situation in 2012 was achieved and further improvements are expected for future beam campaigns. The pion identification of the reconstruction was, however, successful and with a better timing, defined beam tracking, and a mixed hadronic beam composition the required performance will be reached.

5. Conclusion

5.1. Summary

The PANDA detector is a future hadron physics experiment at the FAIR facility. Around the antiproton-proton interaction point, a DIRC detector provides hadronic particle identification for track momenta from $0.5\,\mathrm{GeV}/c$ to $3.5\,\mathrm{GeV}/c$ and polar angles between 22° and 140°. The system is optimized for a pion/kaon separation of at least 3 standard deviations in the Barrel DIRC acceptance space. The baseline design is a scaled version of the successful BaBar DIRC with several improvements. Long rectangular bars made from synthetic fused silica are used as Cherenkov radiators. The surface quality needs to be extraordinary high in order to maintain the Cherenkov information and to preserve the photons. A tank filled with mineral oil and mirrored sides serves as volume where the photons expand before being detected.

During the development process, alternative design options were identified to improve the Barrel DIRC in terms of affordability and better usage of the observables. By using wide synthetic fused silica plates instead of narrow bars as Cherenkov radiators, the number of pieces to be polished is reduced by a factor five. The total amount of Cherenkov-active material does not change. A compact fused silica prism as expansion volume has similar optical properties as the radiators and reduces the area which has to be covered with photon sensors.

It was shown in this work that the traditional BaBar-like reconstruction approach is not suitable for the wide plates. The right Cherenkov angle can be reconstructed but only with a large combinatorial background due to the photon path ambiguities, resulting from chromatic dispersion. The short wavelength part of the photon spectrum is the part with the largest dispersion and the part of the spectrum where most of the Cherenkov photons are created. Reducing the dispersion effects by cutting into the short wavelength range would result in an unacceptable loss of Cherenkov photons. In addition, no practical filter exists to perform a static wavelength cut for a large range of photon incident angles.

A second, successful, approach was developed, which uses time-based probability density functions to perform likelihood ratio tests of the charged particles for different particle hypotheses. The studies of the plate-based geometry and the time-based likelihood approach with Monte-Carlo-generated probability density functions, have shown that the required PID performance is met and even exceeded in the entire DIRC phasespace. The time resolution of sensors and the readout chain was identified in parameter variation studies as the most important parameter for a successful PID. A first version of an analytical way to create the probability density functions was developed and showed good qualitative agreement with the simulated distributions.

Two beam campaigns were performed to validate the performance of DIRC prototypes with a plate geometry. In 2012, only a small amount of data was taken with particle momenta below 10 GeV, so that this beam time was mainly useful for gaining experiences with the setup. In 2014, a low momentum pion beam (1.7 GeV/c) was used to successfully validate the time-based likelihood approach. While a separation power test of pions and kaons was impossible due to the beam characteristics, a likelihood ratio test was performed with pions for a selected prototype configuration and showed a PID efficiency of 90%, although the performance requirement of PANDA was not met. In both beam campaigns the time resolution of the electronics was considerably worse than expected and is considered to be the main contribution of the achieved performance.

5.2. Outlook

A novel kind of detector, based on the DIRC principle, is capable of charged particle identification at a momentum range above typical time-of-flight devices. It features a thin layer of material in the direction of the particle tracks and with the BaBar DIRC only one instance of a DIRC counter exists so far. Currently, several DIRC detectors are in the process of being built or developed.

The recent breakthroughs in the life-times of micro-channel plate photomultiplier tubes make these an intriguing option for fast pixelated photon sensor that were not available during the conception phase of the BaBar DIRC. The work performed for this thesis is an important technology step for the PANDA Barrel DIRC and similar devices. The time-based likelihood approach could be the ideal reconstruction for DIRC counters as it makes optimal use of the fast timing. The approach itself is independent of the radiator geometry and could be used for the plate-based geometry as well as for the baseline design with narrow bars. If the time resolution of the sensors and electronics is further improved, it is expected that the time-based likelihood approach is superior to the traditional BaBar-like reconstruction.

The difficulty is to apply the analytical equations for the calculation of probability density functions to the individual DIRC designs. A preliminary approach was shown in this work to prove that it is (in the case of the PANDA Barrel DIRC) possible to find the equations. The final equations have to be developed when the design options, e.g. the kind of focusing optics, are agreed on.

With even better timing and appropriate equations it is possible that DIRC counters could one day be used for hadronic particle identification up to 6 GeV/c or higher.

A. Information on the Prototype Plates

Two wide radiator plates were ordered in 2012 and produced by InSync, Inc. in order to be used for the prototype testing. The plates met all specifications. Table A.1 shows the demanded and delivered specifications for one of the plates. Quality assurance was performed by the manufacturer.

A data sheet of the roughness determination for one side surface can be seen in Fig. A.1. Ten measurements were done in a small surface area of $\sim 2 \times 2\,\mathrm{mm}^2$. The results were averaged afterwards to obtain the value for the surface roughness for this surface.

Property		**Specification**	**Measured**
Length	[mm]	1225±1	1224.94
Width	[mm]	175±1	174.75
Thickness	[mm]	17±1	17.11
Squareness	[mrad]	0.5	0.29 (RMS)
Roughness Faces & Sides	[Å RMS]	10	3.6
Roughness Ends	[Å RMS]	20	≈17
TTV Face to Face	[µm]	25	15
TTV Side to Side	[µm]	25	0

Table A.1: Specifications of one of the plates. For the other plate the specs are similar. TTV: Total thickness variation.

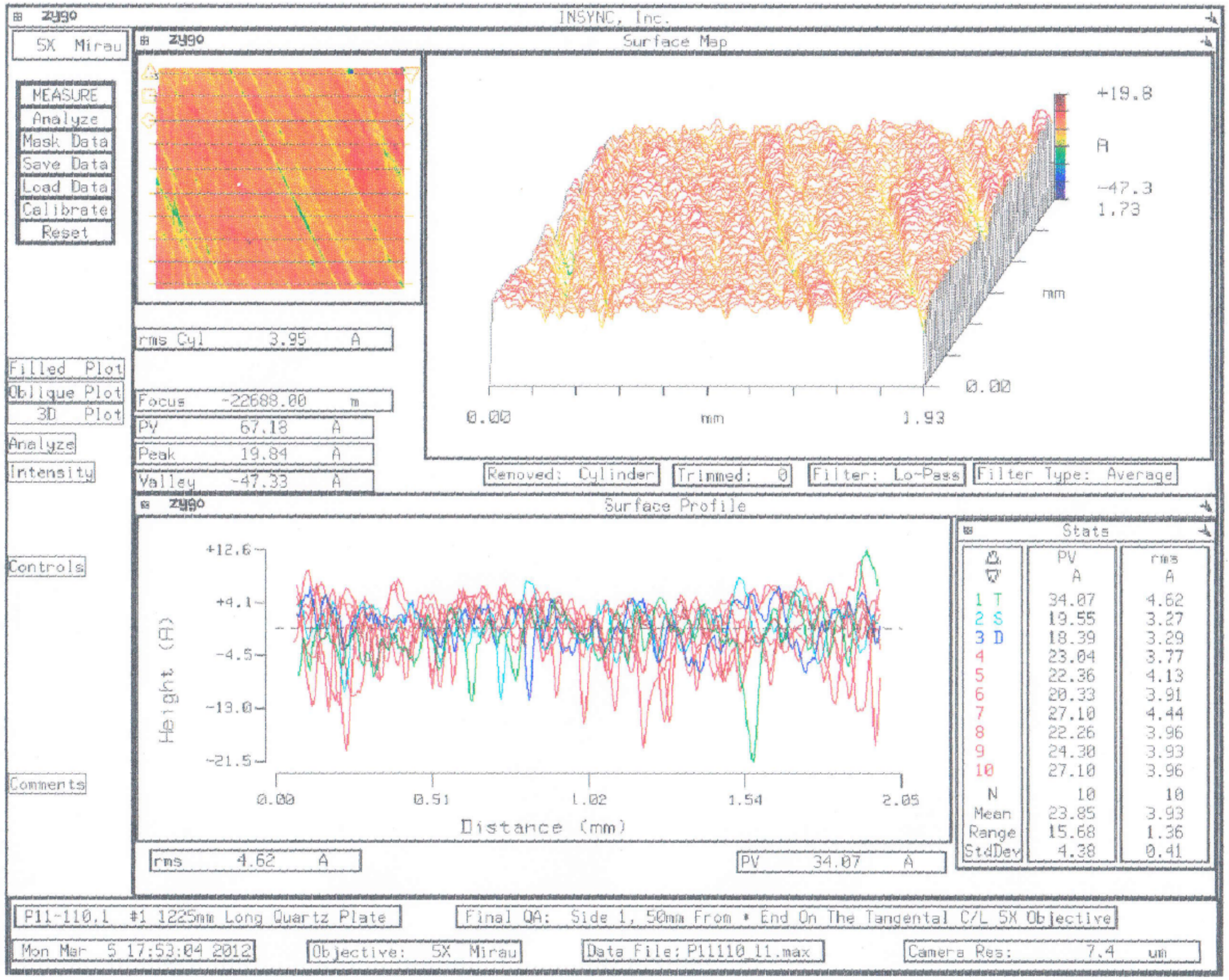

5X Mirau

rms Cyl 3.95 A

Focus -22688.00 m

PV 67.18 A

Peak 19.84 A

Valley -47.33 A

Removed: Cylinder

Trimmed: 0

Filter: Lo-Pass

Filter Type: Average

rms 4.62 A

PV 34.07 A

	PV A	rms A
1 T	34.07	4.62
2 S	19.55	3.27
3 D	18.39	3.29
4	23.04	3.77
5	22.36	4.13
6	20.33	3.91
7	27.10	4.44
8	22.26	3.96
9	24.30	3.93
10	27.10	3.96
N	10	10
Mean	23.85	3.93
Range	15.68	1.36
StdDev	4.38	0.41

P11-110.1 #1 1225mm Long Quartz Plate

Final QA: Side 1, 50mm From • End On The Tangental C/L 5X Objective

Mon Mar 5 17:53:04 2012

Objective: 5X Mirau

Data File: P11110_11.max

Camera Res: 7.4 um

Figure A.1: Quality assurance sheet for the roughness measurement of one of the side surfaces of one of the plates.

B. Derivation of the Uncertainties in Chapter 3.6

The position of the time peaks t in of Eq. 3.19 depends on the projected photon path l_z, the refractive group index n_{Gr}, and the polar angle θ of the photon in the plate coordinate system:

$$t = \frac{l_z \cdot n_{\mathrm{Gr}}}{\cos(\theta) \cdot c_0}$$

The uncertainty σ_t is determined by:

$$\begin{aligned}
\sigma_t &= \sqrt{\left(\frac{\partial t}{\partial l_z}\sigma_{l_z}\right)^2 + \left(\frac{\partial t}{\partial \theta}\sigma_\theta\right)^2 + \left(\frac{\partial t}{\partial n_{\mathrm{Gr}}}\sigma_{n_{\mathrm{Gr}}}\right)^2} \\
&= \sqrt{\left(\frac{n_{\mathrm{Gr}}}{\cos(\theta) \cdot c_0}\sigma_{l_z}\right)^2 + \left(\frac{l_z \cdot n_{\mathrm{Gr}}}{c_0}\frac{\tan(\theta)}{\cos(\theta)}\sigma_\theta\right)^2 + \left(\frac{l_z}{\cos(\theta) \cdot c_0}\sigma_{n_{\mathrm{Gr}}}\right)^2} \\
&= t\sqrt{\left(\frac{\sigma_{l_z}}{l_z}\right)^2 + (\sigma_\theta \cdot \tan(\theta))^2 + \left(\frac{\sigma_{n_{\mathrm{Gr}}}}{n_{\mathrm{Gr}}}\right)^2}
\end{aligned}$$

According to Eq. 3.12, the polar angle θ of the photon depends on the projected photon angles α_x and α_y by

$$\theta = \arctan\left(\sqrt{\frac{1}{\tan^2(\alpha_x)} + \frac{1}{\tan^2(\alpha_y)}}\right),$$

with an uncertainty given by:

$$\begin{aligned}
\sigma_\theta =& \sqrt{\left(\frac{\partial \theta}{\partial \alpha_x}\sigma_{\alpha_x}\right)^2 + \left(\frac{\partial \theta}{\partial \alpha_y}\sigma_{\alpha_y}\right)^2} \\
=& \frac{1}{1/\tan^2(\alpha_x) + 1/\tan^2(\alpha_y) + 1} \cdot \frac{1}{\sqrt{1/\tan^2(\alpha_x) + 1/\tan^2(\alpha_y)}} \\
& \cdot \sqrt{\left(\frac{1}{\tan^3(\alpha_x)} \cdot \frac{1}{\cos^2(\alpha_x)}\sigma_{\alpha_x}\right)^2 + \left(\frac{1}{\tan^3(\alpha_y)} \cdot \frac{1}{\cos^2(\alpha_y)}\sigma_{\alpha_y}\right)^2}
\end{aligned}$$

$$
\begin{aligned}
&= \frac{1}{\tan^2(\theta)+1} \cdot \frac{1}{\tan(\theta)} \sqrt{\left(\frac{\sigma_{\alpha_x}}{\tan(\alpha_x)\sin^2(\alpha_x))}\right)^2 + \left(\frac{\sigma_{\alpha_y}}{\tan(\alpha_y)\sin^2(\alpha_y))}\right)^2} \\
&= \frac{\cos^2(\theta)}{\tan(\theta)} \sqrt{\left(\frac{\sigma_{\alpha_x}}{\tan(\alpha_x)\sin^2(\alpha_x))}\right)^2 + \left(\frac{\sigma_{\alpha_y}}{\tan(\alpha_y)\sin^2(\alpha_y))}\right)^2}
\end{aligned}
$$

The photon angle α_x projected into the X-Z plane of the plate coordinate system depends on the photon path projection l_z and the photon hit position x on the unfolded hit plane (Eq. 3.10):

$$
\alpha_x = \arctan\left(-\frac{x}{z}\right)
$$

The uncertainty is given by:

$$
\begin{aligned}
\sigma_{\alpha_x} &= \sqrt{\left(\frac{\partial \alpha_x}{\partial x}\sigma_x\right)^2 + \left(\frac{\partial \alpha_x}{\partial z}\sigma_z\right)^2} \\
&= \frac{1}{(x/z)^2+1} \cdot \sqrt{\left(\frac{\sigma_x}{z}\right)^2 + \left(\frac{x\sigma_z}{z^2}\right)^2} \\
&= \frac{1}{x^2+l_z^2} \cdot \sqrt{(l_z\sigma_x)^2 + (x\sigma_{l_z})^2}
\end{aligned}
$$

The uncertainty of the projected photon path σ_{l_z} is nonzero if the considered photon path ambiguity has a reflection on the top side of the prism. The situation is visualized in Fig. B.1. σ_{l_z} depends on the opening angle γ of the prism and on the Z-projection p_z of the mirror image of the pixel size p:

$$
\sigma_{l_z} = p_z/\sqrt{12} = p \cdot \cos(\pi/2 - 2\gamma)/\sqrt{12} = p \cdot \sin(2\gamma)/\sqrt{12}.
$$

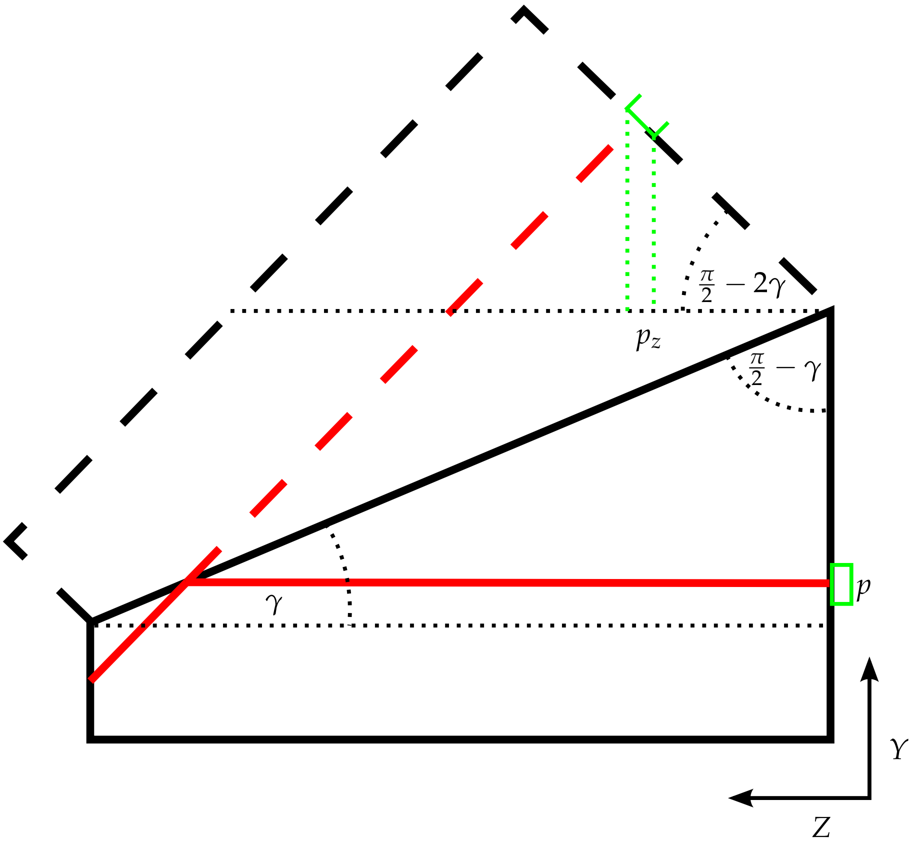

Figure B.1: Schematic view of a prism with an opening angle of γ. The incoming photon ambiguity is highlighted with red and reflected at the top side of the prism. The dashed lines indicate the mirror images of the prism and the photon path. p is the pixel size and p_z the projection of the pixel image on the Z-axis.

Ausführliche Zusammenfassung

Das PANDA (antiProton Annihilation in DArmstadt) Experiment ist eine der vier wissenschaftlichen Säulen des zukünftigen FAIR (Facility for Antiproton and Ion Research) Projektes, welches derzeit als Erweiterung der Beschleunigeranlage am GSI Helmholtzzentrum für Schwerionenforschung entsteht und voraussichtlich 2018 in Betrieb genommen werden wird. Der Forschungsschwerpunkt des PANDA Experiments liegt in der Ergründung der ungeklärten Aspekte der Quantenchromodynamik. Die Antiprotonen, die während des Experiments auf ein Protonentarget geschossen werden, werden in der Beschleunigerkette der FAIR-Anlage erzeugt. Zunächst werden Protonen im Linearbeschleuniger p-Linac und im bereits bestehenden Synchrotron SIS18 vorbeschleunigt, um danach im neuen Hauptbeschleuniger, dem Synchrotron SIS100, auf den finalen Impuls von 30 GeV/c gebracht zu werden. Anschließend dient ein Antiprotonen Produktionstarget dazu, etwa 10^7 Antiprotonen pro Sekunde zu erzeugen, welche in weiteren Speicherringen stochastisch gekühlt und akkumuliert werden. Im HESR (High Energy Storage Ring) können die Antiprotonen schließlich auf Strahlimpulse zwischen 1,5 GeV/c und 15 GeV/c beschleunigt und im PANDA Spektrometer mit Protonentargets zur Reaktion gebracht werden. Der HESR kann je nach wissenschaftlicher Zielsetzung wahlweise im *High Luminosity Mode* (Maximale Luminosität $L_{\max} = 2 \times 10^{32}\,\mathrm{cm}^{-2}\mathrm{s}^{-1}$, Strahlimpulsauflösung $\Delta p/p = 10^{-4}$) oder im *High Resolution Mode* ($L_{\max} = 2 \times 10^{31}\,\mathrm{cm}^{-2}\mathrm{s}^{-1}$, $\Delta p/p = 10^{-5}$) betrieben werden.

Um möglichst den vollen Raumwinkel- und Impulsbereich der Reaktionsprodukte messen zu können, besteht der PANDA Detektor aus zwei eigenständigen Systemen. Das *Target Spectrometer* umschließt das Protonentarget und deckt den Polarwinkel θ (die Strahlrichtung des Antiprotonstrahls entspricht einem Polarwinkel von 0°) über 5° vertikal und 10° horizontal ab. Reaktionsprodukte mit geringem transversalen und hohem longitudinalen Impuls werden im *Forward Spectrometer*, bei Polarwinkeln unter 5° vertikal und 10° horizontal, detektiert. Jedes dieser Spektrometer enthält Komponenten zur wissenschaftlichen Analyse der Reaktionen. Im Target Spectrometer dienen primär zwei, aufgrund des DIRC-Prinzips (Detection of Internally Reflected Cherenkov light) sehr kompakte, ringabbildende Cherenkov-Detektoren der hadronischen Teilchenidentifikation. Der PANDA Barrel DIRC liegt fassförmig um die zentralen Spur- und Vertexdetektoren und deckt den Raumwinkelbereich $22° < \theta < 140°$ ab. Das angestrebte Ziel des Barrel DIRCs ist eine 3σ-Identifikation aller geladener Endzustände (i.B. eine Separation von Kaonen und Pionen) bei Teilchenimpulsen zwischen 500 MeV/c und 3,5 GeV/c.

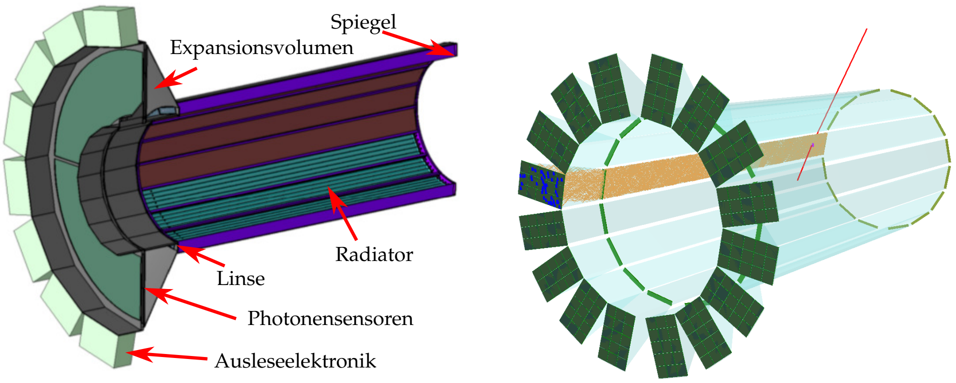

(a) CATIA-Zeichung mit longitudinalem Schnitt des grundlegenden Designs des PANDA Barrel DIRC. Die wichtigsten Elemente des DIRC sind angegeben.

(b) Zeichnung einer Simulation mit der alternativen Geometrie (breite Platten und kompakte Glasprismen). In rot ist ein durchgehendes Myon dargestellt. Propagierende Cherenkov-Photonen sind in orange, Sensorsignale von Photonen in blau dargestellt.

Figure B.2: Gegenüberstellung der PANDA Barrel DIRC Design Optionen.

Der PANDA Barrel DIRC ist eine skalierte und weiterentwickelte Version des sehr erfolgreichen DIRC Detektors, welcher für das BaBar Experiment am SLAC (Stanford Linear Accelerator Center) entwickelt und über 10 Jahre lang betrieben wurde. Durch die zwischenzeitlichen technologischen Verbesserungen bei Photonensensoren ist es möglich, pixelierte kompakte Photonen-Auslesesensoren mit hoher zeitlicher Präzision beim PANDA Barrel DIRC zu verwenden. Dadurch ergeben sich die wesentlichen Verbesserungen im Vergleich zum BaBar DIRC: kompakte Sensorik, hohe zeitliche Messauflösung, ein kompaktes Photonen-Expansionsvolumen und fokussierende Optik. Das grundlegende Design des PANDA Barrel DIRC ist in Abb. B.2a dargestellt. Es besteht aus 80 langen synthetischen Quarzglasstäben mit einer Länge von jeweils 240 cm und einer Querschnittfläche von 1,7 cm × 3,2 cm. Als Expansionsvolumen dient ein großer Tank, gefüllt mit Mineralöl als optischem Medium. Die komplette Rückwand dieses Volumens ist mit Mikrokanalplatten-Photonenvervielfachern (MCP-PMT) bestückt. Etwa 15 000 Pixel werden ausgelesen.

Die vorliegende Dissertation behandelt die Untersuchung einer Design-Alternative des Detektors, die entscheidende Vorteile mit sich bringt und von aktuellen Entwicklungen des Belle-II TOP inspiriert wurde. Die Alternative ist in Abb. B.2b zusammen mit einem Myonendurchgang als Geant4 Simulation dargestellt. Es werden breite Radiatorplatten anstelle von jeweils fünf Stäben verwendet, sodass sich das Materialvolumen des synthetischen Quarzglases nicht verringert, die Anzahl der produzierenden Teile aber um den Faktor 5 reduziert. Die Oberflächenbehandlung der Radiatoren ist eine der Hauptkostentreiber des gesamten Systems, weil einzelne Photonen verlustfrei und informationserhaltend über die gesamte Radiatorlänge mittels Totalreflexion transportiert werden müssen. Dazu ist eine sehr hohe Material- und Oberflächengüte erforderlich. Die Reduktion der Glasstücke bringt eine große Kostenersparnis mit sich.

Als zweite Designalternative kommen kompakte Quarzglasprismen anstelle des Öltanks zur Anwendung. Dies hat mehrere Vorteile: Die 16 azimutalen Segmente (siehe Abb. B.2b) sind dadurch optisch voneinander isoliert und es genügt, die Rekonstruktionsalgorithmen für ein Segment zu entwickeln, ohne optische Kontamination berücksichtigen zu müssen. Das Quarzglas-Expansionsvolumen hat günstigere optische Eigenschaften als Mineralöl und ist sauberer zu handhaben. Die Anzahl der Pixel, und somit der Sensoren, kann reduziert werden, was wiederum in einer signifikanten Kostenersparnis resultiert. Diese Designalternativen stellen dadurch einerseits eine Weiterentwicklung der (noch jungen) DIRC Technologie mit Verbesserungen der Leistungsfähigkeit dar und gewährleisten andererseits auch in Zukunft die Wirtschaftlichkeit der Produktionskosten des PANDA Barrel DIRC und davon abgeleiteter Detektoren.

Die bewährten BaBar-artigen Rekonstruktionsalgorithmen können für diese Designoptionen allerdings nicht verwendet werden, weil sie auf dünne, schmale Radiatorstäbe im Vergleich zur Tiefe des Expansionsvolumens angewiesen sind. Der Stabquerschnitt kann beim BaBar-Ansatz vernachlässigt und der DIRC Detektor als Camera Obscura betrieben werden. Diese Voraussetzung ist bei der Geometrie mit breiten Platten nicht gegeben. Im Rahmen dieser Arbeit wurde eine Modifikation des BaBar-Ansatzes entwickelt, bei der der zu rekonstruierende (räumliche) Photonen-Richtungswinkel in zwei orthogonale Ebenen projiziert wird. Die beiden Winkelprojektionen werden separat nach unterschiedlichen Methoden rekonstruiert und anschließend zusammengesetzt. Der resultierende Richtungsvektor ergibt, kombiniert mit der Teilchenspurrichtung, den Cherenkov-Winkel des Photons.

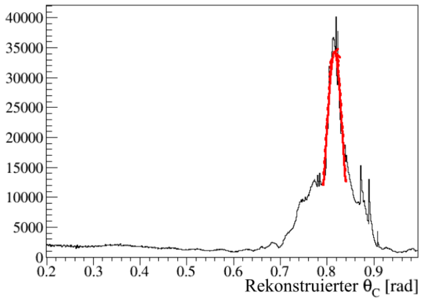

Figure B.3: Verteilung der rekonstruierten Cherenkov-Photonen von 2 000 simulierten Myonen mit polaren Spurwinkel von $\theta = 25°$ und Impulsen von $p = 1\,\mathrm{GeV}/c$.

Dabei treten viele Winkelambiguitäten auf, die ebenso als Ergebnis der Rekonstruktion betrachtet werden müssen, und die als kombinatorischer Untergrund in das rekonstruierte Cherenkov-Winkelspektrum (Abb. B.3) eingehen. Systematische Untersuchungen haben gezeigt, dass der größte Teil des Untergrundes durch die chromatische Dispersion des Radiatormaterials verursacht wird. Die Dispersion lässt sich, wenn überhaupt, nur mit aufwändigen Mitteln reduzieren und nur mit einem unakzeptablen Verlust von Photonen.

Ein völlig anderer Rekonstruktionsansatz ist von den Studien zum Belle-II TOP inspiriert und hat sich als wesentlich erfolgreicher herausgestellt. Durch die zeitlich schnellen und präzisen Photonensensoren ist es möglich, eine zeitbasierte Auftreff-Wahrscheinlichkeitsdichte (PDF) der detektierten Photonen zu erstellen. Die PDF ist 3-dimensional (X- und Y-Koodinate und Zeitpunkt des detektierten Photons) und deckt den ganzen Koordinatenraum der Sensormessungen ab (komplette Sensorebene in einem Zeitfenster von 100 ns). Mittels dieser PDF, die pixelweise aufgespalten wird, kann für jedes Teilchenereignis eine Likelihoodfunktion berechnet und ein Likelihood-Quotienten-Test (LQ-Test) für alle Teilchenhypothesen ($e^{\pm}$, $\mu^{\pm}$, $\pi^{\pm}$, $K^{\pm}$, $p^{\pm}$ und Untergrundereignisse) erstellt werden. Abbildung B.4a zeigt das gemessene Photonenmuster auf der Sensorebene eines Segments mit 6 × 3 Sensoren und jeweils 8 × 8 Pixeln. Das Muster stammt aus einer Simulation, bei der 100 000

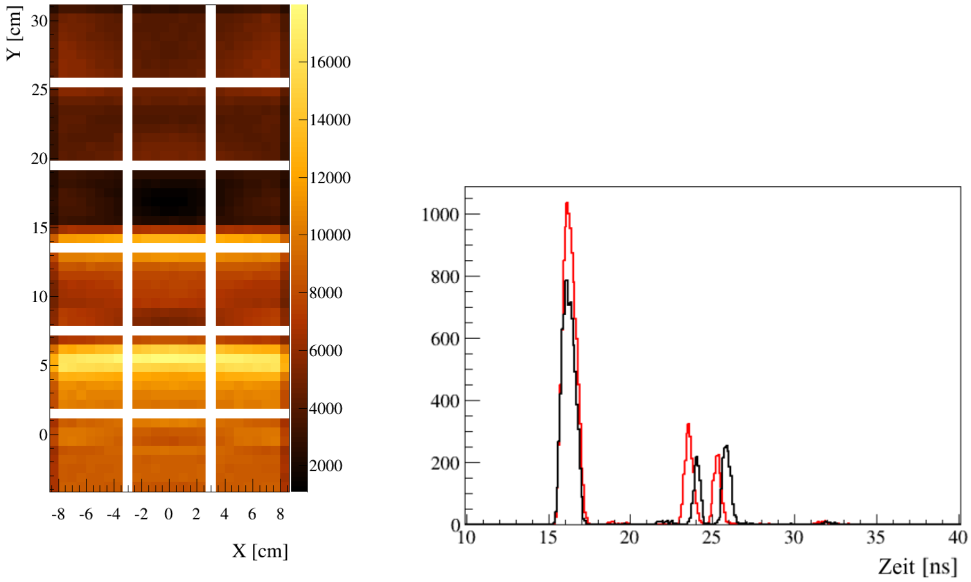

(a) X-Y-Muster von Pionen.

(b) Zeitliche Verteilung der Photonenmusters von Pionen (rot) und Kaonen (schwarz) in einem ausgewählten Pixel.

Figure B.4: Simulierte Photonenmuster von 100 000 geladenen Teilchen mit $p = 3{,}5\,\mathrm{GeV}/c$ und $\theta = 22°$ in räumlichen und zeitlichen Koordinaten.

Pionen durch die Mitte der Radiatorplatte bei einem Impuls von p =3,5 GeV/c und einem Polarwinkel von θ =22° mit Geant4 propagiert wurden. Passend dazu zeigt Abb. B.4b die zeitliche Verteilung der gemessen Cherenkov-Photonen für einen ausgewählten Pixel. Die PDFs erhält man, indem man diese Verteilungen normiert, sodass das Integral über alle Pixel und Zeiten der Zahl der erwarteten Sensorsignale, inklusive Sensorrauschen, pro DIRC Ereignis entspricht. Die rote Verteilung stammt von Pionenereignissen, die schwarze Verteilung von Kaonenereignissen. Die Unterschiede zwischen beiden Verteilungen sind gering, aber erkennbar. Je mehr Photonen pro DIRC-Ereignis gemessen werden können, desto deutlicher werden die Unterschiede bei den Likelihoodwerten. Bei geringeren Teilchenimpulsen unterscheiden sich die Verteilungen signifikant.

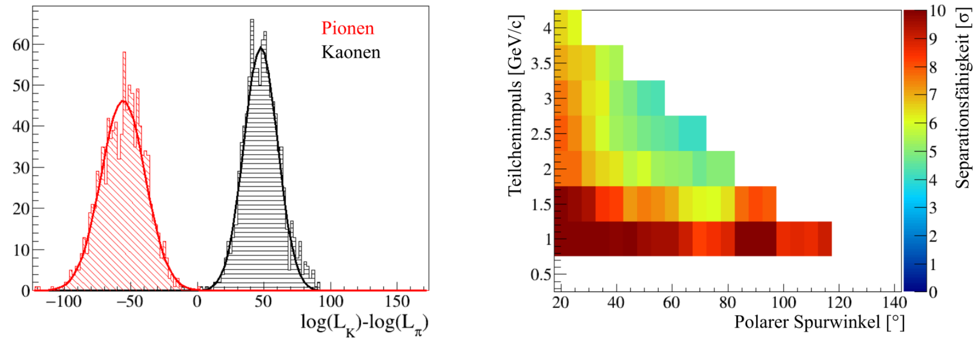

(a) LQ-Verteilungen von Pionen (rot) und Kaonen (schwarz). Die Separation der Mittelwerte beider Kurven beträgt (7,2±0,2) σ.

(b) Phasenraumabrasterung der LQ-Tests über den kompletten Polarwinkel/Impuls-Akzeptanzbereich des PANDA Barrel DIRC. Auf der Farbskala sind die Pion/Kaon-Separationen aufgetragen.

Figure B.5: Separationswerte von Pionen und Kaonen als Vielfache der gemittelten Standardabweichung der LQ-Verteilungen. Sowohl die PDFs als auch die jeweils 1 000 Testteilchen wurden durch Simulation erzeugt.

Das Ergebnis des LQ-Tests ist in Abb. B.5a dargestellt. Es wurde für beide farbige Verteilungen der Wert $\log(L_K) - \log(L_\pi)$ aufgetragen. Die rote Verteilung entspricht den LQ Werten von 1 000 simulierten Pionen, die schwarze Verteilung denen 1 000 simulierter Kaonen. Die Verteilungen sind klar voneinander getrennt, entsprechend einer Separation von (7,2±0,2) gemittelter Standardabweichungen. Abbildung B.5b zeigt die Separationswerte für alle relevanten Punkte des PANDA Barrel DIRC Akzeptanz-Phasenraums. Die Zielsetzung von mindestens 3σ Separation zwischen Pionen und Kaonen wird an allen Punkten im Phasenraum erreicht. Die Tests wurden auch an einer Geometrie mit fokussierender Optik durchgeführt und erfüllen ebenfalls an jedem Phasenraumpunkt die Zielsetzung. Verschiedene systematische Untersuchungen wurden mit Monte-Carlo simulierten PDFs durchgeführt und zeigen, dass insbesondere eine sehr hohe Qualität der Plattenoberflächen (Rauheitswerte von etwa 10 - 20 Å im quadratischen Mittel) und eine exzellente Zeitauflösung der Ausleseelektronik (ca. 100 - 200 ps) für die Leistungsfähigkeit dieser Methode benötigt wird.

Ein erster Ansatz zur analytischen Berechnung der PDFs wurde entwickelt und zeigt gute qualitative Übereinstimmungen mit simulierten Photonenmustern. Ein analytischer Ansatz ist nötig, weil der Parameterraum der PDFs hochdimensional ist und für jeden Punkt in diesem Raum eigene PDFs erzeugt werden müssen. Dies ist mittels Simulation sehr aufwändig und nicht in Echtzeit durchführbar. Mit analytischen Funktionen kann hingegen jede PDF bei Bedarf schnell erzeugt und der Parameterraum dicht abgedeckt werden.

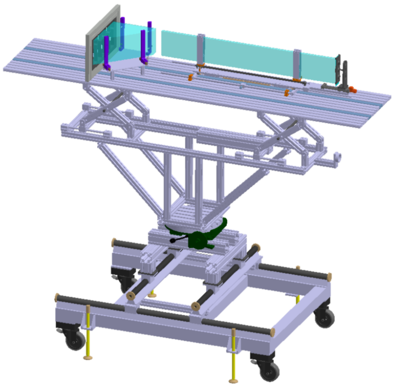

Figure B.6: Schematische Zeichnung des Prototypenaufbaus von 2014. Der eigentliche DIRC Prototyp (Optische Komponenten und Auslesesensorik) befand sich auf einem Gestell, welches in drei Richtungen verschiebbar und um die vertikale Achse drehbar war.

Zur Validierung der Rekonstruktionsmethode und der Radiatorplattengeometrie wurden mehrere Strahlzeiten an der GSI-Anlage und am CERN *Proton Synchrotron* im T9 Testbereich durchgeführt. Während am CERN in 2012 nur wenige Datensätze mit einem Plattenprototypen aufgezeichnet wurden, lag der Hauptfokus bei der GSI Strahlzeit im Sommer 2014 bei Tests der Radiatorplatte. Ein Pionenstrahl mit festem Impuls von 1,7 GeV/c stand zur Verfügung. Abbildung B.6 zeigt den prinzipiellen Aufbau der Prototypkonstruktion von 2014. Eine einzelne Platte und das Expansionsprisma mit Auslesesensoren (nicht dargestellt) war auf einem Gestell montiert, das um die vertikale Achse drehbar (für verschiedene Strahleinfallswinkel) und in allen Raumrichtungen verschiebbar (für verschiedene Strahlpositionen) war. Die gemessenen Photonenmuster bei einem Polarwinkel von 70° sind in Abb. B.7 zu sehen, mit einer Gegenüberstellung von Simulation (Abb. B.7a) und Prototypdaten (Abb. B.7b).

Mit nur einer Teilchensorte kann keine Separation getestet werden, aber ein LQ-Test

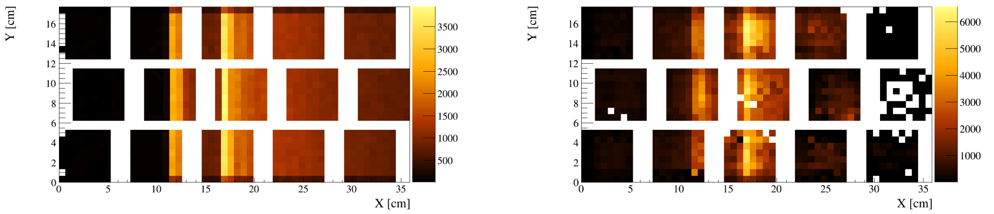

(a) Simuliertes Photonenmuster.

(b) Gemessenes Photonenmuster.

Figure B.7: Gegenüberstellung der Photonenmuster aus Simulation und Prototypdaten. Eine 5×3 Sensorenmatrix wurde zur Strahlzeit 2014 verwendet. Die Muster wurden von jeweils 80 000 Pionen mit p =1,7 GeV/c und θ =70° erzeugt.

ist dennoch möglich. Abbildung B.8 zeigt das Ergebnis der Analyse des LQ-Test

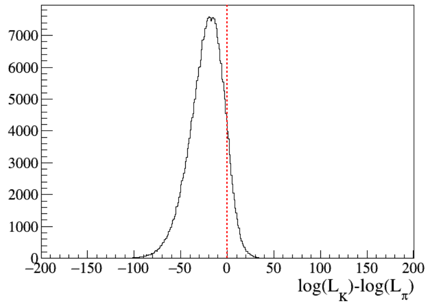

Figure B.8: LQ-Verteilung der gemessenen Pionen (p =1,7 GeV/c, θ =70°). Die hinzugefügte rote Trennungslinie zeigt, dass rund 90% der Pionen höhere Likelihoodwerte mit einer Pionenhypothese als mit einer Kaonenhypothese haben.

der detektierten Pionenereignisse bei einem Polarwinkel von 70°. Die hinzugefügte Nulllinie separiert die Teilchen, die größere Likelihoodwerte mit einer Pionenhypothese haben (links) und die Teilchen mit einer größeren Kaonenhypothese. Die dargestellte Verteilung entspricht einer Pionen-Identifikationseffizienz von 90% und einer Fehlidentifikation der Pionen als Kaonen von 10%.

Die Ergebnisse dieser Arbeit helfen bei der Auswahl der PANDA Barrel DIRC Design Optionen und werden Bestandteil des Technischen Design Reports werden, welcher voraussichtlich 2016 veröffentlicht wird. Als weitere Studien zum Plattendesign und der Rekonstruktionsmethode müssen weiterhin Prototypen in Strahlzeiten getestet werden, um insbesondere die Leistungsfähigkeit der Rekonstruktionsmethode bei allen relevanten Strahl-Polarwinkeln und den Einfluss von fokusierender Optik zu untersuchen. Der entwickelte Rekonstruktionsansatz, basierend auf zeitlichen PDFs, kann zudem auch auf die traditionelle Stabgeometrie mit potenziell vielversprechenden Resultaten angewandt werden.

Bibliography

[1] PANDA Collaboration, "Physics Performance Report for PANDA: Strong Interaction Studies with Antiprotons", arXiv:0903.3905 [hep-ex] (2009).

[2] P. Gianotti, "Results and perspectives in hadron spectroscopy", Phys.Scripta **T150**, 014014 (2012).

[3] BaBar Collaboration, "Observation of a Broad Structure in the $\pi^+\pi^- J/\psi$ Mass Spectrum around $4.26\,\mathrm{GeV/c^2}$", Phys. Rev. Lett. **95**, 142001 (2005).

[4] S.-K. Choi et al., "Observation of a Narrow Charmoniumlike State in Exclusive $B^\pm \to K^\pm \pi^+\pi^- J/\psi$ Decays", Phys. Rev. Lett. **91**, 262001 (2003).

[5] PANDA Collaboration, "Technical Design Report for the PANDA Internal Targets: The Cluster-Jet Target and Developments for the Pellet Target", (2012).

[6] *GSI Helmholtzzentrum für Schwerionenforschung GmbH*, `https://www.gsi.de/` (visited on 11/21/2014).

[7] *Facility for Antiproton and Ion Research: NUSTAR Physics*, `http://www.fair-center.eu/public/experiment-program/nustar-physics.html` (visited on 11/21/2014).

[8] *Facility for Antiproton and Ion Research: APPA Physics*, `http://www.fair-center.eu/public/experiment-program/appa-physics.html` (visited on 11/21/2014).

[9] P. Senger, "The Compressed Baryonic Matter Experiment at FAIR in Darmstadt", Journal of Physics G: Nuclear and Particle Physics **30**, S1087 (2004).

[10] FAIR, *Conceptual Design Report*, (2001) `http://www.fair-center.de/fileadmin/fair/publications_FAIR/FAIR_CDR.pdf` (visited on 03/11/2016).

[11] GSI, *Wissenschaftliche Zielsetzungen und Forschungsprogramme : FAIR - Facility for Antiproton and Ion Research ; Statusbericht Juli 2005* (GSI, Darmstadt, 2005), 52 S.

[12] *GSI - Aufbau der FAIR-Beschleunigeranlage*, `http://www.fair-center.eu/typo3temp/pics/04ff64ac86.jpg` (visited on 03/09/2016).

[13] H. Vormann et al., "Advanced UNILAC Upgrade for FAIR", Proceedings of Linear Accelerator Conference LINAC2010, Tsukuba (2010).

[14] K. Knie et al., "Concept for the Antiproton Production Target at FAIR", Proceedings of IPAC2012, New Orleans, Luisiana, USA (2012).

[15] A. Dolinskii et al., "The CR-RESR Storage Ring Complex of the FAIR Project", Proceedings of the 11th European Conference, EPAC 2008, Genoa, Italy, June 23-27 (2008).

[16] R. Maier, "The High-Energy Storage Ring HESR", Proceedings of 2011 Particle Accelerator Conference, New York, NY, USA (2011).

[17] PANDA Collaboration, "Technical Design Report for the: PANDA Micro Vertex Detector", arXiv:1207.6581 [physics] (2012).

[18] PANDA Collaboration, "Technical Design Report for the: PANDA Straw Tube Tracker", The European Physical Journal A **49** (2013).

[19] R. Arora et al., "A Large GEM-TPC Prototype Detector for Panda", Physics Procedia, Proceedings of the 2nd International Conference on Technology and Instrumentation in Particle Physics (TIPP 2011) **37**, 491–498 (2012).

[20] M. Düren et al., "The PANDA 3D Disc DIRC", JINST **7**, C01059 (2012).

[21] PANDA Collaboration, "Technical Design Report for PANDA Electromagnetic Calorimeter (EMC)", arXiv:0810.1216 [hep-ex, physics:physics] (2008).

[22] PANDA Collaboration, "Technical Design Report for the PANDA Solenoid and Dipole Spectrometer Magnets", arXiv:0907.0169 [hep-ex, physics:physics] (2009).

[23] A. Wronska, "Forward Spectrometer of PANDA - Requirements and Solutions", International Journal of Modern Physics A **24**, 471–475 (2009).

[24] P. Carter, "The Aerogel Radiator of the HERMES RICH: on Behalf of the HERMES Collaboration", Nucl. Instr. and Meth. A **433**, 392–395 (1999).

[25] M. Patsyuk, "Simulation, Reconstruction and Design Optimization for the PANDA Barrel DIRC", PhD Thesis (Goethe-Universität Frankfurt, 2015).

[26] L. Schmitt, "The PANDA Detector at FAIR", Nucl. Instr. and Meth. A **581**, 542–544 (2007).

[27] P. A. Čerenkov, "Visible Radiation Produced by Electrons Moving in a Medium with Velocities Exceeding that of Light", Phys. Rev. **52**, 378–379 (1937).

[28] I. Tamm and I. Frank, "Coherent Radiation of Fast Electrons in Medium", Doklady Akademii Nauk SSSR, 107 (1937).

[29] A. Karle et al., "IceCube - the Next Generation Neutrino Telescope at the South Pole", Nuclear Physics B - Proceedings Supplements, Proceedings of the XXth International Conference on Neutrino Physics and Astrophysics **118**, 388–395 (2003).

[30] The LHCb RICH Collaboration, "Performance of the LHCb RICH Detector at the LHC", The European Physical Journal C **73**, 1–17 (2013).

[31] D. L. Thorek et al., "Cerenkov Imaging - a New Modality for Molecular Imaging", American Journal of Nuclear Medicine and Molecular Imaging **2**, 163–173 (2012).

[32] B. Ratcliff and J. Schwiening, "Cherenkov Counters", Handbook of Particle Detection and Imaging, C. Grupen, I. Buvats (Eds.) (2011).

[33] T. Ypsilantis and J. Seguinot, "Theory of Ring Imaging Cherenkov Counters", Nucl. Instr. and Meth. A **343**, 30–51 (1994).

[34] P. Coyle et al., "The DIRC Counter: A New Type of Particle Identification Device for B Factories", Nucl. Instr. and Meth. A **343**, 292–299 (1994).

[35] R. Wilson et al., "The DIRC Particle Identification System for the BaBar Experiment", Nucl. Instr. and Meth. A **538**, 281–357 (2005).

[36] BaBar Collaboration, "Direct CP Violating Asymmetry in $B^0 \to K^+\pi^-$ Decays", Phys. Rev. Lett. **93**, 131801 (2004).

[37] B. Wang, "The Assembly of the Belle II TOP Counter", Nucl. Instr. and Meth. A **766**, 204–207 (2014).

[38] K. Nishimura, "The Time-of-Propagation Counter for Belle II", Nucl. Instr. and Meth. A **639**, 177–180 (2011).

[39] J. Schwiening et al., "Status of the Fast Focusing DIRC (fDIRC)", Nucl. Instr. and Meth. A, RICH 2007 - Proceedings of the Sixth International Workshop on Ring Imaging Cherenkov Detectors **595**, 104–107 (2008).

[40] Belle II Collaboration, "Belle II Technical Design Report", arXiv:1011.0352 [hep-ex, physics:physics] (2010).

[41] K. Föhl et al., "The WASA Focussing Light Guide Disc DIRC", JINST **7**, C01002–C01002 (2012).

[42] M. Charles and R. Forty, "TORCH: Time of Flight Identification with Cherenkov Radiation", Nucl. Instr. and Meth. A **639**, 173–176 (2011).

[43] J. Stevens et al., "The DIRC Project at GlueX", JINST, Proceedings of the DIRC2015 Workshop 11 - 13 November 2015, Rauischholzhausen, Germany, to be published (2016).

[44] G. Kalicy, "Development and Test of a Prototype for the PANDA Barrel DIRC Detector at FAIR", PhD Thesis (Goethe-Universität Frankfurt, 2015).

[45] A. Britting, "Analyse und signifikante Verbesserung der Lebensdauer von Microchannel-Plate Photomultipliern hinsichtlich ihrer Applikation für das PANDA-Experiment", PhD Thesis (Friedrich-Alexander Universität Erlangen-Nürnberg, 2013).

[46] J. Schwiening et al., "Optical Properties of the DIRC Fused Silica Cherenkov Radiator", Nucl. Instr. and Meth. A **515**, 680–700 (2003).

[47] J. Schwiening, *Private Communication*.

[48] M. N. Polyanskiy, *Refractive Index Database*, `http://refractiveindex.info`.

[49] G. Boca and S. Constanza, *Private Communication*.

[50] S. Spataro, "Simulation and Event Reconstruction Inside the PandaRoot Framework", Journal of Physics: Conference Series **119**, 032035 (2008).

[51] *ROOT - Data Analysis Framework*, `https://root.cern.ch/drupal/` (visited on 01/05/2015).

[52] R. Brun and F. Rademakers, "ROOT — An Object Oriented Data Analysis Framework", Nucl. Instr. and Meth. A **389**, 81–86 (1997).

[53] R. Brun et al., *GEANT 3*, CERN Document Server, (1987) `http://cds.cern.ch/record/1119728` (visited on 01/05/2015).

[54] *Geant4: A Toolkit for the Simulation of the Passage of Particles through Matter*, `http://geant4.cern.ch/` (visited on 01/05/2015).

[55] J. Allison et al., "GEANT4: A Simulation toolkit", Nucl. Instr. and Meth. A **506**, 250–303 (2003).

[56] A. Ferrari et al., "FLUKA: A Multi-Particle Transport Code (Program Version 2005)", CERN-2005-010, SLAC-R-773, INFN-TC-05-11 (2005).

[57] M. Starič, "Pattern Recognition for the Time-of-Propagation Counter", Nucl. Instr. and Meth. A, Proceedings of the Seventh International Workshop on Ring Imaging Cherenkov Detectors **639**, 252–255 (2011).

[58] M. Starič et al., "Likelihood Analysis of Patterns in a Time-of-Propagation (TOP) Counter", Nucl. Instr. and Meth. A **595**, 252–255 (2008).

[59] R. Dzhygadlo, *Private Communication*.

[60] B. Efron, "Bootstrap Methods: Another Look at the Jackknife", Ann. Statist. **7**, 1–26 (1979).

[61] Corning Incorporated, One Riverfront Plaza, Corning, NY 14831, USA.

[62] Advanced Glass Industries, 1335 Emerson St, Rochester, NY 14606, USA.

[63] Eljen Technology, 1300 W. Broadway, Sweetwater, TX 79556, USA.

[64] PHOTONIS USA, Inc., 660 Main St, Sturbridge, MA 01518, USA.

[65] A. Lehmann et al., "Lifetime of MCP-PMTs", JINST, Proceedings of the DIRC 2015 Workshop, November 2015 11 - 13, Rauischholzhausen, Germany, to be published (2016).

[66] Advanced Laser Diode Systems A.L.S. GmbH, Schwarzschildstr. 6, 12489 Berlin, Germany.

[67] W. Krzemien et al., "The TRB for HADES and FAIR Experiments at GSI", arXiv preprint arXiv:0810.4723 (2008).

[68] A. Neiser et al., "TRB3: a 264 cannel high precision TDC platform and its applications", JINST **8**, C12043 (2013).

[69] CERN, *Secondary Beams and Areas, The T9 Beam*, `http://sba.web.cern.ch/sba/BeamsAndAreas/East/East.htm` (visited on 03/13/2016).

[70] M. Mota and J. Christiansen, “A High-Resolution Time Interpolator based on a Delay Locked Loop and an RC Delay Line”, IEEE Journal of Solid-State Circuits **34**, 1360–1366 (1999).

[71] NXP Semiconductors N.V., *BGA2712 MMIC Wideband Amplifier*, High Tech Campus 60, 5656 AG Eindhoven, The Netherlands.

[72] CERN, *Low Power Front-End Amplifier NINO ASIC Chip*, `http://knowledgetransfer.web.cern.ch/technology-transfer/external-partners/nino`.

[73] M. Krebs, “Timing Studies for the PANDA Barrel DIRC”, Master Thesis (Goethe-Universität Frankfurt, 2014).

[74] M. Traxler et al., “A Compact System for High Precision Time Measurements (<14 ps RMS) and Integrated Data Acquisition for a Large Number of Channels”, JINST **6**, C12004 (2011).